Electron holography

Rafal E. Dunin-Borkowski [*]

Ernst Ruska-Centre for Microscopy and Spectroscopy with Electrons and Peter Grünberg Institute, Forschungszentrum Jülich, 52425 Jülich, Germany

András Kovács

Ernst Ruska-Centre for Microscopy and Spectroscopy with Electrons and Peter Grünberg Institute, Forschungszentrum Jülich, 52425 Jülich, Germany

Takeshi Kasama

Center for Electron Nanoscopy, Technical University of Denmark, 2800 Kongens Lyngby, Denmark

Martha R. McCartney

Department of Physics and Astronomy and Center for Solid State Science,

Arizona State University, Tempe, Arizona 85287, USA

David J. Smith

Department of Physics and Astronomy and Center for Solid State Science,

Arizona State University, Tempe, Arizona 85287, USA

[*] Corresponding author

Tel. +49 2461 61 9297

Fax +49 2461 61 6444

E-mail: *r.dunin-borkowski@fz-juelich.de*

1. Introduction

Electron holography, as originally described by Gabor [1], is based on the formation of an interference pattern or 'hologram' in the transmission electron microscope (TEM). In contrast to most conventional TEM techniques, which only record spatial distributions of image intensity, electron holography allows the phase shift of the high-energy electron wave that has passed through the specimen to be measured directly. The phase shift can then be used to provide information about local variations in magnetic induction and electrostatic potential. This Chapter provides an overview of the technique of electron holography. It begins with an outline of the experimental procedures and theoretical background that are needed to obtain phase information from electron holograms. Medium-resolution applications of electron holography to the characterization of magnetic domain structures and electrostatic fields are then described, followed by a description of high-resolution electron holography and alternative modes of electron holography. The majority of the experimental results described below are obtained using the off-axis, or 'sideband', TEM mode, which is the most widely used mode of electron holography at present. For further details about electron holography, the interested reader is referred to recent books (e.g., [2-6]), book chapters and review papers (e.g., [7-18]).

1.1. Basis of off-axis electron holography

The off-axis mode of electron holography involves the examination of an electron-transparent specimen using defocused illumination from a highly coherent field emission gun (FEG) electron source. In order to acquire an off-axis electron hologram, the region of interest on the specimen should be positioned so that it covers approximately half the field of view. An electron biprism, which usually takes the form of a fine (< 1 μm diameter) wire [19], is located below the sample, normally in place of one of the conventional selected-area apertures. The application of a voltage to the biprism results in overlap of a 'reference' electron wave that has

passed through vacuum (or through a thin region of support film) with the electron wave that has passed through the specimen, as shown schematically in Fig. 1a. If the illumination is sufficiently coherent, then holographic interference fringes are formed in the overlap region, with a spacing that is inversely proportional to the biprism voltage [20-22]. The amplitude and the phase shift of the electron wave from the specimen are recorded in the intensity and the position of the holographic fringes, respectively. A representative off-axis electron hologram of a chain of magnetite (Fe_3O_4) nanocrystals is shown in Fig. 1b.

[Place Fig. 1 here]

For coherent TEM imaging, the electron wavefunction in the image plane can be written in the form

$$\psi_i(\boldsymbol{r}) = A_i(\boldsymbol{r})exp[i\phi_i(\boldsymbol{r})] \ , \tag{1}$$

where $\boldsymbol{r}$ is a two-dimensional vector in the plane of the sample, A and ϕ refer to amplitude and phase, and the subscript i refers to the image plane. The recorded intensity distribution is then given by the expression

$$I_i(\boldsymbol{r}) = |A_i(\boldsymbol{r})|^2 \ . \tag{2}$$

Thus, the image intensity can be described as the modulus squared of an electron wavefunction that has been modified by the specimen and the objective lens. The intensity distribution in an off-axis electron hologram can be represented by the addition of a tilted plane reference wave to the complex specimen wave, in the form

$$I_{hol}(\boldsymbol{r}) = |\psi_i(\boldsymbol{r}) + exp[2\pi i \boldsymbol{q_c}.\boldsymbol{r}]|^2 \quad (3)$$

$$= 1 + A_i^2(\boldsymbol{r}) + 2A_i(\boldsymbol{r})cos[2\pi i \boldsymbol{q_c}.\boldsymbol{r} + \phi_i(\boldsymbol{r})] \ , \quad (4)$$

where the tilt of the reference wave is specified by the two-dimensional reciprocal space vector $\boldsymbol{q} = \boldsymbol{q_c}$. It can be seen from Equation 4 that there are three separate contributions to the intensity distribution in a hologram: the reference wave, the image wave and an additional set of cosinusoidal fringes with local phase shifts and amplitudes that are exactly equivalent to the phase and amplitude of the electron wavefunction in the image plane, ϕ_i and A_i, respectively.

1.2. Hologram reconstruction

In order to obtain amplitude and phase information, the off-axis electron hologram is first Fourier transformed. From Equation 4, the complex Fourier transform of the hologram is given by the expression

$$FT[I_{hol}(\boldsymbol{r})] = \delta(\boldsymbol{q}) + FT\left[A_i^2(\boldsymbol{r})\right]$$

$$+ \delta(\boldsymbol{q} + \boldsymbol{q_c}) \otimes FT\left[A_i(\boldsymbol{r})exp[i\phi_i(\boldsymbol{r})]\right]$$

$$+ \delta(\boldsymbol{q} - \boldsymbol{q_c}) \otimes FT\left[A_i(\boldsymbol{r})exp[-i\phi_i(\boldsymbol{r})]\right] \ . \quad (5)$$

Equation 5 describes a peak at the reciprocal space origin corresponding to the Fourier transform of the reference image, a second peak centered on the origin corresponding to the Fourier transform of a bright-field TEM image of the sample, a peak centered at $\boldsymbol{q}$ = -$\boldsymbol{q_c}$ corresponding to

the Fourier transform of the desired image wavefunction, and a peak centered at $\boldsymbol{q} = +\boldsymbol{q}_c$ corresponding to the Fourier transform of the complex conjugate of the wavefunction.

The reconstruction of a hologram to obtain amplitude and phase information is illustrated in Fig. 2. Figures 2a-c show a hologram of a thin crystal, an enlargement of part of the hologram, and a Fourier transform of the entire hologram, respectively. In order to recover the amplitude and the relative phase shift of the electron wavefunction, one of the two sidebands is selected digitally and inverse Fourier transformed, as shown in Fig. 2d. The phase of the electron wavefunction can then be calculated directly by evaluating the arctangent of the ratio of the imaginary and real parts of the resulting real-space complex image.

[Place Fig. 2 here]

The impact of electron holography results from the dependence of the phase shift on the electrostatic potential and the in-plane component of the magnetic induction in the specimen. Neglecting the effects of dynamical diffraction (i.e., assuming that the specimen is thin and weakly diffracting), the phase shift can be expressed (in one dimension for simplicity here) in the form

$$\phi(x) = C_E \int V(x,z)dz - \left(\frac{e}{\hbar}\right) \iint B_\perp(x,z)dxdz \ , \tag{6}$$

where $$C_E = \left(\frac{2\pi}{\lambda}\right)\left(\frac{E+E_0}{E(E+2E_0)}\right) \ , \tag{7}$$

z is in the incident electron beam direction, x is in the plane of the specimen, $B_\perp$ is the component of the magnetic induction within and outside the specimen perpendicular to both x and z, V is the electrostatic potential, λ is the (relativistic) electron wavelength and E and E_0 are, respectively,

the kinetic and rest mass energies of the incident electron [23]. C_E has values of 7.29×10^6, 6.53×10^6 and 5.39×10^6 rad V^{-1} m^{-1} at microscope accelerating voltages of 200 kV, 300 kV and 1 MV, respectively. If neither V nor $B_\perp$ vary along the electron beam direction within a sample of thickness t, then Equation 6 can be simplified to

$$\phi(x) = C_E V(x)t(x) - \left(\frac{e}{\hbar}\right)\int B_\perp(x)t(x)dx \quad . \tag{8}$$

By making use of Equations 6 and 8, high spatial resolution information about local variations in V and $B_\perp$ can be recovered from a measurement of the phase shift ϕ, as described below.

1.3. Experimental considerations

In practice, several issues must be addressed in order to record and analyze an electron hologram successfully. A key experimental requirement is the availability of a vacuum reference wave that can be overlapped onto the region of interest on the specimen, which usually implies that the hologram must be recorded from a region close to the specimen edge. This restriction can be relaxed if a thin, clean and weakly diffracting region of electron-transparent support film, rather than vacuum, can be overlapped onto the region of interest.

As phase information is stored in the lateral displacement of the holographic interference fringes, long-range phase modulations arising from inhomogeneities in the charge and thickness of the biprism wire, as well as from lens distortions and charging effects (e.g., at apertures) must be taken into account by recording a reference hologram after removing the specimen from the field of view without changing the optical parameters of the microscope. Correction is then possible by performing a complex division of the sample and reference waves in real space to obtain the distortion-free phase of the image wave [24].

The need for this procedure is illustrated in Fig. 3. Figure 3a shows a reconstructed phase image of a wedge-shaped crystal of InP obtained before distortion correction, with the vacuum region outside the sample edge on the left side of the image [25]. Figure 3b shows the corresponding vacuum reference phase image, which was acquired with the sample removed from the field of view but with all other imaging parameters unchanged. The equiphase contour lines now correspond to distortions that must be removed from the phase image of the sample. Figure 3c shows the distortion-corrected phase image of the sample, which was obtained by dividing the two complex image waves. The vacuum region in Fig. 3c is flattened substantially by this procedure, which allows relative phase changes within the sample to be interpreted much more reliably. The acquisition of a vacuum reference hologram has the additional advantage that it allows the center of the sideband in Fourier space to be determined accurately. The use of the same location for the sideband in the Fourier transforms of the sample and reference waves removes any tilt of the recorded wave that might be introduced by an inability to locate the exact (sub-pixel) position of the sideband frequency in Fourier space.

[Place Fig. 3 here]

Electron holograms have traditionally been recorded on photographic film, but digital acquisition using charge coupled device (CCD) cameras and direct electron detectors is now widely used due to their linear response, dynamic range and high detection quantum efficiency, as well as the immediate accessibility to the recorded information [26-28]. Whether a hologram is recorded on film or digitally, the field of view in a single electron hologram is typically limited to below approximately 5 μm by the dimensions of the recording medium and the sampling of the holographic fringes. However, the vacuum reference wave can be taken from a much larger distance from the region of interest, either by introducing an additional biprism into the condenser lens system of the microscope to achieve a split-illumination mode of electron holography [29,

30] or by recording multiple electron holograms and using an accumulated reconstruction method [31].

A further complication arises from the fact that a phase image that is calculated digitally is usually evaluated modulo 2π, meaning that 2π phase discontinuities that are unrelated to specimen features appear at positions where the phase shift exceeds this amount. The phase image must often then be 'unwrapped' using suitable algorithms [32].

The high electron beam coherence that is required for electron holography usually requires the use of a FEG electron source, a small spot size, a small condenser aperture and a low gun extraction voltage. The coherence may be improved further by adjusting the condenser lens stigmators in the microscope to provide elliptical illumination that is wide in the direction perpendicular to the biprism when the condenser lens is overfocused [33, 34]. The contrast of the holographic interference fringes is determined primarily by the lateral coherence of the electron wave at the specimen level, the mechanical stability of the biprism wire and the point spread function of the recording medium. The fringe contrast

$$\mu = \left(\frac{I_{max}-I_{min}}{I_{max}+I_{min}}\right) \tag{9}$$

can be determined from a holographic interference fringe pattern that has been recorded in the absence of a sample, where I_{max} and I_{min} are the maximum and minimum intensities of the interference fringes, respectively [35]. Should the fringe contrast decrease too much, reliable reconstruction of the image wavefunction will no longer be possible [36].

The phase detection limit for electron holography [37, 38] can be determined from the effect on a recorded hologram of Poisson-distributed shot noise, the detection quantum efficiency

and point spread function of the CCD camera, and the fringe contrast [39-41]. The minimum phase difference between two pixels that can be detected is given by the expression

$$\Delta\phi_{min} = \left(\frac{SNR}{\mu}\right)\sqrt{\frac{2}{N_{el}}}\ , \tag{10}$$

where *SNR* is the signal-to-noise ratio, μ is defined in Equation 9, and N_{el} is the number of electrons collected per pixel [42]. In practice, some averaging of the measured phase is often implemented [43, 44], particularly if the features of interest vary slowly across the image or only in one direction.

A final artifact results from the presence of Fresnel diffraction at the biprism wire, which is visible in Fig. 1b and causes phase and amplitude modulations of both the image and the reference wave [45, 46]. These effects can be removed to some extent by using a reference hologram, and by Fourier-filtering the sideband before reconstruction of the image wave. More advanced approaches for removing Fresnel fringes from electron holograms based on image analysis [47] and multiple-biprism electron holography [48-51] have been introduced. Great care should also be taken to assess the effect on the reference wave of long-range electromagnetic fields that may extend outside the sample and perturb both the object wave and the reference wave [52, 53].

2. Measurement of mean inner potential and sample thickness

Before describing the application of electron holography to the characterization of magnetic and electrostatic fields, the use of the technique to measure local variations in specimen morphology and composition is considered. Such measurements are possible from a phase image that is associated solely with variations in mean inner potential and specimen thickness. When a

specimen has uniform structure and composition in the electron beam direction, and in the absence of magnetic and long-range electrostatic fields (such as those at depletion regions in semiconductors), Equation 8 can be rewritten in the form

$$\phi(x) = C_E V_0(x) t(x) \ , \tag{11}$$

where the mean inner potential of the specimen, V_0, is the volume average of the electrostatic potential [54]. To a first approximation, values of V_0 can be calculated from the equation

$$V_0 = \left(\frac{h^2}{2\pi m e \Omega}\right) \sum_\Omega f_{el}(0) \tag{12}$$

by treating the specimen as an array of neutral atoms. In Equation 12, $f_{el}(0)$ are electron scattering factors at zero scattering angle for each atom, which have been calculated by, for example, Doyle and Turner [55] and Rez et al. [56], and Ω is typically the volume of the unit cell in a crystalline material. However, values of V_0 that are calculated using Equation 12 are invariably overestimated as a result of bonding in the specimen [57, 58]. It is therefore important to obtain experimental measurements of V_0. According to Equation 11, an independent measure of the specimen thickness profile is required in order to determine V_0, for example by examining a specimen in which the thickness changes in a well-defined manner, as shown in Fig. 4a for a phase profile obtained from a 90° wedge of GaAs tilted to a weakly diffracting orientation. If the specimen thickness profile is known, then V_0 can be determined by measuring the gradient of the phase $d\phi/dx$, and making use of the relation

$$V_0 = \left(\frac{1}{C_E}\right)\left(\frac{d\phi/dx}{dt/dx}\right) \ . \tag{13}$$

[Place Fig. 4 here]

This approach has been used successfully to measured the mean inner potential of cleaved wedges and cubes of Si, MgO, GaAs, PbS [59, 60] and Ge [61]. The resulting values of V_0 that were determined for MgO, GaAs, PbS and Ge using this approach are 13.0±0.1, 14.5±0.2, 17.2±0.1 and 14.3±0.2 V, respectively. In a similar study, wedge-shaped Si samples with stacked Si oxide layers on their surfaces were used to measure the mean inner potentials of the oxide layers [62]. Experimental measurements of V_0 have been obtained from 20-40 nm-diameter Si nanospheres coated in layers of amorphous SiO_2 [63]. The mean inner potential of crystalline Si was found to be 12.1±1.3V, that of amorphous Si 11.9±0.9 V and that of amorphous SiO_2 10.1±0.6 V. The mean inner potential of ZnO nanowires has been measured to be 14.30±0.28 V using off-axis electron holography [64]. Similar measurements obtained from spherical latex particles embedded in vitrified ice have provided values for V_0 of 8.5±0.7 and 3.5±1.2 V for the two materials, respectively [65].

Dynamical contributions to the phase shift complicate the determination of V_0 from crystalline samples [59, 61, 66]. These corrections can be taken into account by using either multislice or Bloch wave algorithms [67, 68]. The fact that Equation 11 is no longer valid when the sample is tilted to a strongly diffracting orientation is demonstrated in Fig. 4b for a 90° cleaved wedge sample of GaAs that has been tilted close to a <100> zone axis. The phase shift varies non-linearly with sample thickness, and is also very sensitive to small changes in sample orientation. Fortunately, dynamical contributions to the phase do not significantly affect measurements of phase shifts at medium resolution from amorphous materials or liquids [69-72] or from very thin samples of low-atomic-number two-dimensional materials [73, 74]. Additional experimental factors that may affect measurements of V_0 include the chemical and physical state and the crystallographic orientation of the specimen surface [75], and specimen charging [76-81].

If V_0 is already known, then measurements of the phase shift can be used to determine the local specimen thickness t. Alternatively, the specimen thickness can be inferred from a holographic amplitude image in units of λ_{in}, the mean free path for inelastic scattering, by making use of the relation

$$\frac{t(x)}{\lambda_{in}} = -2ln\left(\frac{A_i(x)}{A_r(x)}\right) , \tag{14}$$

where $A_i(x)$ and $A_r(x)$ are the measured amplitudes of the sample and reference holograms, respectively [82, 83]. When applying Equation 14 to experimental amplitude images, the holographic fringe contrast outside the specimen must be normalized to unity if it is not the same for the sample and reference holograms. If desired, the sample-thickness-dependence of both the phase and the amplitude image can be removed by combining Equations 11 and 14 in the form

$$\frac{\phi(x)}{-2C_E ln\left(\frac{A_i(x)}{A_r(x)}\right)} = V_0(x)\lambda_{in}(x) \ . \tag{15}$$

Equation 15 can be used to generate an image, in which the contrast is the product of the local values of the mean inner potential and the inelastic mean free path. These parameters depend only on the local composition of the sample, and thus can be useful for interpreting images obtained from samples with varying composition and thickness [84, 85].

If the mean inner potential in a specimen is constant or if its variation across the specimen is known, then the morphologies of nanoscale particles (for which dynamical contributions to the phase shift are likely to be small) can be measured using electron holography by making use of Equation 11. Examples of the measurement of specimen shapes using this approach include the characterization of faceted ZrO_2 crystals [86], carbon nanotubes [87], bacterial flagellae [88] and atomic-height steps on clean surfaces of MoS_2 [89]. Such

measurements can in principle be extended to three dimensions by combining electron holography and electron tomography [90], as demonstrated by the acquisition and analysis of tilt series of electron holograms of latex spheres [91, 92], Pt nanoparticles [93] and semiconductor nanowires [83]. The demanding nature of the latter measurements results from the facts that specimen tilt angles of at least ±60°, as well as small tilt steps, accurate alignment of the resulting phase images and sophisticated reconstruction algorithms, are typically required in order to avoid artifacts.

3. Measurement of magnetic fields

The most successful and widespread applications of electron holography have involved the characterization of magnetic fields within and surrounding materials at medium spatial resolution. When examining magnetic materials, the normal microscope objective lens is usually switched off, as its strong magnetic field is likely to saturate the magnetization in the sample along the electron beam direction. A high-strength Lorentz mini-lens [21, 22] located below the objective lens is then often instead used to provide reasonably high magnification (~ 50-75 k×), with the sample either in a magnetic-field-free environment or in a chosen (pre-calibrated) vertical magnetic field provided by using an intermediate setting of the TEM objective lens (combined with tilting of the specimen) or a dedicated in situ magnetizing specimen holder [94-98].

3.1. Early experiments

Although the earliest studies of magnetic fringing fields outside materials in the TEM, which involved using beam stops [99, 100] and distortions of wire meshes [101], can be traced back to the 1940s and 1950s, the characterization of magnetic materials using electron holography

has only developed rapidly since the 1980s. Early examples of the examination of magnetic materials using electron holography involved the reconstruction of electron holograms using a laser bench, and included the characterization of horseshoe magnets [102], magnetic recording media [103] and vortices in superconductors [104-106]. The most elegant of these experiments involved the confirmation of the Aharonov-Bohm effect [107, 108], which states that when an electron wave from a point source passes on either side of an infinitely long solenoid then the relative phase shift between the two parts of the wave results from the presence of a vector potential. In this way, the Aharonov-Bohm effect provides the only observable confirmation of the physical reality of gauge theory. Electron holography experiments were carried out on 20-nm-thick permalloy toroidal magnets that were covered with 300-nm-thick layers of superconducting Nb, which prevented electrons from penetrating the magnetic material and confined the magnetic flux by exploiting the Meissner effect [109, 110]. The observations showed that the phase difference between the center of the toroid and the region outside was quantized to a value of 0 or π when the temperature was below the Nb superconducting critical temperature (5 K), i.e., when a supercurrent was induced to circulate in the magnet. The observed quantization of magnetic flux, and the measured phase differences with the magnetic field entirely screened by the superconductor, provided unequivocal confirmation of the Aharonov-Bohm effect.

3.2. Digital acquisition and analysis

Recent applications of electron holography to the characterization of magnetic fields in nanostructured materials have been based on digital recording and processing. The examples that are described below highlight the different approaches that can be used to separate a desired magnetic signal from a recorded phase image, as well as illustrating the magnetic properties of the materials. The off-axis mode of electron holography is ideally suited to the characterization of magnetic fields in nanoscale materials because unwanted contributions to the contrast from local variations in composition and specimen thickness can usually be removed from a phase

image more easily than from images recorded using other TEM phase contrast techniques. For example, the Fresnel and Foucault modes of Lorentz microscopy [111] and differential phase contrast (DPC) imaging [112-114] provide signals that are approximately proportional to either the first or the second differential of the phase shift. These techniques inherently enhance contributions to the contrast from rapid variations in specimen thickness and composition, as compared to the weak and slowly varying magnetic signal.

The *digital* acquisition, reconstruction and analysis of electron holograms has allowed magnetic fields within samples with small feature sizes and rapid variations in thickness or composition to be examined. The key advantage of digital analysis is that the magnetic and mean inner potential contributions to the measured holographic phase shift can be separated, particularly at the edges of nanostructured particles, where rapid changes in specimen thickness can dominate both the phase and the phase gradient. Examples of approaches that can be used to achieve this separation are described below. Digital analysis also facilitates the construction of line profiles from phase images, which can provide quantitative information such as the widths of magnetic domain walls.

Determination of the phase gradient is particularly useful for studies of magnetic materials because of the following relationship, which is obtained by differentiating Equation 8:

$$\frac{d\phi(x)}{dx} = C_E \frac{d}{dx}\{V(x)t(x)\} - \left(\frac{e}{\hbar}\right) B_{\perp}(x)t(x) \quad . \tag{16}$$

According to Equation 16, for a specimen of uniform thickness and composition the phase gradient is proportional to the in-plane component of the magnetic induction in the specimen

$$\frac{d\phi(x)}{dx} = -\left(\frac{et}{\hbar}\right) B_{\perp}(x) \quad . \tag{17}$$

A direct graphical representation of the magnetic induction can therefore be obtained by adding contours to a magnetic phase image, where a phase difference of 2π corresponds to an enclosed magnetic flux of 4×10^{-15} Wb. Significantly, an experimental phase image does not need to be unwrapped in order to evaluate its first differential digitally. Instead, if the reconstructed image wave is designated ψ, then the phase differential can be determined directly from the expression

$$\frac{d\phi(x,y)}{dx} = Im\left(\frac{\frac{d\psi(x,y)}{dx}}{\psi(x,y)}\right) \quad . \tag{18}$$

Most of the results that are described below were acquired using Philips CM200ST, Philips CM300ST and FEI Titan FEG TEMs equipped with rotatable electron biprisms, and with Lorentz mini-lenses located in the bores of their objective lens pole-pieces. The Lorentz lenses allow electron holograms to be recorded at magnifications of up to ~75 k× with the specimens located in magnetic-field-free environments.

NdFeB hard magnets

Figure 5a shows a Lorentz (Fresnel defocus) image of a $Nd_2Fe_{14}B$ specimen, in which magnetic domains can be seen [115]. Such images provide little information about the direction of the local projected magnetic induction in the specimen. An electron holographic phase image acquired from the same area using an interference fringe spacing of 2.5 nm is shown in Fig. 5b. Gradients of the phase image were calculated along the +x and -y directions, as shown in Figs. 5c and d, respectively. These images were combined to form a vector map of the magnetic induction, as shown in Fig. 5e. The map is divided into 20 nm squares, and has a low contrast phase gradient

image superimposed on it for reference purposes. The minimum vector length is zero (corresponding to out-of-plane projected magnetic induction), while the maximum vector length is consistent with a measured in-plane magnetic induction B of 1.0 T. A vector map of the region marked in Fig. 5e is shown at higher magnification in Fig. 5f. In this map, magnetic vortices show Bloch-like character, with vanishingly small vector lengths. Care is needed when interpreting the fine details in such maps due to the possible effects of magnetic fringing fields immediately above and below the sample, as well as contributions from variations in specimen thickness. A single pixel line scan across a 90° domain wall, which appears as the bright ridge near the central part of Fig. 5b, is shown in Fig. 5g. This line profile places an upper limit of 10 nm on the magnetic domain wall width, which agrees well with theoretical estimates. More recent studies of magnetic domain walls using off-axis electron holography have benefited from the preparation of TEM samples of uniform thicknes using focused ion beam (FIB) milling (e.g., [116]).

[Place Fig. 5 here]

Co nanoparticle chains

The dominant nature of the mean inner potential contribution to the phase shift recorded from a nanoscale magnetic particle is illustrated in Fig. 6. Figures 6a and b show a hologram and a reconstructed phase image of a chain of Co particles suspended over a hole in a carbon support film [117]. Figures 6c and d show corresponding line traces determined from the phase image across the centers of two particles. Each trace is obtained in a direction perpendicular to the chain axis. The in-plane magnetic induction and mean inner potential of each particle can be determined by fitting simulations to the experimental line traces. Analytical expressions for the expected phase shifts can be derived for a uniformly magnetized sphere of radius a, in-plane magnetic induction $B_{\perp}$ (along y) and mean inner potential V_0 in the form

$$\phi(x,y)|_{(x^2+y^2)<a^2} = 2C_E V_0\sqrt{a^2-(x^2+y^2)} + \left(\frac{e}{\hbar}\right) B_\perp a^3 \left(\frac{x}{x^2+y^2}\right)\left[1-\left(1-\left(\frac{x^2+y^2}{a^2}\right)\right)^{\frac{3}{2}}\right] \quad (19)$$

$$\phi(x,y)|_{(x^2+y^2)>a^2} = \left(\frac{e}{\hbar}\right) B_\perp a^3 \left(\frac{x}{x^2+y^2}\right) , \quad (20)$$

where $B_\perp = \left(\frac{2}{3}\right)\mu_0 M_0$ (along *y*) for a spherical magnetic particle and M_0 is the magnetization of the material.

For line profiles through the centers of the particles in a direction perpendicular to that of $B_\perp$, these expressions reduce to

$$\phi(x)|_{x<a} = 2C_E V_0\sqrt{a^2-x^2} + \left(\frac{e}{\hbar}\right) B_\perp \left[\frac{a^3-(a^2-x^2)^{\frac{3}{2}}}{x}\right] \quad (21)$$

$$\phi(x)|_{x>a} = \left(\frac{e}{\hbar}\right) B_\perp \left(\frac{a^3}{x}\right) . \quad (22)$$

Least squares fits of Equations 21 and 22 to the experimental data points, which are also shown in Figs. 6c and d, were used to provide best-fitting values for *a*, $B_\perp$ and V_0 [117].

[Place Fig. 6 here]

3.3. Separation of magnetic and mean inner potential contributions

When characterizing magnetic fields inside nanostructured materials, the mean inner potential contribution to the measured phase shift must in general be removed in order to interpret

the magnetic contribution of primary interest. Several approaches can be used to achieve this separation. First, the sample may be inverted to change the sign of the magnetic contribution to the signal and a second hologram recorded. The sum and the difference of the two phase images can then be used to provide twice the magnetic contribution, and twice the mean inner potential contribution, respectively [118, 119]. Second, two holograms may be acquired from the same area of the specimen at two different microscope accelerating voltages. In this case, the magnetic signal is independent of accelerating voltage, and subtraction of the two phase images can be used to provide the mean inner potential contribution. Third, electron holograms can be recorded below and above the magnetic Curie temperature of the specimen. A fourth, often more practical, method of removing the mean inner potential contribution involves performing magnetization reversal in situ in the electron microscope, and subsequently selecting pairs of holograms that differ only in the (opposite) directions of the magnetization in the specimen. The magnetic and mean inner potential contributions to the phase can be calculated by taking half the difference, and half the sum, of the phases. The mean inner potential contribution can then be subtracted from all other phase images acquired from the same specimen region [120]. In situ magnetization reversal, which is required both for this purpose and for performing magnetization reversal experiments in the TEM, can be achieved by exciting the conventional microscope objective lens slightly and tilting the specimen to apply known magnetic fields, as shown schematically in Fig. 7. Subsequently, electron holograms can be recorded with the conventional microscope objective lens switched off and the Lorentz lens switched on, while the magnetic specimen is located in a magnetic-field-free environment. In practice, if the two remanent magnetic states are not exactly equal and opposite to each other, then it may be necessary to repeat the switching process several times so that non-systematic differences between switched pairs of phase images average out. Such differences, which can lead to artifacts in the final magnetic induction map, can sometimes be identified simply by inspection. By varying the applied magnetic field, it is also possible to record a series of images that correspond to any desired point on a remanent hysteresis loop or magnetization reversal cycle.

[Place Fig. 7 here]

Magnetite nanoparticle chains

Results obtained from a chain of magnetite (Fe_3O_4) nanoparticles, which are shown in Fig. 8, illustrate the fact that both the mean inner potential and the magnetic contribution to the phase shift can provide useful information. In particular, the mean inner potential contribution can be used to interpret the morphologies and orientations of nanoparticles, as discussed above. Figures 8a and b show phase contours generated from, respectively, the mean inner potential and magnetic contributions to the phase shift at the end of a chain of magnetite crystals from a magnetotactic bacterium collected from a brackish lagoon at Itaipu in Brazil. The magnetic moment that the crystals impart to the bacterial cell results in its alignment and subsequent migration along the Earth's magnetic field lines [121-123]. Separation of the mean inner potential and magnetic contributions to the phase shift was achieved by using the field of the conventional microscope objective lens to magnetize each chain parallel and then anti-parallel to its length in situ in the TEM, as illustrated in Fig. 7. The contours in Figs. 8a and b have been overlaid onto the mean inner potential contribution to the phase. In Fig. 8a, they are associated with variations in specimen thickness and are confined primarily to the crystals, while in Fig. 8b they correspond to magnetic lines of force, which extend smoothly from within the crystals to the surrounding region. Figure 8c shows line profiles measured across the large and small magnetite crystals visible close to the centers of Figs. 8a and b, in a direction perpendicular to the chain axis. Individual experimental data points are shown as open circles. Corresponding simulations based on Equation 8 are shown on the same axes. The darker solid line shows the best-fitting simulation to the data for the larger crystal, on the assumption that the external shape is formed from a combination of {111}, {110} and {100} faces. The simulation corresponds to a distorted

hexagonal shape in cross-section (shown as an inset above the figure). The lighter line shows a worse fit, provided by assuming a diamond shape in cross-section. Off-axis electron holography has been used to provide unique information about differences in magnetic microstructure between different strains of magnetotactic bacteria that contain both magnetite nanocrystals [124-126] and greigite (Fe_3S_4) nanocrystals [127].

[Place Fig. 8 here]

Recent experiments have involved the combined application of off-axis electron holography, environmental TEM and in situ heating to study the effects of oxidation and temperature on the remanent magnetic states of magnetite nanocrystals [128-132], as well as the study of magnetic states in superstructured magnetite nanoparticles [133] and magnetite nanocrystals studied in a closed liquid cell in situ in the TEM [72].

Co nanoparticle rings

An illustration of the characterization of magnetostatic interactions between particles that each contain a single magnetic domain is provided by the examination of rings of 20-nm-diameter crystalline Co particles, as shown in Fig. 9. Such rings are appealing candidates for high density information storage applications because they are expected to form chiral magnetic domain states that exhibit flux closure (FC). Magnetic nanoparticle rings are also of interest for the development of electron holography because their magnetization directions cannot be reversed by applying an in-plane external field. As a result, phase images were obtained both before and after inverting the specimen. The resulting pairs of phase images were aligned in position and angle, and their sum and difference calculated as described above. Figure 9a shows a low magnification bright-field image of the Co rings [134]. A variety of self-assembled structures is visible, including five- and six- particle rings, chains and closely-packed aggregates.

The particles are each encapsulated in a 3-4 nm oxide shell. Figures 9b-d show magnetic FC states in four different Co particle rings, measured using electron holography at room temperature in zero-magnetic-field conditions [135]. The magnetic flux lines, which are formed from the cosine of 128 times the magnetic contribution to the measured phase shift, reveal the projected in-plane magnetic induction within each ring ensemble. Further electron holography experiments show that the chirality of the FC states can often be switched in situ in the TEM by using an out-of-plane magnetic field [136-138].

[Place Fig. 9 here]

FeNi nanoparticle chains

The magnetic properties of nanoparticle chains have been studied for many years (e.g., [139]). However, there are few experimental measurements of the critical sizes at which individual particles that are arranged in chains are large enough to support magnetic vortices rather than single domains. Previous electron holography studies did not provide direct images of such vortex states. Here, we illustrate the use of electron holography to characterize chains of ferromagnetic FeNi crystals, whose average diameter of 50 nm is expected to be close to the critical size for vortex formation [140]. Figure 10a shows a chemical map of a chain of $Fe_{0.56}Ni_{0.44}$ nanoparticles, acquired using a Gatan imaging filter. The particles are each coated in a 3 nm oxide shell. A defocused bright-field image and a corresponding electron hologram recorded from part of a chain are shown in Figs. 10b and c, respectively. The mean inner potential contribution to the phase shift was determined by using the field of the microscope objective lens to magnetize each chain parallel and then anti-parallel to its length. The external magnetic field was removed, before finally recording holograms in magnetic-field-free conditions.

[Place Fig. 10 here]

Figures 11a and b show the remanent magnetic states of two chains of $Fe_{0.56}Ni_{0.44}$ particles, measured using electron holography. For a 75 nm $Fe_{0.56}Ni_{0.44}$ particle sandwiched between two smaller particles (Fig. 11a), closely-spaced contours run along the chain in a channel of width 22±4 nm. A comparison of the result with micromagnetic simulations [140] indicates that the particle contains a vortex with its axis parallel to the chain axis, as shown schematically in Fig. 11c. In Fig. 11b, a vortex can be seen end-on in a 71 nm particle at the end of a chain. The positions of the particle's neighbors determine the handedness of the vortex, with the flux channel from the rest of the chain sweeping around the core to form concentric circles (Fig. 11d). The vortex core, which is now perpendicular to the chain axis, is only 9±2 nm in diameter. The larger value of 22 nm observed in Fig. 11a results from magnetostatic interactions along the chain [141, 142]. Similar vortices were never observed in particles below 30 nm in size, while intermediate states were observed in 30-70 nm particles. Particles with an alloy concentration of $Fe_{0.10}Ni_{0.90}$ were observed to contain wider flux channels of diameter ~70 nm, and single domain states when the particles were above ~100 nm in size [143]. Magnetic vortices have also been observed using electron holography in more complicated arrangements of $Fe_{0.20}Ni_{0.80}$ nanocrystals [144]. The complexity of such vortex states highlights the importance of controlling the shapes, sizes and positions of closely-spaced magnetic nanocrystals for applications in magnetic storage devices.

[Place Fig. 11 here]

Planar arrays of magnetite nanoparticles

The magnetic behavior of the chains and rings of magnetic nanocrystals described above contrasts with that of a regular two-dimensional array of closely-spaced nanomagnets. Figures 12a and b show chemical maps of a crystalline region of a naturally occurring magnetite-ulvöspinel (Fe_3O_4-Fe_2TiO_4) mineral specimen, which exsolved during slow cooling to yield an

intergrowth of magnetite-rich blocks separated by non-magnetic ulvöspinel-rich lamellae [145]. The Fe and Ti chemical maps shown in Fig. 12 were obtained using three-window background-subtracted elemental mapping with a Gatan imaging filter. Exsolution lamellae subdivide the grain into a fairly regular array of magnetite-rich blocks. The specimen thickness increases from 70 nm at the top of the chosen region to 195 nm at the bottom. The magnetite blocks are, therefore, roughly equidimensional.

[Place Fig. 12 here]

Remanent magnetic states were recorded by tilting the specimen in zero field and then turning the objective lens on fully to saturate the sample, in order to provide a known starting point from which further fields could be applied. The objective lens was then turned off, the specimen tilted in zero field in the opposite direction and the objective lens was excited partially to apply a known in-plane field component to the specimen in the opposite direction. The objective lens was switched off and the sample tilted back to 0° in zero field to record each hologram. This procedure was repeated for a number of different applied magnetic fields [146]. Mean inner potential contributions to the measured phase shifts were removed using a different procedure to that used for the chains and rings of nanoparticles described above. Although both thickness and composition vary in the magnetite-ulvöspinel specimen, the different compositions of magnetite and ulvöspinel are compensated by their densities in such a way that their mean inner potentials are almost exactly equal. As a result, only a thickness correction is required. The local specimen thickness across the region of interest was determined in units of inelastic mean free path by using energy-filtered imaging. This thickness measurement was then used to determine the mean inner potential contribution to the phase shift, which was in turn used to determine the magnetic contribution to the phase. Figure 13 shows eight of the resulting remanent magnetic states recorded after applying the in-plane fields indicated. Just as in Fig. 9, the black contour lines provide the direction and magnitude of the projected magnetic induction in the plane

of the sample, which can be correlated with the positions of the magnetite blocks (outlined in white). The direction of the measured magnetic induction is also indicated using colors and arrows, according to the color wheel shown at the bottom of the figure. Figure 13 shows that the magnetic domain structure in this sample is extremely complex. In Fig. 13, the smallest block observed to form a vortex is larger than the predicted minimum size of 70 nm for vortices to form in *isolated* cubes of magnetite. The abundance of single domain states implies that they have lower energy than vortex states in the presence of strong magnetostatic interactions between closely adjacent blocks. The demagnetizing energy, which normally destabilizes the single domain state with respect to the vortex state in isolated particles, is greatly reduced in an array of strongly interacting particles.

[Place Fig. 13 here]

Figure 14 illustrates similar results obtained from a study of magnetite-ulvöspinel inclusions in clinopyroxene [147]. In this sample, strong magnetostatic interactions between adjacent magnetite blocks constrain their remanent magnetization direction to lie almost perpendicular to their elongation directions and to the applied field direction. Interactions between magnetic microstructure and ferroelastic twin boundaries in pure magnetite samples above and below the Verwey transition have also been investigated in detail using electron holography [148-150].

[Place Fig. 14 here]

Planar arrays of much smaller (~15 nm) self-assembled Co nanoparticles have been studied using electron holography, in order to understand the influence of magnetostatic (dipolar) interactions on the correlation between particle arrangement and magnetic order [151]. Dipolar ferromagnetism, antiferromagnetism and local flux closure were observed in one-dimensional

and quasi-two-dimensional arrays, depending on the particle arrangement. Ferromagnetic order was shown to exist in the nanoparticle assemblies even when their structural arrangement was disordered.

Lithographically patterned magnetic nanostructures

Specimen preparation presents a major challenge for many samples of interest that contain nanostructured magnetic materials. An example is provided by a study of nanomagnet arrays that were fabricated directly on a Si substrate using interferometric lithography [152]. Figure 15a shows a scanning electron microscope image of nominally 100-nm-diameter 20-nm-thick Co dots fabricated on Si in a square array of side 200 nm. The dots were prepared for TEM examination using FIB milling in plan-view geometry, by micro-machining a trench from the substrate side of the specimen to leave a free-standing 10 × 12 μm membrane of crystalline Si, which was had a thickness of approximately 100 nm and contained over 3000 Co dots. Figure 15b shows an off-axis electron hologram recorded from part of the electron-transparent membrane containing the dots. The specimen was tilted slightly away from zone axis orientations of the underlying Si substrate to minimize diffraction contrast. The specimen edge is towards the bottom left of the figure [153, 154]. Figures 15c and d show contours of spacing $0.033 \approx \pi/94$ radians superimposed on the (slightly smoothed) magnetic contribution to the holographic phase, for two different remanent magnetic states of the Co dots. In Fig. 15c, which was recorded after saturating the dots upwards and then removing the external field, the dots are oriented magnetically in the direction of the applied field. In contrast, in Fig. 15d, which was recorded after saturating the dots upwards, applying a 382 Oe downward field and then removing the external field, the dots are magnetized in a range of different directions. The experiments show that the dots are sometimes magnetized out of the plane (e.g., at the bottom left of Fig. 15d). The measured saturation magnetizations are smaller than expected for pure Co, possibly because of oxidation or damage

sustained during specimen preparation. Similar electro-deposited 57-nm-diameter 200-nm-high Ni pillars arranged in square arrays of side 100 nm, which were prepared for TEM examination using FIB milling in a cross-sectional geometry, have also been examined [155]. Despite their shape, not all of the Ni pillars were magnetized parallel to their long axes. Instead, they interacted with each other strongly, with two, three or more adjacent pillars combining to form vortices.

[Place Fig. 15 here]

Similar results to those shown in Fig. 15 have been obtained from a wide range of other lithographically patterned structures, many of which show multi-domain behavior [156-158]. Few phase contours are visible outside such elements when they support magnetic flux closure states. Electron holography has also been used to provide information about magnetic interactions between closely-separated ferromagnetic layers within individual Co/Au/Ni spin-valve elements [159]. The presence of two different contour spacings at different applied fields in such elements is associated with the reversal of the magnetization direction of the Ni layer in each element before the external field is reduced to zero, as a result of flux closure associated with the strong magnetic fringing field of the magnetically more massive and closely adjacent Co layer.

The use of a TEM specimen holder equipped with multiple electrical contacts has allowed Lorentz TEM and electron holography to be used to study the competing effects of heating and spin torque on the current-induced motion of transverse and vortex-type domain walls in lithographically patterned permalloy wires [160]. The device comprised permalloy zigzag structures with line widths and thicknesses of 430 and 11 nm, respectively. Electron holograms were recorded at sequential positions of a magnetic domain wall that was moved along a wire using 10 μs pulses with a current density of 3.14×10^{11} A/m^2. It was observed that a transverse wall initially formed at a kinked region of the wire after the application of a magnetic field. After applying a current pulse, the magnetic domain wall moved by ~2 μm in the direction of electron

flow and transformed into a vortex-type wall. After a second pulse, the vortex-type magnetic domain wall moved slightly in the same direction and became distorted, with the long axis of the vortex increasingly perpendicular to the wire length. This behavior may be associated with edge roughness or defects, which may restrict movement of the wall. After a third pulse, the magnetic domain wall moved 260 nm further and retained its vortex state. More recent studies have involved the injection of smaller currents to influence thermally-activated magnetic domain wall motion between closely-adjacent pinning sites [161].

Magnetic skyrmions

Magnetic skyrmions are nanoscale spin objects that can be stabilised in chiral magnets and bilayer thin films due to the Dzyaloshinskii-Moriya interaction (DMI) [162-164]. The ability to move magnetic skyrmions using extremely low electrical currents [165] has triggered interest in their use in new magnetic data storage and spintronics technologies, in which the skyrmions are proposed to act as data bit carriers. Figure 16 shows electron holographic magnetic induction maps recorded from Bloch-type magnetic skyrmions in specimen of *B*20-type FeGe that had been prepared for TEM examination using FIB milling [166-168]. The sample was examined below the magnetic transition temperature T_C of 278.3 K using a liquid nitrogen cooling holder, while controlling the pre-calibrated magnetic field applied to the sample by changing the current of the microscope objective lens. In order to separate the magnetic contribution to the phase shift from the mean inner potential contribution, phase images were recorded both at low temperature and at room temperature. The phase images were then aligned and subtracted from each other (on the assumption that the mean inner potential is the same and that there are no changes in diffraction contrast or specimen charging between the two temperatures). Below the transition temperature, the material is observed to adopt a helical magnetic structure in zero magnetic field, which transforms into a skyrmion lattice upon applying a perpendicular (out-of-plane) magnetic field to the sample.

[Place Fig. 16 here]

Figure 16 shows that a hexagonal skyrmion lattice initially forms upon cooling the sample below the critical temperature in the presence of a small out-of-plane magnetic field. The average magnetic phase shift of an individual skyrmion was measured to be ~0.7 radians at 95 K for the present sample thickness. The magnitude of the measured phase shift decreases gradually as the temperature is increased to 280 K. These observations suggest that the critical temperature in a thin film of *B*20-FeGe is identical to the bulk value. As the out-of-plane magnetic field was increased to 300 mT at a constant temperature of 200 K, the skyrmion lattice started to deviate from a hexagonal arrangement, becoming disordered at approximately 350 mT. A gradual decrease in skyrmion core diameter was accompanied by an expansion of the lattice period. At 400 mT, the number of skyrmions decreased significantly. Between adjacent skyrmions, the sample then became fully saturated by the applied magnetic field. At 450 mT, no skyrmions remained and the sample was fully saturated magnetically parallel to the applied magnetic field direction. The measured magnetic phase shifts of individual skyrmions were observed to decrease with increasing applied magnetic field.

In a separate study, the detailed magnetic configurations of individual skyrmions in a lattice arrangement were analysed [169]. It was shown that there is no significant dependence of skyrmion structure on temperature. The influence of confining skyrmions to a narrow stripe of *B*20-FeGe was also studied experimentally. FIB-prepared wedge-shaped samples and theoretical calculations were used to create a temperature *vs* applied magnetic field phase diagram [170]. It was shown that a distorted helical spin structure, which forms at a low value of applied magnetic field, transforms into a pure edge twist, a single skyrmion chain or a zig-zag skyrmion chain in the presence of an applied magnetic field, depending on the width of the stripe. The skyrmions in

the stripe were observed to exhibit longitudinal and transverse elliptical distortions. This work was subsequently extended to studies of "target" skyrmions confined to nanoscale disks of *B*20-FeGe [171].

Co nanowires

An important question relates to the minimum size of a nanostructure in which magnetic fields can be characterized successfully using electron holography. This point was addressed in an early study of 4-nm-diameter single crystalline Co nanowires [172]. The difficulty of this measurement results from the fact that the mean inner potential contribution to the phase shift at the center of a 4 nm wire relative to that in vacuum is 0.57 radians (assuming a value for V_0 of 22 V), whereas the step in the magnetic contribution to the phase shift across the wire is only 0.032 radians (assuming a value for *B* of 1.6 T). Figure 17a shows a bright-field TEM image of a bundle of 4-nm-diameter Co wires, which are each between a few hundred nm and several hundred μm in length. Magnetic contributions to the phase shift were obtained by recording two holograms from each area of interest, with the wires magnetized parallel and then antiparallel to their length by tilting the sample by ±30° about an axis perpendicular to the wire axis and using the conventional microscope objective lens to apply a large in-plane field to the specimen. The lens was then switched off and the sample returned to zero tilt to record each electron hologram. This procedure relies on the ability to reverse the magnetization in the sample exactly, which is a good assumption for such narrow and highly anisotropic wires. Figure 17b shows the magnetic contribution to the measured phase shift for an isolated wire, in the form of contours that are spaced 0.005 radians apart. The contours have been overlaid onto the mean inner potential contribution to the phase shift, so that they can be correlated with the position of the wire. The magnetic signal is weak and noisy, and was smoothed before forming the contours. The closely-spaced contours along the length of the wire confirm that it is magnetized along its axis. The fact

that they are not straight is intriguing. However, it may result simply from smoothing of the signal, which is noisy and weak.

[Place Fig. 17 here]

Figure 18a shows a montage of three holograms obtained close to the end of a bundle of the same Co wires, which was magnetized approximately parallel to its length. The magnetic contribution to the phase shift is shown in Fig. 18b in the form of contours, which are spaced 0.25 radians apart. The nanowires can be seen to channel the magnetic flux efficiently along their length, and they fan out as the field decreases in strength at the end of the bundle. Although the signal from the bundle of nanowires appears to obscure that from individual wires and junctions, these details can be recovered by increasing the density of the contours [172]. The slight asymmetry between the contours on either side of the bundle in Fig. 18b may result from the fact that the holographic reference wave is affected by the magnetic leakage field of the bundle, which acts collectively as though it were a single wire of larger diameter. The step in magnetic phase across the bundle is (9.0±0.2) radians, which is consistent with the presence of (280±7) ferromagnetically coupled wires.

[Place Fig. 18 here]

A more recent study of nanowires consisting of periodic layers of magnetically soft layers of CoFeB and non-magnetic layers of Cu fabricated by electrodeposition in nanoporous alumina membranes revealed a dependence of the magnetization direction of the ferromagnetic segments, relative to the nanowire axis, on wire diameter and layer thickness [173].

Cross-sectional specimens

One of the most challenging problems for electron holography of magnetic materials is the quantitative measurement of the magnetic properties of nm-scale magnetic layers that are examined in cross-section. The primary difficulty is the presence of rapid and unknown variations in both the composition and the thickness of the specimen, from which the weak magnetic signal must be separated. In a cross-sectional sample, the effects of variations in specimen thickness on the measurements cannot be eliminated by using the normalized amplitude of the hologram (Equation 14), both because the mean free path in each material in such a cross-sectional specimen is usually unknown and because the amplitude image is in general noisy and may contain strong contributions from diffraction and Fresnel contrast. However, by rearranging Equations 8 and 16, it can be shown that, in the absence of strong Fresnel contrast from the magnetic contrubution to the phase, specimen thickness effects may be removed by plotting the difference in phase gradient between images in which the magnetization has reversed divided by the average of their phases, multiplied by a constant and by the value of the mean inner potential of each magnetic layer separately [120]. Formally, this procedure can be written

$$\left(\frac{C_E \hbar V_0(x,y)}{e}\right)\left\{\frac{\Delta[d\phi(x,y)/dx]}{\langle\phi(x,y)\rangle}\right\} = \frac{\Delta B_\perp(x,y)}{(1-(e/C_E\hbar V_0(x,y)))\{\langle\int B_\perp(x,y)t(x,y)dx\rangle/t(x,y)\}} \ . \qquad (23)$$

According to Equation 23, by combining phase profiles and their gradients (evaluated in a direction perpendicular to the layers) from successive holograms between which the magnetization direction in the specimen was reversed, the thickness profile can be eliminated and the magnetic induction in each layer can be determined quantitatively. Both the magnitude and the sign of $\Delta B_\perp(x,y) = 2B_\perp(x,y)$ are obtained exactly using Equation 23 if the magnetization reverses exactly everywhere in the sample. (The denominator on the right-hand side of the equation is then unity). Furthermore, non-zero values are returned only in regions where the

magnetization has changed. Figure 19 illustrates the application of Equation 23 to a cross-sectional magnetic tunnel junction that contains a layer sequence of 22 nm Co/ 4 nm HfO_2/ 36 nm CoFe on a Si substrate [174]. Two holograms were obtained, similar to that shown in Fig. 19a, between which the magnetization directions of the Co and CoFe layers in the specimen were reversed in situ in the electron microscope. Figure 19b shows an unwrapped phase profile obtained from the hologram in Fig. 19a by taking a line profile in the direction perpendicular to the layers. Phase profiles from the two holograms appeared almost identical irrespective of the direction of magnetization. The application of Equation 23 to the two phase images results in the image shown in Fig. 19c. The line profile in Fig. 19d was obtained by averaging Fig. 19c parallel to the direction of the layers. As predicted, Fig. 19d, which should by now be independent of variations in composition and specimen thickness, is non-zero only in the magnetic layers and yields a value for the magnetic induction in the Co layer of 1.5 T (assuming a mean inner potential of 25 V).

[Place Fig. 19 here]

Similar approaches have been used to remove specimen thickness and mean inner potential contributions from phase images of $La_xCa_{1-x}MnO_3$ acquired at different temperatures [175, 176], as well from phase images recorded from a $GdBa_2Cu_3O_7/La_{0.75}Sr_{0.25}MnO_3$ superlattice above and below the Curie temperature of the manganite layers [177]. Thicker magnetic layers that display more complicated magnetic states in cross-section have also been studied using electron holography [178, 179].

3.4. Quantitative measurements, micromagnetic simulations and resolution

A particular strength of electron holography is its ability to provide quantitative information about magnetic properties. The magnetic moment of a nanoparticle can be obtained from the relation

$$\boldsymbol{m} = \int\int\int \boldsymbol{M}(\boldsymbol{r}) d^3\boldsymbol{r} \ , \tag{24}$$

where $\boldsymbol{M}(\boldsymbol{r})$ is the position-dependent magnetisation and $\boldsymbol{r}$ is a three-dimensional position vector. Unfortunately, an electron holographic phase image does not provide direct information about $\boldsymbol{M}(\boldsymbol{r})$, but is proportional to the projection (in the electron beam direction) of the in-plane component of the magnetic induction $\boldsymbol{B}(\boldsymbol{r})$ both within and around the specimen. Fortunately, it has been shown that the magnetic moment of an isolated crystal can be measured quantitatively by integrating the gradient of a phase image around the crystal using a circular inegration contour [180]. The resulting measurement is model-independent, does not rely on assumptions such as uniform magnetisation of the particle or a priori knowledge such as the particle's morphology and/or composition, and is free of most artefacts if the calculation is performed as a function of the radius of the integration circle and extrapolated to a circle of zero radius. Furthermore, since the integration loop encloses the object and never crosses its boundaries, the procedure can be applied to a reconstructed phase image without the need for separating the mean inner potential and magnetic contributions to the phase.

A model-based approach for the reconstruction of *magnetization* distributions in nanoscale materials, which involves applying an iterative reconstruction algorithm to one or more magnetic phase images recorded using off-axis electron holography, was also recently developed [181]. The advantage of using a model-based approach is that each trial solution satisfies known physical laws. The initially ill-posed problem was replaced by a least-squares minimization

problem. First order Tikhonov regularization was applied and a mask was used to localize magnetized objects. All measures were combined into a cost function, whose minimization was facilitated by conjugate gradient methods. Diagnostic tools were used to assess the quality of the reconstruction result. Sources of magnetization outside the field of view were accounted for by introducing buffer pixels. A confidence array was used to exclude other identifiable artefacts from the reconstruction. Encouraging experimental results were obtained from the reconstruction of projected magnetization distributions of magnetic skyrmions examined in both extended films and geometrically-confined structures fabricated using FIB milling [167, 168].

In general, the need to compare electron holographic measurements with micromagnetic simulations results from the sensitivity of the magnetic domain structure in nanoscale materials and devices to their detailed magnetic history. Differences in the starting magnetic states on a scale that is too small to be distinguished visually, as well as inter-element coupling and the presence of out-of-plane magnetic fields, are all important for the formation of subsequent domain states, and in particular for the sense (the handedness) with which magnetic vortices unroll [182]. The sensitivity of the magnetic domain structure to such effects emphasizes the need to correlate high quality experimental holographic measurements with micromagnetic simulations. Such comparisons, which have recently been illustrated for samples that include twinned crystals of magnetite [148-150], meteoritic metal intergrowths [183], nanoscale cubes of Fe [184], domain walls in Ni nanocylinders [185] and hard disk drive write poles [186], are facilitated by the availability of software that can convert the results of micromagnetic calculations directly into simulated phase images [150, 181, 187].

The spatial resolution that can be achieved in phase images is determined primarily by the spacing of the holographic interference fringes. However, the contrast of these fringes decreases as their spacing is reduced, and the recording process is also dominated by Poisson-distributed shot noise [188]. These parameters are affected by the illumination diameter, exposure

time and biprism voltage. The final 'phase resolution' [37] and 'spatial resolution' are always inherently linked, in the sense that a small phase shift can be measured with high precision and poor spatial resolution, or with low precision but high spatial resolution. In each of the examples described above, the recorded phase images were always smoothed slightly to remove noise, and the spatial resolution of the magnetic information was estimated typically to be between 5 and 20 nm. This procedure is necessarily subjective, and great care is required to ensure that artifacts are not introduced. Higher spatial and phase resolution can be achieved by recording several holograms of each area of interest and subsequently averaging the resulting phase images [43, 44]. Recently, by using a 1.2 MeV TEM, Tanigaki et al. [189] succeeded in achieving 0.67 nm spatial resolution in magnetic induction mapping of CoFeB/Ta layers using electron holography.

4. Measurement of electrostatic fields

In this Section, the application of electron holography to the characterization of electrostatic fields is reviewed. Initial examples are taken from the characterization of electrostatic fringing fields outside electrically biased nanotips. The challenges that are associated with imaging dopant contrast at depletion layers in semiconductors are then described, before discussing the characterization of interfaces at which both charge redistribution and changes in chemistry can introduce significant local variations in phase shift.

4.1. Electrically biased nanotips

Early experiments on tungsten microtips demonstrated that electron holography could be used to measure electrostatic fringing fields outside electrically biased samples [190]. Susbequent studies were made on pairs of parallel 1-μm-diameter Pt wires held at different potentials [191] and on single conducting wires [192], and simulations were presented for electrostatic phase plates [193]. More recent experiments have involved the use of electron holography to map

electrostatic potentials around the ends of electrically-biased carbon nanotubes and field emitting needles. In one of the first such studies, a three-axis manipulation electrode was used to position a multi-walled carbon nanotube approximately 6 μm from a gold electrode [194], as shown in Fig. 20a. Depending on the applied bias between the nanotube and the gold electrode, electrons were emitted from the nanotube. The left hand column of Fig. 20b shows contoured (wrapped) phase images recorded both before a bias V_b was applied to the specimen, and for a bias above the threshold for field emission (approximately 70 V). The upper phase shift map ($V_b = 0$) is featureless around the nanotube, whereas the lower map ($V_b = 120$ V) shows closely-spaced 2π phase contours. The right hand column in Fig. 20b shows the corresponding phase gradient for each image. When $V_b = 0$, the phase gradient is featureless around the nanotube, whereas it is concentrated around the nanotube tip when $V_b = 120$ V. The images shown in Fig. 20b were interpreted by comparison with simulations, calculated on the assumption that the nanotube could be approximated by a line charge, along which the charge distribution was varied until a close fit to the data was found. The fit to the 120 V phase data in Fig. 20b provided a value of 1.22 V/nm for the electric field at the nanotube tip. This field was stable over time, even when the emission current varied.

[Place Fig. 20 here]

Similar electron holographic observations of phase variations outside biased nanotips were subsequently reported outside $TaSi_2$ nanowires [195] (Kim et al., 2007), cone-shaped carbon nanotips [196-198] and atom probe needles [199, 200].

A model-independent method was recently developed to allow the projected charge density distribution in a TEM specimen to be measured directly from the Laplacian of a recorded electron holographic phase image [201]. Fortuitously, even if the vacuum reference wave that is used to form the electron hologram is perturbed by charges within the region of interest or outside

the field of view, the measurement of the charge within the object is unaffected, unlike the phase image itself. This approach was applied to the measurement of electron-beam-induced charge density in a bundle of single-walled carbon nanotubes [201] and on a MgO nanoparticle [202]. Great care is required to avoid misinterpretation of the charge density distribution recovered using this approach, as a result of contributions to the recorded phase from local variations in mean inner potential and specimen thickness [203].

Figure 21 illustrates the application of off-axis electron holography to the study of an electrically biased Fe needle that contains yttrium oxide nanoparticle inclusions. A voltage was applied between the needle and a counter-electrode that was placed coaxially with the needle at distance of ~400 nm from it [200]. The results were interpreted both by fitting the recorded phase shift to a simulated phase image modeled using two lines of constant but opposite charge density and from the Laplacian of the recorded phase. Both approaches required subtraction of the magnetic contribution to the recorded phase shift (resulting from the fact that the needle is made from ferromagneic Fe and that the microscope was operated in Lorentz mode). This subtraction was achieved by evaluating the difference between phase images recorded at two different bias voltages, as shown in Figs. 21a to c. This approach also automatically results in subtraction of the mean inner potential contribution to the phase shift, which was found to be essential for the latter (Laplacian) approach, as described above. Cumulative charge profiles along the needle measured using the model-independent (Laplacian) approach revealed the presence of charge accumulation at the apex of the needle. On the assumption of cylindrical symmetry, the three-dimensional electrostatic potential and electric field around the needle could be inferred from the results, as shown in Fig. 21d, which shows a central slice of the three-dimensional potential (colours) and electric field (white lines) around the needle.

[Place Fig. 21 here]

4.2. Dopant potentials in semiconductors

An important challenge for electron holography is the quest for a reliable, quantitative approach for the characterization of electrostatic potentials associated with charge redistribution at depletion regions in doped semiconductors. Attempts to tackle this problem have been made since the 1960s using different phase contrast techniques, both experimentally (e.g., [204, 205]) and theoretically (e.g., [206, 207]). It is now recognized that TEM specimen preparation can have a profound effect on phase images of doped semiconductors because of physical damage, pinning of the Fermi level on the free specimen surface or the implantation of dopant ions such as Ar or Ga during ion milling. An electrically inactive near-surface layer and/ or a doped layer, with a thickness that depends on the specimen preparation method, may then form at the sample surface. In addition, the specimen may charge up during observation in the TEM, to such an extent that all dopant contrast is lost. The effects of specimen preparation, and in particular the electrical state of near-surface regions, most likely account for many anomalous results in early experiments. Recent studies indicate that it may be possible to resolve these problems, in particular for specimens that contain high dopant concentrations [208].

The first unequivocal demonstration of two-dimensional mapping of the electrostatic potential in an unbiased doped semiconductor device using electron holography was achieved for metal oxide semiconductor (MOS) Si transistors by Rau et al. [209]. The source and drain regions in the transistors were visible in phase images with a spatial resolution of 10 nm and an energy resolution of close to 0.10 eV. Differential thinning was discounted as a cause of the observed phase shifts, and an optimal specimen thickness of 200 - 400 nm was identified for such experiments. The transistors were prepared for TEM examination using conventional mechanical polishing and Ar ion milling. A 25-nm-thick electrically altered layer was identified on each surface of the specimen, and was reported to be responsible for the value of the measured built-

in voltage of 0.9±0.1 V across each *p-n* junction, which was lower than the value of 1.0 V predicted for the specified dopant concentrations.

Electron holography studies of transistors have subsequently been compared with process simulations [208, 210]. Figure 22a shows a contoured image of the electrostatic potential associated with a 0.35 μm Si device inferred from an electron hologram taken from the work of Gribelyuk et al. [210]. The contours correspond to potential steps of 0.1 V. The B-doped source and drain regions are delineated clearly. In this study, the specimen was prepared using tripod wedge polishing, followed by limited low-angle Ar ion milling at 3.5 kV. Surprisingly, no electrically altered surface layer needed to be taken into account to quantify the results. Figures 22b and c show a comparison between line profiles obtained from Fig. 22a and simulations, both laterally across the junction and with depth from the Si surface. Simulations for 'scaled loss' and 'empirical loss' models, which account for B-implant segregation into the adjacent oxide and nitride layers, are shown. The scaled-loss model, which leads to stronger B diffusion, assumes uniform B loss across the device structure, whereas the empirical loss model assumes segregation of the implanted B at the surfaces of the source and drain regions. In both Fig. 22b and Fig. 22c, the empirical loss model provides a closer match to the experimental results. Figure 22d shows a simulated electrostatic potential map for the same device based on the 'empirical loss' model, which matches closely with the experimental image in Fig. 22a. This study demonstrated successful mapping of the electrostatic potential in 0.13 μm and 0.35 μm device structures with a spatial resolution of 6 nm and a sensitivity of 0.17 eV.

[Place Fig. 22 here]

In early applications of electron holography to dopant delineation, which were carried out on chemically-thinned Si samples under reverse bias conditions (e.g., [211]), differences between phase images recorded at different bias voltages were used to visualize external

electrostatic fringing fields in vacuum close to the positions of *p*-*n* junctions. Electrostatic potential profiles were subsequently measured across reverse-biased Si *p*-*n* junctions that were prepared for TEM examination using FIB milling [212-214]. In this context. it is significant to note that FIB milling is currently the technique of choice for preparing TEM specimens from site-specific regions of integrated circuits. It is therefore important to establish whether electron holography results obtained from unbiased specimens prepared by FIB milling are reliable. It is also important to develop specimen and contacting geometries that allow specimens prepared using this technique to be electrically biased in situ in the TEM.

Although FIB-prepared lamellae containing semiconductor devices can now be routinely electrically biased in commercial specimen holders that are equipped with multiple electrical contacts, here we present results from one of the earliest studies, in which *p*-*n* junctions were prepared for in situ electrical biasing by using a 30 kV FEI 200 FIB workstation to machine parallel-sided electron-transparent membranes at the corners of 1 × 1 mm 90^{o} cleaved squares of wafer that were placed in a home-modified single-tilt holder, as shown schematically in Figs. 23a and 23b. This specimen geometry was chosen because it allowed electrical contacts to be made to the front and back surfaces of the small square of wafer in a home-designed setup. In such studies, care must be taken to expose the region of interest to the focused beam of Ga ions only at a glancing angle to its surface. Figure 23c shows a representative electron holographic phase image recorded from an unbiased Si *p*-*n* junction sample prepared in this geometry using FIB milling. The ‘crystalline’ specimen thickness was measured to be 550 nm using convergent beam electron diffraction. The *p*-type and *n*-type regions are delineated clearly as areas of darker and lighter contrast, respectively. An additional 'gray' band visible at the specimen edge is likely to be associated with the presence of an electrically altered layer, which is visible in cross-section here but is also thought to extend around the entire specimen surface. No electrostatic fringing field is visible outside the specimen, indicating that its surface must be an equipotential. Line

profiles across the junction were obtained from phase images acquired with different reverse bias voltages applied to a specimen of 390 nm crystalline thickness (Fig. 23d), as well as from several unbiased specimens. Each profile in Fig. 23d is qualitatively consistent with the expected potential profile for a *p-n* junction in a specimen of uniform thickness. The height of the potential step across the junction, $\Delta\phi$, increases linearly with reverse bias voltage V_{appl}, as shown in Fig. 23e.

[Place Fig. 23 here]

This behavior is described, to a first approximation, by the equation

$$\Delta\phi = C_E\left(V_{bi} + V_{appl}\right)t_{active} \ , \tag{25}$$

where C_E is defined in Equation 7 and the *p-n* junction is contained in an 'electrically active' layer of thickness t_{active} in a specimen of total thickness t . Measurement of the gradient of the graph shown in Fig. 23e, which is equal to $C_E t_{active}$, provides a value for t_{active} of 340±10 nm, suggesting that 25±5 nm of the crystalline thickness on each surface of the TEM specimen is electrically inactive. The intercept with the vertical axis is $C_E V_{bi} t_{active}$, which provides a value for the built-in voltage across the junction of 0.9±0.1 V. Depletion widths across the junction measured from the line profiles are higher than expected, suggesting that the electrically active dopant concentration in the specimen is lower than the nominal value. The experiments also show that electrical biasing re-activates some of the dopant that has been passivated by specimen preparation [215]. Figure 23f shows a four-times-amplified phase image obtained from a 90° cleaved wedge that had *not* been prepared by FIB milling, for an applied reverse bias of 2 V, where an external electrostatic fringing field is visible outside the specimen edge. Such fringing fields are almost

never observed outside FIB-milled specimens, indicating that the surfaces of TEM specimens prepared by FIB milling are usually equipotentials, even under applied bias.

The importance of minimizing and assessing damage, implantation and specimen thickness variations when examining FIB-milled TEM specimens that contain *p*-*n* junctions has been highlighted by results obtained from unbiased samples (e.g., [216-219]). One of these experiments involved the use of FIB milling to form a 45° specimen thickness profile, from which both the phase change across the junction and the absolute phase shift relative to vacuum on each side of the junction could be plotted as a function of specimen thickness. The slopes of the phase profiles were then used to determine the built-in voltage across the junction, the mean inner potentials on the *p* and *n* sides of the junction, and the electrically altered layer thickness. By using this approach, the mean inner potentials of the *p* and *n* sides of the junction were measured to be 11.50±0.27 and 12.1±0.40 V, respectively. The electrically altered layer thickness was measured to be approximately 25 nm on each surface of the specimen.

In contrast to results obtained from Si specimens of similar thickness, it has been shown that the step in phase across a GaAs *p*-*n* junction is affected more strongly by the effects of sample preparation using FIB milling. Fortunately, both the phase shift across the junction and the signal to noise in recorded phase images can be improved by using low temperature annealing, in order to remove defects resulting from Ga+ implantation and to re-activate dopant atoms. A similar, although smaller, improvement is seen for FIB-milled Si specimens [220]. It is also important to note that the built-in voltage across a *p*-*n* junction can be affected by the choice of electron beam current used during examination in the TEM (and therefore the rate at which charge is dissipated from the area of interest) and that it can then be improved by providing high quality electrical contacts to the region of interest on the TEM specimen [221].

The electrical nature of the surface of a TEM specimen that contains a doped semiconductor can also be assessed by comparing experimental holography results with simulations. Such a comparison of experimental phase images with simulations performed using commercial semiconductor process simulation software [222] suggests that electron-beam-induced positive charging of the surface of a TEM specimen, at a level of 10^{13} to 10^{14} cm^{-2} , can create an inversion layer on the *p*-side of the junction in a thin TEM specimen. This layer may explain the absence of electrostatic fringing fields outside the specimen surface, which would otherwise dominate the observed phase contrast [223]. Figure 24 shows the results of finite-element numerical simulations, in which semi-classical equations were used to determine the charge density and potential in a thin parallel-sided Si sample that contains a *p-n* junction. In the simulations, the Fermi level on the surface of the specimen was set to a single value to ensure that it is an equipotential [224]. The simulations shown in Fig. 24 are for symmetrical junctions, in which the dopant concentrations are 10^{18}, 10^{17} and 10^{16} cm^{-3}. Contours of spacing 0.05 V are added to each figure. Significantly, as either the dopant concentration or the specimen thickness decreases, a correspondingly smaller fraction of the specimen retains electrical properties that are close to those of the bulk device. In the simulations, the average step in potential across the junction through the thickness of the specimen is almost insensitive to the surface state energy and is *always* reduced from that in the bulk device. This reduction is greatest for lower sample thicknesses and lower dopant concentrations. In practice, as a result of additional complications from oxidation, physical damage and implantation, the simulations shown in Fig. 24 are likely to be an underestimate of the full modification of the potential from that in the original device.

[Place Fig. 24 here]

Further calculations of the influence of the electrical state of the specimen surface on the electrostatic potential in a TEM specimen have been performed using calculations based on both density functional theory [225-228] and semiconductor process simulations [208].

The ways in which the sample preparation technique of 'wedge-polishing' affects both the ‘dead layer’ thickness and specimen charging have been explored experimentally for a one-dimensional *p*-*n* junction in Si by McCartney et al. [77]. A specimen was prepared from a *p*-type wafer that had been subjected to a shallow B implant and a deeper P implant, resulting in the formation of an *n*-type well and a *p*-doped surface region. Phase images were obtained before and after coating one side of the specimen with approximately 40 nm of carbon. Profiles obtained from the uncoated sample showed an initial increase in the measured phase going from vacuum into the specimen, then dropping steeply and becoming negative at large thicknesses. This behavior was not observed after carbon coating, suggesting that it is associated with sample charging that results from the electron-beam-induced emission of secondary electrons.

Similar charging effects can be seen directly in two dimensions in Fig. 25. Figure 25a shows a bright-field TEM image of a linear array of transistors, which were originally located ~5 μm below the surface of a wafer and separated from its surface by metallization layers. Such transistors present a significant but representative challenge for TEM specimen preparation for electron holography using FIB milling, both because the metallization layers are substantial and can result in thickness corrugations in the doped regions of interest and because these overlayers must often, at least in part, be removed to provide a vacuum reference wave for electron holography. An additional difficulty results from the possibility that the overlayers, which contain silicon oxides, may charge during examination in the electron microscope. Conventional 'trench' FIB milling [229, 230] was used to prepare the specimen, which has a nominal thickness of 400 nm. Figure 25b shows eight-times-amplified phase contours obtained from the region marked '1' in Fig. 25a. Instead of the expected phase distribution, which should be approximately proportional to the mean inner potential multiplied by the specimen thickness, elliptical contours are visible in each oxide region, and an electrostatic fringing field is present outside the specimen (at the top of Fig. 25b). Both the elliptical contours and the fringing field are associated with the

build-up of positive charge in the oxide. The centers of the elliptical contours are several hundreds of nm from the specimen edge. Figure 25c shows a similar phase image obtained after coating the specimen on one side with approximately 20 nm of carbon. The effects of charging are now absent, there is no fringing field outside the specimen edge, and the phase contours follow the change in specimen thickness. One-dimensional phase profiles were generated from the phase images used to form Figs. 25b and c along the line marked '2' in Fig. 25a, and are shown in Fig. 25d. The dashed and solid lines correspond to results obtained before and after coating the specimen with carbon, respectively, while the dotted line shows the difference between the solid and dashed lines. If the charge is assumed to be distributed through the thickness of the specimen, then the electric field in the oxide is approximately 2×10^7 V/m. This value is just below the breakdown electric field for thermal SiO_2 of 10^8 V/m [231]. Equivalent results obtained from a specimen of 150 nm nominal thickness show that the centers of the elliptical contours in the oxide are closer to the specimen edge. The effect of specimen charging on the dopant potential (in the source and drain regions of the transistors) is just as significant. The phase gradient continues into the substrate, and the dopant potential is undetectable before carbon coating, whether or not a phase ramp is subtracted from the images. If FIB milling from the substrate side of the wafer [232] is used, then specimen charging no longer occurs, presumably as a result of Si (and Ga) deposition onto the specimen surface. McCartney et al. [233] provide an overview of this and other techniques for the preparation of semiconductor devices for electron holography.

[Place Fig. 25 here]

More recent progress in electron holography of semiconductor devices has focused on improving detection limits [234, 235], reducing artefacts [236-238], characterizing ever smaller transistor structures reliably [239-242], analyzing thinner FIB-prepared specimens that contain higher dopant concentrations [208], separating mean inner potential from dopant potential

contributions to phase images for very high dopant concentrations [243], studying working semiconductor devices in situ in the TEM [244] and developing approaches for electron holographic tomography of dopant potentials in thin TEM specimens [83, 90, 245-247].

Although questions still remain about phase contrast observed at simple *p-n* junctions, electron holography has also been used to infer charge redistribution in more complicated semiconductor device structures, in which changes in composition as well as doping concentration are present. One example is provided by a study of a strained *n*-$Al_{0.1}Ga_{0.9}N$/ $In_{0.1}Ga_{0.9}N$/ *p*-$Al_{0.1}Ga_{0.9}N$ heterojunction diode, in which strong piezoelectric and polarization fields induce high two-dimensional electron gas concentrations [248]. In order to interpret experimental measurements of the potential profile across such a heterojunction, after corrections for specimen thickness changes (assuming a linear thickness profile and neglecting contributions to the measured phase from variations in mean inner potential), additional charge had to be added to simulations. In particular, a sheet of negative charge was included at the bottom of the InGaN well. The sheet charge density at this position was $2.1 \times 10^{13} cm^{-2}$. In other similar studies, electron holography has been used to study internal electrostatic potentials across nitride quantum wells [249, 250] and wurtzite GaN quantum dots [251], hole accumulation in Ge/Si core/shell nanowires [252], dislocation cores [253-255], junctions between ZnSe polytypes [256], Pt/Fe:$SrTiO_3$/Nb:$SrTiO_3$ thin-film resistive switching structures [257], electrically biased resistive switching devices based on thin SiO_2 layers [258], core-shell nanowire *p-n* junctions [259, 260], lithiation in Ge nanowires [261], electrically biased solid-state electrolytes [53] and thin film solar cells [262].

4.3. Space charge layers at grain boundaries

Electron holography has also been used to characterize space charge layers at doped and undoped grain boundaries in electroceramics, despite the fact that several contributions to the electron holographic phase shift can often complicate interpretation. The space charge distribution that is predicted to form at such a grain boundary [263] is often described as a double (back-to-back) Schottky barrier. For Mn-doped and undoped grain boundaries in $SrTiO_3$, a decrease in the measured phase shift at the boundary relative to that in the specimen was reported [264]. The changes in phase measured at the doped boundaries were larger in magnitude and spatial extent than at similar undoped boundaries. Possible contributions to the contrast from changes in density, composition, specimen thickness, dynamical diffraction and electrostatic fringing fields [265, 266] were considered, and the remaining contributions to the measured phase shifts at the doped boundaries were attributed to space charge. The sign of the space charge contribution to the specimen potential was consistent with the presence of Mn^{2+} and Mn^{3+} ions on Ti sites at the boundaries. The results were interpreted in terms of a narrow (1-2 nm) region of negative grain boundary charge and a wider (3-5 nm) distribution of positive space charge.

A similar approach has been applied to the characterization of grain boundaries in ZnO, at which a space charge layer width of approximately 150 nm has been measured [267]. Defocus contrast has been used to assess possible space charge contributions to electrostatic potential profiles across grain boundaries in doped and undoped $SrTiO_3$ [268]. The contrast observed in these experiments was not consistent with a dominant contribution to the signal from space charge. Defocus contrast recorded from delta-doped layers in Si and GaAs has also been attributed to the presence of space charge [243, 269]. The possible presence of electrostatic fringing fields outside interfaces in a variety of different TEM specimens has been considered [223, 266, 270, 271].

Although related experiments have been performed in attempts to measure polarization distributions across domain boundaries in ferroelectric materials such as $BaTiO_3$ and $PbTiO_3$ [272-274], it is now recognised that the design and interpretation of such measurements is highly complicated and requires further work [275, 276].

5. High-resolution electron holography

Aberrations of the TEM objective lens, which result in modifications to the amplitude and phase shift of the electron wave, rarely need to be taken into account when characterizing magnetic and electrostatic fields at medium spatial resolution, as described in Sections 3 and 4. However, these aberrations must be considered when interpreting electron holograms that have been acquired at atomic resolution, in which lattice fringes are visible.

The back focal plane of the objective lens contains the Fraunhofer diffraction pattern, i.e., the Fourier transform, of the specimen wave $\psi_s(\boldsymbol{r}) = A_s(\boldsymbol{r})exp[i\phi_s(\boldsymbol{r})]$, denoted $\psi_s(\boldsymbol{r}) = \psi(\boldsymbol{q}) = FT[\psi_s(\boldsymbol{r})]$. Transfer from the back focal plane to the image plane is then represented by an inverse Fourier transform. For a perfect thin lens, neglecting magnification and rotation of the image, the complex image wave would be equivalent to the object wave $\psi_s(\boldsymbol{r})$. Modifications to the electron wave that result from objective lens aberrations can be represented by multiplication of the electron wavefunction in the back focal plane by a transfer function of the form

$$T(\boldsymbol{q}) = B(\boldsymbol{q})exp[i\chi(\boldsymbol{q})] \quad . \tag{26}$$

In Equation 26, $B(\boldsymbol{q})$ is an aperture function that takes a value of unity for q within the objective aperture and zero beyond the edge of the aperture. The effects of two of the most

important objective lens aberrations, defocus and spherical aberration, can be included in the phase factor in the form

$$\chi(\boldsymbol{q}) = \pi\Delta z\lambda q^2 + \frac{\pi}{2}C_S\lambda^3 q^4 \ , \tag{27}$$

where Δz is the defocus of the lens and C_S is the spherical aberration coefficient. The complexity of Equation 27 increases rapidly as further aberrations are considered. The complex wave in the image plane can then be written in the form

$$\psi_i(\boldsymbol{r}) = FT^{-1}[FT[\psi_s(\boldsymbol{r})] \times T(\boldsymbol{q})] \tag{28}$$

$$= \psi_s(\boldsymbol{r}) \otimes t(\boldsymbol{r}) \ , \tag{29}$$

where $t(\boldsymbol{r})$ is the inverse Fourier transform of $T(\boldsymbol{q})$, and the convolution $\otimes$ of the specimen wave $\psi_s(\boldsymbol{r})$ with $t(\boldsymbol{r})$ represents the smearing of information that results from lens imperfections. Since both $\psi_s(\boldsymbol{r})$ and $t(\boldsymbol{r})$ are in general complex, the intensity of a conventional bright-field image, which can be expressed in the form

$$I(\boldsymbol{r}) = [\psi_s(\boldsymbol{r}) \otimes t(\boldsymbol{r})]^2 \tag{30}$$

is no longer related simply to the structure of the specimen.

The effects of lens aberrations can be removed by multiplying the complex image wave by a suitable phase plate corresponding to $T^*(\boldsymbol{q})$ to provide the amplitude and the phase shift of the *specimen* wave $\psi_s(\boldsymbol{r})$ rather than the *image* wave $\psi_i(\boldsymbol{r})$. Hence, the interpretable resolution of the image can be improved beyond the point resolution of the electron microscope. The optimal

defocus that maximizes the resolution of the reconstructed specimen wave after correction of aberrations [277-280] is given by the expression

$$\Delta z_{opt} = -\frac{3}{4} C_S (\lambda q_{max})^2 \ , \tag{30}$$

where q_{max} is the maximum desired spatial frequency.

Figure 26 illustrates one of the first successful applications of aberration correction to a high-resolution electron hologram, in this case for crystalline Si imaged at the <110> zone axis, at which characteristic 'dumbbell' contrast, of spacing 0.136 nm, is expected [281]. The original hologram was acquired using an interference fringe spacing of 0.05 nm on a CM30 FEGTEM, which has a point resolution of 0.198 nm and an information limit of 0.1 nm at 300 kV. Figures 26a and b show, respectively, the reconstructed amplitude and phase shift of the hologram after aberration correction using a phase plate. The phase image reveals the expected white 'dumbbell' contrast, at a spatial resolution that is considerably better than the point resolution of the microscope, after lens aberrations, including residual astigmatism and off-axis coma, have been measured and removed. Note also that the projected atom column positions are visible as black contrast in the amplitude image.

[Place Fig. 26 here]

High-resolution electron holography is clearly an exciting area of research, with many recent developments and applications of the technique to a wide range of materials problems [14, 282-286], including recent successful comparisons between experimental phase and amplitude images of two-dimensional transition metal dichalcogenides with simulations based on density functional theory on an absolute scale [287, 288].

6. Alternative forms of electron holography

Many different forms of electron holography can be envisaged and implemented, both in the TEM and in the scanning TEM (STEM) [289]. Equally, there are several ways in which the off-axis mode of TEM electron holography can be implemented. A full discussion of these various schemes, which include interferometry in the diffraction plane of the microscope [290], reflection electron holography [291] and strain mapping using dark-field electron holography [292-295], is beyond the scope of this Chapter. Here, selected developments are reviewed.

The need for a vacuum reference electron wave is a major drawback of the standard off-axis mode of TEM holography, since this requirement restricts the region that can be examined to near the specimen edge. In many applications, the feature of interest is not so conveniently located. The implementation of split-illumination electron holography [29, 30], an accumulated reconstruction method [31] or a DPC mode of electron holography in the TEM enables this restriction to be overcome. DPC imaging is well-established as a technique in the STEM, involving the use of various combinations of detectors to obtain magnetic contrast [112, 113, 296]. It has also been shown [297] that DPC contrast can be obtained using far-out-of-focus STEM electron holography (see below). An equivalent TEM configuration can be achieved by using an electron biprism located in the condenser aperture plane of the microscope [298]. Figure 27a shows a schematic ray diagram that illustrates the electron-optical configuration for this differential mode of off-axis TEM holography. The application of a positive voltage to the biprism results in the formation of two closely-spaced, overlapping plane waves, which appear to originate from sources S_1 and S_2 to create an interference fringe pattern at the specimen level. When the observation plane is defocused by a distance Δz with respect to the specimen plane, the two coherent beams produced by the beam splitter, which are labeled k_1 and k_2 in Fig. 27a, impinge upon different parts of the specimen. For a magnetic material, the difference in the

component of the magnetic induction parallel to the biprism wire between these two points in the specimen plane determines the relative phase shift of the holographic fringes, thus giving differential phase contrast. Since the hologram is acquired under out-of-focus conditions, it is in effect the superposition of a pair of Fresnel images. The biprism voltage must be adjusted so that the feature of interest or the desired spatial resolution is sampled by at least three interference fringes. An appropriate post-specimen magnification should be chosen to ensure that the interference fringes are properly sampled by the recording medium. Figure 27b shows a composite phase image formed from a series of eight DPC holograms of a 30-nm-thick Co film. The fringe system was shifted progressively across the specimen plane between exposures. In addition to the holographic interference fringes, the image shows black and white lines that delineate walls between magnetic domains, with magnetization ripple visible within the domains. All of the image features are doubled due to the split incident beam. Figure 27c shows the final reconstructed DPC image obtained from Fig. 27b, in which the contrast is proportional to the component of the magnetic induction parallel to the holographic fringes. The arrow below the image indicates the direction of the component of the induction analyzed in this experiment. Several magnetic vortices, at which the measured field direction circles an imperfection in the film, are visible. One such vortex is indicated by an arrow in the lower right corner of the image. For characterization of both components of the in-plane induction without removing the sample from the microscope, a rotating biprism or a rotating sample holder is required.

[Place Fig. 27 here]

An alternative scheme that is conceptually similar to the differential mode of electron holography in the TEM, but which does not require the use of an electron biprism or a field emission electron gun, is termed amplitude division electron holography. Whereas conventional modes of electron holography involve splitting the wavefront of the incident illumination and thus require high spatial coherence to form interference fringes, this coherence requirement can

be removed by dividing the amplitude of the electron beam instead of the wavefront. Division of the amplitude of the electron wave can be achieved by using a crystal film located before the specimen. The lattice fringes of the crystal film are then used as carrier fringes. The original configuration for this scheme involved placing the specimen in the selected-area-aperture plane of the microscope [299, 300]. The specimen can also be inserted into the normal object plane by placing a single-crystal thin film and the sample of interest on top of each other, in close proximity [301]. The single crystal film is then tilted to a strong Bragg condition and used as an electron beam splitter. As a result of the separation of the crystal and the specimen, the hologram plane contains two defocused images of the specimen that are shifted laterally with respect to one another. One of these images is carried by the direct beam and the other by the Bragg-reflected beam. When the distance between the two images is greater than the size of the object, the images separate perfectly and interfere with adjacent plane waves to form an off-axis electron hologram. Because the single crystal is in focus and the object is out of focus, a Fresnel electron hologram of the object is obtained. The defocus of the object can be corrected at the reconstruction stage by using a phase plate, although high coherence of the incident illumination is then required. The coherence used when forming the image therefore determines the spatial resolution of the final reconstructed image. Although amplitude division electron holography has several disadvantages over wavefront division holography, the final phase image is not affected by Fresnel diffraction from the edges of the biprism.

An approach that can be used to increase the phase sensitivity of electron holography is termed phase-shifting electron holography. This approach is based on the acquisition of several off-axis holograms while the phase offset (the initial phase) of the image is changed, either by tilting the incident electron beam or by shifting the biprism [302]. Electron holograms are recorded at successive values of the incident beam tilt, such that the phase is shifted by at least 2π over the image series. The fringe shift can be monitored in the complex Fourier spectra of the holograms. Although three holograms can in principle be used to reconstruct the object wave, in

practice as many holograms as possible should be used to reduce noise. The advantages of the phase-shifting approach are greatly improved phase sensitivity and spatial resolution. Moreover, objects that are smaller than one fringe width can be reconstructed. Care is required if the object is out of focus, as tilting the beam will also induce an image shift between successive images. Very small phase shifts have been observed from individual unstained ferritin molecules using this approach [303]. More recent developments in phase-shifting electron holography have included the assessment and improvement of the precision of the technique [304, 305], applications to specimens that include doped semiconductors [306] and its implementation using alternative approaches such as stage-scanning [307].

Electron holograms can be acquired at video-rate and subsequently digitized and processed individually to record dynamic events, but this procedure is time-consuming. An alternative real-time approach for acquiring and processing holograms has been demonstrated by using a liquid-crystal panel to reconstruct holograms [308]. The holograms are recorded at TV-rate and transferred to a liquid-crystal spatial light modulator, which is located at the output of a Mach-Zender interferometer. The liquid crystal panel is illuminated using a He-Ne laser, and interference micrographs are observed at video rate on the monitor beside the microscope as the specimen is examined. In an alternative configuration, a liquid-crystal panel can also be used as a computer-controlled phase plate to correct for aberrations. More recent approaches for achieving real-time electron holography have focused either on the use of multiple electron biprisms to visualize electromagnetic microfields directly [309, 310] or, more practically, on the use of faster computers for the reconstruction, visualization and and interpretation of recorded electron holograms [311].

Whereas an off-axis electron hologram is formed by the interference of an object and a reference wave that propagate in different directions in the electron microscope, the simplest way of recording an electron hologram without using an electron biprism involves using the

transmitted wave as the reference wave to perform in-line electron holography. Gabor's original paper described the reconstruction of an image by illuminating an in-line hologram with a parallel beam of light and using a spherical aberration correcting plate and an astigmatism corrector. The reconstructed image is, however, disturbed by the presence of a 'ghost' or 'conjugate' twin image [312]. If the hologram is recorded and subsequently illuminated by a plane wave, then the reconstructed image and a defocused conjugate image of the object are superimposed on each other. The most effective method of separating the twin images is to use Fraunhofer in-line holography. Here, in-line holograms are recorded in the Fraunhofer diffraction plane of the object [313, 314]. Under this condition, the conjugate image is so blurred that its effect on the reconstructed image is negligible [315]. Recent work has focused on the development of more advanced model-based [316] and model-independent [317-319] approaches for recovering phase information from in-line electron holograms, as well as on the combined application of in-line and off-axis electron holography [262, 320].

The STEM holographic mode used for DPC imaging, which has similarities with the TEM differential mode of electron holography described above, is a point projection technique in which a stationary beam in a STEM is split by a biprism preceding the sample so that two mutually coherent electron point sources are formed just above the specimen. In this operating mode, the objective lens is excited weakly so that the hologram is formed in the diffraction plane rather than the image plane [321]. By greatly defocusing the objective lens, a shadow image of the object is formed, which has the appearance of a TEM hologram, although it is distorted by spherical aberration and defocus. The image magnification and the separation of the sources relative to the specimen are flexible in this configuration, and can be adjusted by changing the biprism voltage and/ or the objective or post-specimen lens settings. The far-out-of-focus mode of STEM electron holography has been applied to the characterization of a range of magnetic materials [322, 323].

A rapid approach that can be used to visualize equiphase contours, which is termed double-exposure electron holography, involves superimposing a hologram of the specimen onto a reference hologram acquired under identical conditions, with the specimen removed from the field of view [324]. Interference effects between the holographic fringes in the two images then provide widely-spaced, low contrast bright and dark bands that reveal phase contours directly. By defocusing the combined image slightly, the unwanted finely-spaced holographic interference fringes can be removed. The technique has been applied to image both electrostatic and magnetic fields and has recently been extended to the study of time-varying high frequency electromagnetic fields in materials [325, 326].

A related approach involves the use of two parallel or perpendicular electron biprisms to generate an interference pattern between either three or four electron waves, respectively. Equiphase contours are then displayed in the recorded hologram. This method has been used to form images of electric fields outside charged latex and alumina particles, magnetic fields outside ferrite particles [327], and to expose a resist to fabricate a 100-nm-period two-dimensional grating lithographically [328]. It has recently been discussed in the context of the formation of a lattice of nanoscale phase vortices [329]. Two parallel biprisms have also been used to form a 'trapezoidal' biprism, in order to perform double-exposure electron holography with the biprism voltage changed [330] and with the reference wave unaffected by the biprism voltage [331].

7. Discussion and conclusions

In this Chapter, the technique of off-axis electron holography has been described, and its recent application to a wide variety of materials has been reviewed. Results have been presented from the characterization of magnetic fields in arrangements of closely-spaced nanocrystals, patterned elements and nanowires, and electrostatic fields in field emitters and doped semiconductors. In situ experiments, which allow magnetization reversal processes to be

followed and electrostatic fields in working semiconductor devices to be characterized, have been described, and the advantages of using digital approaches to record and analyze electron holograms have been highlighted. High-resolution electron holography and alternative modes of electron holography have also been described. Although the results that have been presented are specific to the dimensions and morphologies of the particular examples chosen, they illustrate the ways in which electron holography can be adapted to tackle different materials problems.

Future developments in electron holography are likely to include the development and application of new forms of electron holography and instrumentation, the application of real-time electron holography to in situ studies of dynamic processes in materials in the presence of applied voltages, fields and elevated or reduced temperature, the experimental measurement of phase shifts of shaped electron wavefunctions [332], the introduction of new approaches for enhancing weak magnetic and electrostatic signals, the formulation of a better understanding of the effect of different TEM sample preparation techniques on phase images recorded from semiconductors and ferroelectrics, the development of approaches to reduce electron beam induced specimen charging and to minimize dynamical contributions to recorded phase images, use of sophisticated simulations to model fringing fields outide TEM specimens [53], the development of new theoretical descriptions of electron holography [333] and the combination of electron holography with electron tomography to record both electrostatic and magnetic fields *inside* nanostructured materials in *three* dimensions rather than simply in projection [83, 91-93, 245-247, 333-337]. In the application of electron holographic tomography to the characterization of magnetic vector fields inside materials in three dimensions, a significant challenge lies in the measurement and subtraction of the unwanted mean inner potential contribution to the measured phase shift at every one of the tilt angles required.

The unique capability of electron holography to provide quantitative information about magnetic and electrostatic fields in materials at a resolution approaching the nanometer scale,

coupled with the increasing availability of field-emission-gun transmission electron microscopes and quantitative digital recording, ensure that the technique has a very promising future.

Acknowledgments

The authors are grateful to T. Almeida, J. Barthel, M. Beleggia, S. Blügel, C.B. Boothroyd, T.J. Bromwich, R.F. Broom, P.R. Buseck, J. Caron, S. Chang, R.K.K. Chong, D. Cooper, P. Diehle, H. Du, C. Dwyer, R.B. Frankel, M. Farle, I. Farrer, J.M. Feinberg, P.E. Fischione, R.B. Frankel, K. Harada, R.J. Harrison, L.J. Heyderman, M.J. Hÿtch, B.E. Kardynal, N. Kiselev, M. Kläui, J. Li, Z.-A. Li, J.C. Loudon, D. Meertens, P.A. Midgley, V. Migunov, A.R. Muxworthy, S.B. Newcomb, P. Parameswaran, A.K. Petford-Long, M. Pósfai, G. Pozzi, A. Putnis, D.A. Ritchie, A.C. Robins, C.A. Ross, M.R. Scheinfein, K. Shibata, E.T. Simpson, E. Snoeck, A.H. Tavabi, Y. Tokura, A. Tonomura, S.L. Tripp, A.C. Twitchett-Harrison, A. Wei, W. Williams, F. Winkler, S. Yazdi, F. Zheng and Y. Zhu for discussions and ongoing collaborations. The research leading to these results has received funding from the European Research Council under the European Union's Seventh Framework Programme (FP7/2007-2013)/ ERC grant agreement number 320832.

Acronyms

CCD	charge coupled device
DMI	Dzyaloshinskii-Moriya interaction
DPC	differential phase contrast
FC	flux closure
FEG	field emission gun
FIB	focused ion beam
MOS	metal oxide semiconductor
STEM	scanning transmission electron microscope/microscopy
TEM	transmission electron microscope/microscopy

References

1. D. Gabor: Microscopy by reconstructed wave-fronts, Proc. R. Soc. London A **197**, 454-487 (1949)
2. A. Tonomura, L.F. Allard, G. Pozzi, D.C. Joy, Y.A. Ono (Eds.): *Electron Holography* (Elsevier, Amsterdam 1992)
3. A. Tonomura: *The Quantum World Unveiled by Electron Waves* (World Scientific, Singapore, 1998)
4. E. Völkl, L.F. Allard, D.C. Joy (Eds.): *Introduction to Electron Holography* (Plenum, New York 1998)
5. G. Pozzi: *Microscopia e olografia con elettroni* (Bononia University Press, Bologna 2013)
6. G. Pozzi: Particles and Waves in Electron Optics and Microscopy, In: *Advances in Imaging and Electron Physics*, Vol. 194, ed. by P.W. Hawkes (Academic Press 2016)
7. A. Tonomura: Electron-holographic interference microscopy, Adv. Phys. **41**, 59-103 (1992)
8. P.A. Midgley: An introduction to off-axis electron holography, Micron **32**, 167-184 (2001)
9. H. Lichte: Electron interference: mystery and reality, Phil. Trans. R. Soc. Lond. A **360**, 897-920 (2002)
10. G. Matteucci, G.F. Missiroli, G. Pozzi: Electron holography of long-range electrostatic fields, In: *Advances in Imaging and Electron Phys*., Vol. 122, ed. by P.W. Hawkes (Academic Press 2002), pp. 173-249
11. R.E. Dunin-Borkowski, M.R. McCartney, D.J. Smith: Electron holography of nanostructured materials, In: *Encyclopaedia of Nanoscience and Nanotechnology*, Vol. 3, ed. by H.S. Nalwa (American Scientific Publishers, Stevenson Ranch, California 2004) pp. 41-100
12. R.E. Dunin-Borkowski, T. Kasama, A. Wei, S.L. Tripp, M.J. Hÿtch, E. Snoeck, R.J. Harrison, A. Putnis: Off-axis electron holography of magnetic nanowires and chains,

rings, and planar arrays of magnetic nanoparticles, Microsc. Res. Techn. **64**, 390-402 (2004)

13. M.R. McCartney, D.J. Smith: Electron holography: phase imaging with nanometer resolution, Annu. Rev. Mater. Res. **37**, 729-767 (2007)
14. H. Lichte, M. Lehmann: Electron holography - basics and applications, Rep. Prog. Phys. **71**, 016102 (2008)
15. J.M. Thomas, E.T. Simpson, T. Kasama, R.E. Dunin-Borkowski: Electron holography for the study of nanomagnetic materials, Acc. Chem. Res. **41**, 665-674 (2008)
16. P.A. Midgley, R.E. Dunin-Borkowski: Electron tomography and holography in materials science, Nature Materials **8**, 271-280 (2009)
17. G. Pozzi, M. Beleggia, T. Kasama, R.E. Dunin-Borkowski: Interferometric methods for mapping static electric and magnetic fields, Comptes Rendus Physique **15**, 126-139 (2014)
18. T. Tanigaki, K. Harada, Y. Murakami, K. Niitsu, T. Akashi, Y. Takahashi, A. Sugawara, D. Shindo: New trend in electron holography, J. Phys. D: Applied Physics **49**, 244001 (2016)
19. G. Möllenstedt, H. Düker: Fresnelscher Interferenzversuch mit einem Biprisma für Elektronenwellen, Naturwissenschaften **42**, 41-41 (1954)
20. G. Matteucci, G.F. Missiroli, G. Pozzi: Electron holography of long-range electrostatic fields, Adv. in Imaging and Electron Phys. **99**, 171-240 (1998)
21. P.F. Fazzini, P.G. Merli, G. Pozzi: Electron microscope calibration for the Lorentz mode, Ultramicroscopy **99**, 201-209 (2004)
22. J. Sickmann, P. Formánek, M. Linck, U. Muehle, H. Lichte: Imaging modes for potential mapping in semiconductor devices by electron holography with improved lateral resolution, Ultramicroscopy **111**, 290-302 (2011)
23. L. Reimer: *Transmission Electron Microscopy* (Springer-Verlag, Berlin 1991)
24. W.J. de Ruijter, J.K. Weiss: Detection limits in quantitative off-axis electron holography, Ultramicroscopy **50**, 269-283 (1993)

25. D.J. Smith, W.J. de Ruijter, J.K. Weiss, M.R. McCartney: Quantitative electron holography. In: *Introduction to Electron Holography*, ed. by E. Völkl, L.F. Allard, D.C. Joy (Kluwer Academic/ Plenum Publishers, New York 1998), pp. 107-124

26. W.J. de Ruijter: Imaging properties and applications of slow-scan charge-coupled device cameras suitable for electron microscopy, Micron **26**, 247-275 (1995)

27. R.R. Meyer, A.I. Kirkland: Characterisation of the signal and noise transfer of CCD cameras for electron detection, Micr. Res. Techn. **49**, 269-280 (2000)

28. S.L.Y. Chang, C. Dwyer, J. Barthel, C.B. Boothroyd, R.E. Dunin-Borkowski: Performance of a direct detection camera for off-axis electron holography, Ultramicroscopy **161**, 90-97 (2016)

29. H. Lichte, G. Möllenstedt: Measurement of the roughness of supersmooth surfaces using an electron mirror interference microscope, J. Phys. E: Sci. Instrum. **12**, 941-944 (1979)

30. T. Tanigaki, Y. Inada, S. Aizawa, T. Suzuki, H.S. Park, T. Matsuda, A. Taniyama, D. Shindo, A. Tonomura: Split-illumination electron holography, Appl. Phys. Lett. **101**, 043101 (2012)

31. K. Harada, H. Kasai: Accumulated reconstruction method for electron holography, Microsc. Microanal. **20**, 248-249 (2014)

32. D.C. Ghiglia, M.D. Pritt: *Two-Dimensional Phase Unwrapping. Theory, Algorithms and Software* (Wiley, New York 1998)

33. D.J. Smith, M.R. McCartney: Practical electron holography. In: *Introduction to Electron Holography*, ed. by E. Völkl, L.F. Allard, D.C. Joy (Kluwer Academic/ Plenum Publishers, New York 1998), pp. 87-106

34. M. Lehmann: Influence of the elliptical illumination on acquisition and correction of coherent aberrations in high-resolution electron holography, Ultramicroscopy **100**, 9-23 (2004)

35. E. Völkl, L.F. Allard, A. Datye, B. Frost: Advanced electron holography: a new algorithm for image processing and a standardized quality test for the FEG electron microscope, Ultramicroscopy **58**, 97-103 (1995)

36. S.L.Y. Chang, C. Dwyer, C.B. Boothroyd, R.E. Dunin-Borkowski: Optimising electron holography in the presence of partial coherence and instrument instabilities, Ultramicroscopy **151,** 37-45 (2015)

37. A. Harscher, H. Lichte: Experimental study of amplitude and phase detection limits in electron holography, Ultramicroscopy **64**, 57-66 (1996)

38. H. Lichte: Performance limits of electron holography, Ultramicroscopy **108**, 256-262 (2008)

39. E. Völkl: Noise in off-axis type holograms including reconstruction and CCD camera parameters, Ultramicroscopy **110**, 199-210 (2010)

40. E. Völkl, D. Tang: Approaching routine 2π/1000 phase resolution for off-axis type holography, Ultramicroscopy **110**, 447-459 (2010)

41. F. Röder, A. Lubk, D. Wolf, T. Niermann: Noise estimation for off-axis electron holography, Ultramicroscopy **144**, 32-42 (2014)

42. H. Lichte: Electron holography: state and experimental steps towards 0.1 nm with the CM30-Special Tübingen, In: *Electron Holography*, ed. by A. Tonomura, L.F. Allard, G. Pozzi, D.C. Joy, Y.A. Ono (Elsevier, Amsterdam 1995), pp. 11-31

43. T. Niermann, M. Lehmann: Averaging scheme for atomic resolution off-axis electron holograms, Micron **63**, 28-34 (2014)

44. R.A. McLeod, M. Bergen, M. Malac: Phase measurement error in summation of electron holography series, Ultramicroscopy **141**, 38-50 (2014)

45. K. Yamamoto, T. Tanji, M. Hibino: Hologram simulation for off-axis electron holography, Ultramicroscopy **85**, 35-49 (2000)

46. M.A. Schofield, M. Beleggia, Y. Zhu, G. Pozzi: Characterization of JEOL 2100F Lorentz-TEM for low-magnification electron holography and magnetic imaging, Ultramicroscopy **108**, 625-634 (2008)

47. T. Fujita, M.R. McCartney: Phase recovery for electron holography using Gerchberg–Papoulis iterative algorithm, Ultramicroscopy **102**, 279-286 (2005)

48. K. Harada, A. Tonomura, Y. Togawa, T. Akashi, T. Matsuda: Double-biprism electron interferometry, Appl. Phys. Lett. **84**, 3229-3231 (2004)

49. K. Yamamoto, T. Hirayama, T. Tanji: Off-axis electron holography without Fresnel fringes, Ultramicroscopy **101**, 265-269 (2004)

50. K. Harada, T. Matsuda, A. Tonomura, T. Akashi, Y. Togawa: Triple-biprism electron interferometry, J. Appl. Phys. **99**, 113502 (2006)

51. T. Tanigaki, S. Aizawa, H.S. Park, T. Matsuda, K. Harada, D. Shindo: Advanced split-illumination electron holography without Fresnel fringes, Ultramicroscopy **137**, 7-11 (2014)

52. G. Matteucci, M. Muccini, U. Hartmann: Flux measurements on ferromagnetic microprobes by electron holography, Phys. Rev. B **50**, 6823-6828 (1994)

53. Y. Aizawa, K. Yamamoto, T. Sato, H. Murata, R. Yoshida, C.A. Fisher, T. Kato, Y. Iriyama, T. Hirayama: In situ electron holography of electric potentials inside a solid-state electrolyte: Effect of electric-field leakage, Ultramicroscopy **178**, 20-26 (2017)

54. J.C.H. Spence: On the accurate measurement of structure-factor amplitudes and phases by electron diffraction, Acta Crystallogr. A **49**, 231-260 (1993)

55. P.A. Doyle, P.S. Turner: Relativistic Hartree–Fock X-ray and electron scattering factors, Acta Crystallogr. A **24**, 390-397 (1968)

56. D. Rez, P. Rez, I. Grant: Dirac–Fock calculations of X-ray scattering factors and contributions to the mean inner potential for electron scattering, Acta Crystallogr., Sect. A **50**, 481-497 (1994)

57. G. Radi: Complex lattice potentials in electron diffraction calculated for a number of crystals, Acta Crystallogr. A **26**, 41-56 (1970)

58. M. Gajdardziska-Josifovska, A. Carim: Applications of electron holography. In: *Introduction to Electron Holography*, ed. by E. Völkl, L.F. Allard, D.C. Joy (Kluwer Academic/ Plenum Publishers, New York 1998), pp. 267-294

59. M. Gajdardziska-Josifovska, M.R. McCartney, W.J. de Ruijter, D.J. Smith, J.K. Weiss, J.M. Zuo: Accurate measurements of mean inner potential of crystal wedges using digital electron holograms, Ultramicroscopy **50**, 285-299 (1993)

60. W.J. de Ruijter, M. Gajdardziska-Josifovska, M.R. McCartney, R. Sharma, D.J. Smith, J.K. Weiss: Quantification of high-resolution lattice images and electron holograms, Scanning Microscopy Suppl. **6**, 347-357 (1992)

61. J. Li, M.R. McCartney, R.E. Dunin-Borkowski, D.J. Smith: Determination of mean inner potential of germanium using electron holography, Acta Crystallogr. A **55**, 652-658 (1999)

62. W.D. Rau, F.H. Baumann, J.A. Rentschler, P.K. Roy, A. Ourmazd: Characterization of stacked gate oxides by electron holography, Appl. Phys. Lett. **68**, 3410-3412 (1996)

63. Y.C. Wang, T.M. Chou, M. Libera, T.F. Kelly: Transmission electron holography of silicon nanospheres with surface oxide layers, Appl. Phys. Lett. **70**, 1296-1298 (1997)

64. Ding, Y., Liu, Y., Pradel, K.C., Bando, Y., Fukata, N., Wang, Z.L.: Quantifying mean inner potential of ZnO nanowires by off-axis electron holography, Micron, **78**, 67-72 (2015)

65. A. Harscher, H. Lichte: Inelastic mean free path and mean inner potential of carbon foil and vitrified ice measured with electron holography, In: H.A. Calderón Benavides, M.J. Yacamán (Eds.): Electron Microscopy 98 **1**. Paper presented at the 14th International Conference on Electron Microscopy, Cancun (Institute of Physics Publishing, Bristol 1998), pp. 553-554

66. I. MacLaren, L. Wang, D. McGrouther, A.J. Craven, S. McVitie, R. Schierholz, A. Kovács, J. Barthel, R.E. Dunin-Borkowski: On the origin of differential phase contrast

at a locally charged and globally charge-compensated domain boundary in a polar-ordered material, Ultramicroscopy **154**, 57-63 (2015)

67. R.E. Dunin-Borkowski, C.B. Boothroyd, M. Beleggia: Dynamical effects in the study of supported nanocrystals using electron holography, Microsc. Microananal. **16 Suppl. 2**, 572-573 (2010)

68. A. Lubk, D. Wolf, H. Lichte: The effect of dynamical scattering in off-axis holographic mean inner potential and inelastic mean free path measurements, Ultramicroscopy **110**, 438-446 (2010)

69. S.M. Kathmann, I.F.W. Kuo, C.J. Mundy, G.K. Schenter: Understanding the surface potential of water, J. Phys. Chem. B **115**, 4369-4377 (2011)

70. B. Sellner, S.M. Kathmann: A matter of quantum voltages, J. Chem. Phys. **141**, 18C534 (2014)

71. M. Shirai, T. Tanigaki, S. Aizawa, H.S. Park, T. Matsuda, D. Shindo: In situ electron holographic study of Ionic liquid, Ultramicroscopy **146**, 125-129 (2014)

72. T. Prozorov, T.P. Almeida, A. Kovács, R.E. Dunin-Borkowski: Off-axis electron holography of bacterial cells and magnetic nanoparticles in liquid, J. R. Soc. Interface **14**, 20170464 (2017)

73. L. Ortolani, F. Houdellier, M. Monthioux, E. Snoeck, V. Morandi: Surface electrostatic potentials in carbon nanotubes and graphene membranes investigated with electron holography, Carbon **49**, 1423-1429 (2011)

74. D. Cooper, C.T. Pan, S. Haigh: Atomic resolution electrostatic potential mapping of graphene sheets by off-axis electron holography, J. Appl. Phys. **115**, 233709 (2014)

75. M. O'Keeffe, J.C.H. Spence: On the average Coulomb potential (Φ_0) and constraints on the electron density in crystals, Acta Crystallogr. A **50**, 33-45 (1994)

76. S.J. Lloyd, R.E. Dunin-Borkowski, C.B. Boothroyd: The determination of the ionicity of sapphire using energy filtered high resolution electron microscopy, Inst. Phys. Conf. Ser. **153**, 113-116 (1997)

77. M.R. McCartney, M.A. Gribelyuk, J. Li, P. Ronsheim, J.S. McMurray, D.J. Smith: Quantitative analysis of one-dimensional dopant profile by electron holography, Appl. Phys. Lett. **80**, 3213-3215 (2002)

78. K.H. Downing, M.R. McCartney, R.M. Glaeser: Experimental characterization and mitigation of specimen charging on thin films with one conducting layer, Microsc. Microanal. **10**, 783-789 (2004)

79. M.R. McCartney: Characterization of charging in semiconductor device materials by electron holography, J. Electron Microsc. **54**, 239-242 (2005)

80. R.E. Dunin-Borkowski, S.B. Newcomb, T. Kasama, M.R. McCartney, M. Weyland, P.A. Midgley: Conventional and back-side focused ion beam milling for electron holography of electrostatic potentials in transistors, Ultramicroscopy **103**, 67-81 (2005)

81. T. Latychevskaia, F. Wicki, J.N. Longchamp, C. Escher, H.W. Fink: Direct observation of individual charges and their dynamics on graphene by low-energy electron holography, Nano Letters **16**, 5469-5474 (2016)

82. M.R. McCartney, M. Gajdardziska-Josifovska: Absolute measurement of normalized thickness, t/λi, from off-axis electron holography, Ultramicroscopy **53**, 283-289 (1994)

83. A. Lubk, D. Wolf, F. Kern, F. Röder, P. Prete, N. Lovergine, H. Lichte: Nanoscale three-dimensional reconstruction of elastic and inelastic mean free path lengths by electron holographic tomography, Appl. Phys. Lett. **105**, 173101 (2014)

84. J.K. Weiss, W.J. de Ruijter, M. Gajdardziska-Josifovska, D.J. Smith, E. Völkl, H. Lichte: Applications of electron holography to multilayer interfaces. In: Proceedings of the 49th EMSA Meeeting, ed. by G.W. Bailey (San Francisco Press, San Francisco 1991), pp. 674-675

85. J.K. Weiss, W.J. de Ruijter, M. Gajdardziska-Josifovska, M.R. McCartney, D.J. Smith: Applications of electron holography to the study of interfaces, Ultramicroscopy **50**, 301-311 (1993)

86. L.F. Allard, E. Völkl, A. Carim, A.K. Datye, R. Ruoff: Morphology and crystallography of nano-particulates revealed by electron holography, Nano. Mater. **7**, 137-146 (1996)

87. X. Lin, V.P. Dravid: Mapping the potential of graphite nanotubes with electron holography, Appl. Phys. Lett. **69**, 1014-1016 (1996)

88. K. Aoyama, Q. Ru: Electron holographic observation for biological specimens: electron holography of bio-specimens, J. Microscopy **182**, 177-185 (1996)

89. A. Tonomura, T. Matsuda, T. Kawasaki, J. Endo, N. Osakabe: Sensitivity-enhanced electron-holographic interferometry and thickness-measurement applications at atomic scale, Phys. Rev. Lett. **54**, 60-62 (1985)

90. D. Wolf, A. Lubk, F. Röder, H. Lichte: Electron holographic tomography, Current Opinion in Solid State and Materials Science **17**, 126-134 (2013)

91. G. Lai, K. Hirayama, T. Ishizuka, T. Tanji, A. Tonomura: Three-dimensional reconstruction of electric-potential distribution in electron-holographic interferometry, Appl. Opt. **33**, 829-833 (1994)

92. T. Fujita, M. Chen: Quantitative electron holographic tomography for a spherical object, J. Electron Microsc. **58**, 301-304 (2009)

93. T. Tanigaki, S. Aizawa, T. Suzuki, A. Tonomura: Three-dimensional reconstructions of electrostatic potential distributions with 1.5-nm resolution using off-axis electron holography, J. Electron Microsc. **61**, 77-84 (2012)

94. T. Uhlig, M. Heumann, J. Zweck: Development of a specimen holder for in situ generation of pure in-plane magnetic fields in a transmission electron microscope, Ultramicrosopy **94**, 193-196 (2003)

95. G. Yi, W.A.P. Nicholson, C.K. Lim, J.N. Chapman, S. McVitie, C.D.W. Wilkinson: A new design of specimen stage for in situ magnetising experiments in the transmission electron microscope, Ultramicroscopy **99**, 65-72 (2004)

96. M. Inoue, T. Tomita, M. Naruse, Z. Akase, Y. Murakami, D. Shindo: Development of a magnetizing stage for in situ observations with electron holography and Lorentz microscopy, J. Electron Microsc. **54**, 509-513 (2005)

97. J. Cumings, E. Olsson, A.K. Petford-Long, Y. Zhu: Electric and magnetic phenomena studied by in situ transmission electron microscopy, MRS Bull. **33**, 101-106 (2008)

98. M. Arita, R. Tokuda, K. Hamada, Y. Takahashi: Development of TEM holder generating in-plane magnetic field used for in-situ TEM observation, Mat. Trans. **55**, 403-409 (2014)

99. L. Marton: Electron optical "Schlieren" effect, J. Appl. Phys. **19**, 687-688 (1948)

100. L. Marton: Electron optical observation of magnetic fields, J. Appl. Phys. **19**, 863-864 (1948)

101. L. Marton, S.H. Lachenbruch: Electron optical mapping of electromagnetic fields, J. Appl. Phys. **20**, 1171-1182 (1949)

102. T. Matsuda, A. Tonomura, R. Suzuki, J. Endo, N. Osakabe, H. Umezaki, H. Tanabe, Y. Sugita, H. Fujiwara: Observation of microscopic distribution of magnetic fields by electron holography, J. Appl. Phys. **53**, 5444-5446 (1982)

103. N. Osakabe, K. Yoshida, Y. Horiuchi, T. Matsuda, H. Tanabe, T. Okuwaki, J. Endo, H. Fujiwara, A. Tonomura: Observation of recorded magnetization pattern by electron holography, Appl. Phys. Lett. **42**, 746-748 (1983)

104. T. Matsuda, S. Hasegawa, M. Igarashi, T. Kobayashi, M. Naito, H. Kajiyama, J. Endo, N. Osakabe, A. Tonomura, R. Aoki: Magnetic field observation of a single flux quantum by electron-holographic interferometry, Phys. Rev. Lett. **62**, 2519-2522 (1989)

105. T. Matsuda, A. Fukuhara, T. Yoshida, S. Hasegawa, A. Tonomura, Q. Ru: Computer reconstruction from electron holograms and observation of fluxon dynamics, Phys. Rev. Lett. **66**, 457-460 (1991)

106. J.E. Bonevich, K. Harada, T. Matsuda, H. Kasai, T. Yoshida, G. Pozzi, A. Tonomura: Electron holography observation of vortex lattices in a superconductor, Phys. Rev. Lett. **70**, 2952-2955 (1993)

107. W. Ehrenberg, R.E. Siday: The refractive index in electron optics and the principles of dynamics, Proc. Phys. Soc. Lond. B **62**, 8-21 (1949)

108. Y. Aharonov, D. Bohm: Significance of electromagnetic potentials in the quantum theory, Phys. Rev. **115**, 485-491 (1959)

109. A. Tonomura, T. Matsuda, R. Suzuki, A. Fukuhara, N. Osakabe, H. Umezaki, J. Endo, K. Shinagawa, Y. Sugita, H. Fujiwara: Observation of Aharonov-Bohm effect by electron holography, Phys. Rev. Lett. **48**, 1443-1446 (1982)

110. A. Tonomura, H. Umezaki, T. Matsuda, N. Osakabe, J. Endo, Y. Sugita: Is magnetic flux quantized in a toroidal ferromagnet?, Phys. Rev. Lett. **51**, 331-334 (1983)

111. J.N. Chapman: The investigation of magnetic domain structures in thin foils by electron microscopy, J. Phys. D: Appl. Phys. **17**, 623-647 (1984)

112. N.H. Dekkers, H. de Lang: Differential phase contrast in a STEM, Optik **41**, 452-456 (1974)

113. J.N. Chapman, P.E. Batson, E.M. Waddell, R.P. Ferrier: The direct determination of magnetic domain wall profiles by differential phase contrast electron microscopy, Ultramicroscopy **3**, 203-214 (1978)

114. K.J. Kirk, S. McVitie, J.N. Chapman, C.D.W. Wilkinson: Imaging magnetic domain structure in sub-500 nm thin film elements, J. Appl. Phys. **89**, 7174-7176 (2001)

115. M.R. McCartney, Y. Zhu: Induction mapping of $Nd_2Fe_{14}B$ magnetic domains by electron holography, Appl. Phys. Lett. **72**, 1380-1382 (1998)

116. A. Kovács, K.G. Pradeep, G. Herzer, D. Raabe, R.E. Dunin-Borkowski: Magnetic microstructure in a stress-annealed $Fe_{73.5}Si_{15.5}B_7Nb_3Cu_1$ soft magnetic alloy observed using off-axis electron holography and Lorentz microscopy, AIP Advances **6**, 056501 (2016)

117. M. De Graef, T. Nuhfer, M.R. McCartney: Phase contrast of spherical magnetic particles, J. Microsc. **194**, 84-94 (1999)

118. D.J. Wohlleben: Magnetic phase contrast. In: *Electron Microscopy in Materials Science*, ed. by U. Valdré, Vol. 2 (Academic Press, New York 1971), pp. 712-757

119. A. Tonomura, T. Matsuda, J. Endo, T Arii., K. Mihama: Holographic interference electron microscopy for determining specimen magnetic structure and thickness distribution, Phys. Rev. B: Solid State **34**, 3397-3402 (1986)

120. R.E. Dunin-Borkowski, M.R. McCartney, D.J. Smith, S.S.P. Parkin: Towards quantitative electron holography of magnetic thin films using in situ magnetisation reversal, Ultramicroscopy **74**, 61-73 (1998)

121. R.P. Blakemore: Magnetotactic bacteria, Science **190**, 377-379 (1975)

122. D.A. Bazylinski, B.M. Moskowitz: Microbial biomineralization of magnetic iron minerals; microbiology, magnetism and environmental significance, Reviews in Mineralogy and Geochemistry **35**, 181-223 (1997)

123. D.J. Dunlop, Ö. Özdemir: *Rock Magnetism* (Cambridge Univ. Press, Cambridge 1997)

124. R.E. Dunin-Borkowski, M.R. McCartney, R.B. Frankel, D.A. Bazylinski, M. Posfai, P.R. Buseck: Magnetic microstructure of magnetotactic bacteria by electron holography, Science **282**, 1868-1870 (1998)

125. R.E. Dunin-Borkowski, M.R. McCartney, M. Posfai, R.B. Frankel, D.A. Bazylinski, P.R. Buseck: Off-axis electron holography of magnetotactic bacteria: magnetic microstructure of strains MV-1 and MS-1, Eur. J. Mineral. **13**, 671-684 (2001)

126. E.T. Simpson, T. Kasama, M. Posfai, P.R. Buseck, R.J. Harrison, R.E. Dunin-Borkowski: Magnetic induction mapping of magnetite chains in magnetotactic bacteria at room temperature and close to the Verwey transition using electron holography, J. Phys. Conf. Ser. **17**, 108-121 (2005)

127. T. Kasama, M. Posfai, R.K.K. Chong, A.P. Finlayson, P.R. Buseck, R.B. Frankel, R.E. Dunin-Borkowski: Magnetic properties, microstructure, composition and morphology

of greigite nanocrystals in magnetotactic bacteria from electron holography and tomography, American Mineralogist **91**, 1216-1229 (2006)

128. T.P. Almeida, T. Kasama, A.R. Muxworthy, W. Williams, L. Nagy, T.W. Hansen, P.D. Brown, R E. Dunin-Borkowski: Visualised effect of oxidation on chemical remanent magnetisation of pseudo-single-domain magnetite particles, Nature Communications **5**, 5154 (2014)

129. T.P. Almeida, T. Kasama, A.R. Muxworthy, W. Williams, L. Nagy, R.E. Dunin-Borkowski: Observing thermomagnetic stability of non-ideal magnetite particles: Good paleomagnetic recorders?, Geophysical Research Letters **41**, 7041-7047 (2014)

130. T.P. Almeida, A.R. Muxworthy, T. Kasama, W. Williams, C.D. Damsgaard, C. Frandsen, T.J. Pennycook, R.E. Dunin-Borkowski: Effect of maghemization on the magnetic properties of non-stoichiometric pseudo-single-domain magnetite particles, Geochemistry, Geophysics, Geosystems **16**, 2969-2979 (2015)

131. T.P. Almeida, A.R. Muxworthy, A. Kovács, W. Williams, L. Nagy, P. Ó Conbhuí, C. Frandsen, R. Supakulopas, R.E. Dunin-Borkowski: Direct observation of the thermal demagnetization of a vortex structure held by a non-ideal magnetite recorder, Geophysical Research Letters **43**, 8426-8434 (2016)

132. T.P. Almeida, A.R. Muxworthy, A. Kovács, W. Williams, P.D. Brown, R.E. Dunin-Borkowski: Direct visualization of the thermomagnetic behavior of pseudo-single-domain magnetite particles, Science Advances **2**, e1501801 (2016)

133. V. Reichel, A. Kovács, M. Kumari, É. Bereczk-Tompa, E. Schneck, P. Diehle, M. Pósfai, A.M. Hirt, M. Duchamp, R.E. Dunin-Borkowski, D. Faivre: Single crystalline superstructured stable single domain magnetite nanoparticles, Scientific Reports **7**, 45484 (2017)

134. S.L. Tripp, S.V. Pusztay, A.E. Ribbe, A. Wei: Self-assembly of cobalt nanoparticle rings, J. Am. Chem. Soc. **124**, 7914-7915 (2002)

135. S.L. Tripp, R.E. Dunin-Borkowski, A. Wei: Flux closure in self-assembled cobalt nanoparticle rings, Angew. Chemie **42**, 5591-5593 (2003)

136. T. Kasama, R.E. Dunin-Borkowski, M.R. Scheinfein, S.L. Tripp, J. Liu, A. Wei: Reversal of flux closure states in cobalt nanoparticle rings with coaxial magnetic pulses, Adv. Mat. **20**, 4248-4252 (2008)

137. A. Wei, S.L. Tripp, J. Liu, T. Kasama, R.E. Dunin-Borkowski: Calixarene-stabilized cobalt nanoparticle rings: self-assembly and collective magnetic properties, Supramolecular Chemistry **21**, 189-195 (2009)

138. A. Wei, T. Kasama, R.E. Dunin-Borkowski: Self-assembly and flux closure studies of magnetic nanoparticle rings, J. Mater. Chem. **21**, 16686-16693 (2011)

139. I.S. Jacobs, C.P. Bean: An approach to elongated fine-particle magnets, Phys. Rev. **100**, 1060-1067 (1955)

140. M.J. Hÿtch, R.E. Dunin-Borkowski, M.R. Scheinfein, J. Moulin, C. Duhamel, F. Mazelayrat, Y. Champion: Vortex flux channeling in magnetic nanoparticle chains, Phys. Rev. Lett. **91**, 257207 (2003)

141. P. Barpanda, T. Kasama, R.E. Dunin-Borkowski, M.R. Scheinfein, A.S. Arrott: Evolution and propagation of magnetic vortices in chains of permalloy nanospheres, J. Appl. Phys. **99**, 08G103 (2006)

142. P. Barpanda, M.R. Scheinfein, T. Kasama, R.E. Dunin-Borkowski: The role of magnetic vortex formation in chains of spherical FeNi nanoparticles: a micromagnetics study, Jap. J. Appl. Phys. **48**, 103002 (2009)

143. R.K.K. Chong, R.E. Dunin-Borkowski, T. Kasama, M.J. Hÿtch, M.R. McCartney: Off-axis electron holography and image spectroscopy of ferromagnetic FeNi nanoparticles, Inst. Phys. Conf. Ser. **179**, 451-454 (2003)

144. M.K. Kim, P. Dhak, H.Y. Lee, J.H. Lee, M.W. Yoo, J. Lee, K. Jin, A. Chu, K.T. Nam, H.S. Park, S. Aizawa: Self-assembled magnetic nanospheres with three-dimensional magnetic vortex, Appl. Phys. Lett. **105**, 232402 (2014)

145. G.D. Price: Subsolidus phase relations in the titanomagnetite solid solution series, Am. Mineral. **66**, 751-758 (1981)

146. R.J. Harrison, R.E. Dunin-Borkowski, A. Putnis: Direct imaging of nanoscale magnetic interactions in minerals, Proc. Nat. Acad. Sci. USA, **99**, 16556-16561 (2002)

147. J.M. Feinberg, R.J. Harrison, T. Kasama, R.E. Dunin-Borkowski, G.R. Scott, P.R. Renne: Effects of internal mineral structures on the magnetic remanence of silicate-hosted titanomagnetite inclusions: An electron holography study, J. Geophys. Res. **111**, B12S15 (2006)

148. T. Kasama, N.S. Church, J.M. Feinberg, R.E. Dunin-Borkowski, R.J. Harrison: Direct observation of ferrimagnetic/ferroelastic domain interactions in magnetite below the Verwey transition, Earth Planet. Sci. Lett. **297**, 10-17 (2010)

149. T. Kasama, R.J. Harrison, N.S. Church, M. Nagao, J.M. Feinberg, R.E. Dunin-Borkowski: Ferrimagnetic/ferroelastic domain interactions in magnetite below the Verwey transition Part I: electron holography and Lorentz microscopy, Phase Transitions **86**, 67-87 (2013)

150. J.F.J. Bryson, T. Kasama, R.E. Dunin-Borkowski, R.J. Harrison: Ferrimagnetic/ferroelastic domain interactions in magnetite below the Verwey transition Part II: micromagnetic and image simulations, Phase Transitions **86**, 88-102 (2013)

151. M. Varón, M. Beleggia, T. Kasama, R.J. Harrison, R.E. Dunin-Borkowski, V.F. Puntes, C. Frandsen: Direct observation of dipolar magnetism in low-dimensional nanoparticle assemblies, Scientific Reports **3**, 1234 (2013)

152. C.A. Ross: Patterned magnetic recording media, Ann. Rev. Mater. Res. **31**, 203-235 (2001)

153. R.E. Dunin-Borkowski, S.B. Newcomb, M.R. McCartney, C.A. Ross, M. Farhoud: Off-axis electron holography of magnetic microstructure in nanomagnet arrays fabricated by interferometric lithography, Inst. Phys. Conf. Ser. **168**, 485-488 (2001)

154. T.J. Bromwich, A. Kohn, A.K. Petford-Long, T. Kasama, R.E. Dunin-Borkowski, S.B. Newcomb, C.A. Ross: Remanent magnetization states and interactions of arrays of 100 nm cobalt dots measured using TEM, J. Appl. Phys. **98**, 053909 (2005)

155. T.J. Bromwich, T. Kasama, R.K.K. Chong, R.E. Dunin-Borkowski, A.K. Petford-Long, O.G. Heinonen, C.A. Ross: Remanent magnetic states and interactions in nano-pillars, Nanotechnology **17**, 4367-4373 (2006)

156. R.E. Dunin-Borkowski, M.R. McCartney, B. Kardynal, S.S.P. Parkin, M.R. Scheinfein, D.J. Smith: Off-axis electron holography of patterned magnetic nanostructures, J. Microsc. **200**, 187-205 (2000)

157. H. Hu, H. Wang, M.R. McCartney, D.J. Smith: Study of in situ magnetization reversal processes for nanoscale Co rings using off-axis electron holography, J. Appl. Phys. **97**, 054305 (2005)

158. M. Heumann, T. Uhlig, J. Zweck: True single domain and configuration-assisted switching of submicron permalloy dots observed by electron holography, Phys. Rev. Lett. **94**, 077202 (2005)

159. D.J. Smith, R.E. Dunin-Borkowski, M.R. McCartney, B. Kardynal, M.R. Scheinfein: Interlayer coupling within individual patterned magnetic elements, J. Appl. Phys. **87**, 7400-7404 (2000)

160. F. Junginger, M. Kläui, D. Backes, U. Rüdiger, T. Kasama, R.E. Dunin-Borkowski, L.J. Heyderman, C.A.F. Vaz, J.A.C. Bland: Spin torque and heating effects in current-induced domain wall motion probed by high-resolution transmission electron microscopy, Appl. Phys. Lett. **90**, 132506 (2007)

161. M. Eltschka, M. Wötzel, J. Rhensius, S. Krzyk, U. Nowak, M. Kläui, T. Kasama, R.E. Dunin-Borkowski, L.J. Heyderman, H.J. van Driel, R.A. Duine: Nonadiabatic spin torque investigated using thermally activated magnetic domain wall dynamics, Phys. Rev. Lett. **105**, 056601 (2010)

162. A.N. Bogdanov, D.A. Yablonskii: Thermodynamically stable “vortices” in magnetically ordered crystals. The mixed state of magnets, Sov. Phys. JETP **68**, 101-103 (1989)

163. S. Mühlbauer, B. Binz, F. Jonietz, C. Pfleiderer, A. Rosch, A. Neubauer, R. Georgii, P. Böni: Skyrmion lattice in a chiral magnet, Science **323**, 915-919 (2009)

164. X.Z. Yu, Y. Onose, N. Kanazawa, J.H. Park, J.H. Han, Y. Matsui, N. Nagaosa, Y. Tokura: Real-space observation of a two-dimensional skyrmion crystal, Nature **465**, 901-904 (2010)

165. X.Z. Yu, N. Kanazawa, W.Z. Zhang, T. Nagai, T. Hara, K. Kimoto, Y. Matsui, Y. Onose, Y. Tokura: Skyrmion flow near room temperature in an ultralow current density, Nature Communications **3**, 988 (2012)

166. A. Kovács, Z.-A. Li, K. Shibata, R.E. Dunin-Borkowski: Lorentz imaging and off-axis electron holography of magnetic skyrmions in FeGe, Resolution and Discovery **1**, 2-8 (2016)

167. Z.-A. Li, F. Zheng, A.H. Tavabi, J. Caron, C. Jin, H. Du, A. Kovács, M. Tian, M. Farle, R.E. Dunin-Borkowski: Magnetic skyrmion formation at lattice defects and grain boundaries studied by quantitative off-axis electron holography, Nano Letters **17**, 1395-1401 (2017)

168. A. Kovács, J. Caron, A. Savchenko, N.S. Kiselev, K. Shibata, Z.-A. Li, N. Kanazawa, Y. Tokura, S. Blügel, R.E. Dunin-Borkowski: Mapping the magnetization fine structure of a lattice of Bloch-type skyrmions in an FeGe thin film, Appl. Phys. Lett. **111**, 192410 (2017)

169. K. Shibata, A. Kovács, N. Kanazawa, R.E. Dunin-Borkowski, Y. Tokura: Temperature and magnetic field dependence of the internal and lattice structures of skyrmions by off-axis electron holography, Phys. Rev. Lett. **118**, 087202 (2017)

170. C. Jin, Z.-A. Li, A. Kovács, J. Caron, F. Zheng, F.N. Rybakov, N.S. Kiselev, H. Du, S. Blügel, M. Tian, Y. Zhang, M. Farle, R.E. Dunin-Borkowski: Control of morphology and formation of highly geometrically confined magnetic skyrmions, Nature Communications **8**, 15569 (2017)

171. F. Zheng, H. Li, S. Wang, D. Song, C. Jin, W. Wei, A. Kovács, J. Zang, M. Tian, Y. Zhang, H. Du, R.E. Dunin-Borkowski: Direct imaging of a zero-field target skyrmion and its polarity switch in a chiral magnetic nanodisk, Phys. Rev. Lett. **119**, 197205 (2017)

172. E. Snoeck, R.E. Dunin-Borkowski, F. Dumestre, P. Renaud, C. Amiens, B. Chaudret, P. Zurcher: Quantitative magnetization measurements on nanometer ferromagnetic cobalt wires using electron holography, Appl. Phys. Lett. **82**, 88-90 (2003)

173. A. Akhtari-Zavareh, L.P. Carignan, A. Yelon, D. Ménard, T. Kasama, R. Herring, R.E. Dunin-Borkowski, M.R. McCartney, K.L. Kavanagh: Off-axis electron holography of ferromagnetic multilayer nanowires, J. Appl. Phys. **116**, 023902 (2014)

174. M.R. McCartney, R.E. Dunin-Borkowski: Electron holography of nano-scale magnetic particles and cross-sectional tunnel junctions, In: *Electron Microscopy 98*, Vol.2, ed. by H.A. Calderón Benavides, M.J. Yacamán. Paper presented at the 14th International Conference on Electron Microscopy, Cancun, Mexico (Institute of Physics Publishing, Bristol, 1998), pp. 497-498.

175. J.C. Loudon, N.D. Mathur, P.A. Midgley: Charge-ordered ferromagnetic phase in $La_{0.5}Ca_{0.5}MnO_3$, Nature **420**, 797-800 (2002)

176. Y. Murakami, J.H. Yoo, D. Shindo, T. Atou, M. Kikuchi: Magnetization distribution in the mixed-phase state of hole-doped manganites, Nature **423**, 965-968 (2003)

177. T. Kasama, M.S. Moreno, R.E. Dunin-Borkowski, S.B. Newcomb, N. Haberkorn, J. Guimpel, P.A. Midgley: Characterization of the magnetic properties of a $GdBa_2Cu_3O_7/La_{0.75}Sr_{0.25}MnO_3$ superlattice using off-axis electron holography, Appl. Surf. Sci. **252**, 3977-3983 (2006)

178. A. Masseboeuf, A. Marty, P. Bayle-Guillemaud, C. Gatel, E. Snoeck: Quantitative observation of magnetic flux distribution in new magnetic films for future high density recording media, Nano Letters **9**, 2803-2806 (2009)

179. D. Zhang, J.M. Shaw, D.J. Smith, M.R. McCartney: Domain structure and perpendicular magnetic anisotropy in CoFe/Pd multilayers using off-axis electron holography, J. Magn. Magn. Mat. **388**, 16-21 (2015)

180. M. Beleggia, T. Kasama, R.E. Dunin-Borkowski: The quantitative measurement of magnetic moments from phase images of nanoparticles and nanostructures, Ultramicroscopy **110**, 425-432 (2010)

181. J. Caron: Model-based reconstruction of magnetisation distributions in nanostructures from electron optical phase images, PhD thesis (RWTH Aachen University, Aachen 2017)

182. R.E. Dunin-Borkowski, M.R. McCartney, B. Kardynal, D.J. Smith, M.R. Scheinfein: Switching asymmetries in closely coupled magnetic nanostructure arrays, Appl. Phys. Lett. **75**, 2641-2643 (1999)

183. J.F. Bryson, N.S. Church, T. Kasama, R.J. Harrison: Nanomagnetic intergrowths in Fe-Ni meteoritic metal: The potential for time-resolved records of planetesimal dynamo fields, Earth and Planetary Science Letters **388**, 237-248 (2014)

184. E. Snoeck, C. Gatel, L.M. Lacroix, T. Blon, S. Lachaize, J. Carrey, M. Respaud, B. Chaudret: Magnetic configurations of 30 nm iron nanocubes studied by electron holography, Nano Letters **8**, 4293-4298 (2008)

185. N. Biziere, C. Gatel, R. Lassalle-Balier, M.C. Clochard, J.E. Wegrowe, E. Snoeck: Imaging the fine structure of a magnetic domain wall in a Ni nanocylinder, Nano Letters **13**, 2053-2057 (2013)

186. J.F. Einsle, C. Gatel, A. Masseboeuf, R. Cours, M.A. Bashir, M. Gubbins, R.M. Bowman, E. Snoeck: In situ electron holography of the dynamic magnetic field emanating from a hard-disk drive writer, Nano Research **8**, 1241-1249 (2015)

187. S.K. Walton, K. Zeissler, W.R. Branford, S. Felton: MALTS: A tool to simulate Lorentz Transmission Electron Microscopy from micromagnetic simulations, IEEE Trans. Magn. **49**, 4795-4800 (2013)

188. H. Lichte, K.H. Herrmann, F. Lenz: Electron noise in off-axis image plane holography, Optik **77**, 135-140 (1987)

189. T. Tanigaki, T. Akashi, A. Sugawara, K. Miura, J. Hayakawa, K. Niitsu, T. Sato, X. Yu, Y. Tomioka, K. Harada, D. Shindo: Magnetic field observations in CoFeB/Ta layers with 0.67-nm resolution by electron holography, Scientific Reports, **7**, 16598 (2017)

190. G. Matteucci, G.F. Missiroli, M. Muccini, G. Pozzi: Electron holography in the study of the electrostatic fields: the case of charged microtips, Ultramicroscopy **45**, 77-83 (1992)

191. G. Matteucci, G.F. Missiroli, G. Pozzi: Electron interferometry and holography of electrostatic fields: Fundamental and applicative aspects, Physica B 151, 223-229 (1988)

192. T. Kawasaki, G.F. Missiroli, G. Pozzi, A. Tonomura: Multiple-beam interference experiments with a holographic electron microscope, Optik **92**, 168-174 (1993)

193. T. Matsumoto, A. Tonomura: The phase constancy of electron waves traveling through Boersch's electrostatic phase plate, Ultramicroscopy **63**, 5-10 (1996)

194. J. Cumings, A. Zettl, M.R. McCartney, J.C.H. Spence: Electron holography of field-emitting carbon nanotubes, Phys. Rev. Lett. **88**, 056804 (2002)

195. J.J. Kim, D. Shindo, Y. Murakami, W. Xia, L.J. Chou, Y.L. Chueh: Direct observation of field emission in a single $TaSi_2$ nanowire, Nano Letters **7**, 2243-2247 (2007)

196. F. Houdellier, A. Masseboeuf, M. Monthioux, M.J. Hÿtch: New carbon cone nanotip for use in a highly coherent cold field emission electron microscope, Carbon **50**, 2037-2044 (2012)

197. L. de Knoop, F. Houdellier, C. Gatel, A. Masseboeuf, M. Monthioux, M.J. Hÿtch: Determining the work function of a carbon-cone cold-field emitter by in situ electron holography, Micron **63**, 2-8 (2014)

198. F. Houdellier, L. de Knoop, C. Gatel, A. Masseboeuf, S. Mamishin, Y. Taniguchi, M. Delmas, M. Monthioux, M.J. Hÿtch, E. Snoeck: Development of TEM and SEM high brightness electron guns using cold-field emission from a carbon nanotip, Ultramicroscopy **151**, 107-115 (2015)

199. M. Beleggia, T. Kasama, R.E. Dunin-Borkowski, D.J. Larson, T.F. Kelly, G. Pozzi: Towards quantitative electron holographic mapping of the electric field around the tip of a sharp biased metallic needle, J. Appl. Phys. **116**, 024305 (2014)

200. V. Migunov, A. London, M. Farle, R.E. Dunin-Borkowski: Model-independent measurement of the charge density in an Fe atom probe needle using off-axis electron holography without mean inner potential effects, J. Appl. Phys. **117**, 134301 (2015)

201. M. Beleggia, T. Kasama, R.E. Dunin-Borkowski, S. Hofmann, G. Pozzi: Direct measurement of the charge distribution along a biased carbon nanotube bundle using electron holography, Appl. Phys. Lett. **98**, 243101 (2011)

202. C. Gatel, A. Lubk, G. Pozzi, E. Snoeck, M.J. Hÿtch: Counting elementary charges on nanoparticles by electron holography, Phys. Rev. Lett. **111**, 025501 (2013)

203. M. Beleggia, L.C. Gontard, R.E. Dunin-Borkowski: Local charge measurement using off-axis electron holography, J. Phys. D: Appl. Phys. **49**, 294003 (2016)

204. J.M. Titchmarsh, A.J. Lapworth, G.R. Booker: A new method for investigating the electric field regions of p-n junctions, Phys. Stat. Sol. **34**, K83-K86 (1969)

205. S. Frabboni, G. Matteucci, G. Pozzi: Observation of electrostatic fields by electron holography: the case of reverse-biased p-n junctions, Ultramicroscopy **23**, 29-37 (1987)

206. G. Pozzi, M. Vanzi: Interpretation of electron interference images of reverse-biased p-n junctions, Optik **60**, 175-180 (1982)

207. M. Beleggia, D. Cristofori, P.G. Merli, G. Pozzi: Electron microscopy of reverse biased p-n junctions, Micron **31**, 231-236 (2000)

208. A. Pantzer, A. Vakahy, Z. Eliyahou, G. Levi, D. Horvitz, A. Kohn: Dopant mapping in thin FIB prepared silicon samples by off-axis electron holography, Ultramicroscopy **138**, 36-45 (2014)

209. W.D. Rau, P. Schwander, F.H. Baumann, W. Höppner, A. Ourmazd: Two-dimensional mapping of the electrostatic potential in transistors by electron holography, Phys. Rev. Lett. **82**, 2614-2617 (1999)

210. M.A. Gribelyuk, M.R. McCartney, J. Li, C.S. Murthy, P. Ronsheim, B. Doris, J.S. McMurray, S. Hegde, D.J. Smith: Mapping of electrostatic potential in deep submicron CMOS devices by electron holography, Phys. Rev. Lett. **89**, 025502 (2002)

211. S. Frabboni, G. Matteucci, G. Pozzi, M. Vanzi: Electron holographic observations of the electrostatic field associated with thin reverse-biased p-n junctions, Phys. Rev. Lett. **55**, 2196-2199 (1985)

212. A.C. Twitchett, R.E. Dunin-Borkowski, P.A. Midgley: Quantitative electron holography of biased semiconductor devices, Phys. Rev. Lett. **88**, 238302 (2002)

213. A.C. Twitchett, R.E. Dunin-Borkowski, R.J. Hallifax, R.F. Broom, P.A. Midgley: Off-axis electron holography of electrostatic potentials in unbiased and reverse biased focused ion beam milled semiconductor devices, J. Microsc. **214**, 287-296 (2004)

214. A.C. Twitchett, R.E. Dunin-Borkowski, R.J. Hallifax, R.F. Broom, P.A. Midgley: Off-axis electron holography of unbiased and reverse-biased focused ion beam milled Si *p-n* junctions, Microsc. Microanal. **11**, 66-78 (2005)

215. R.E. Dunin-Borkowski, A.C. Twitchett, P.A. Midgley: The determination and interpretation of electrically active charge density profiles at reverse biased p-n junctions from electron holograms, Microsc. Microanal. **8** (Suppl. 2), 42-43 (2002)

216. Z. Wang, T. Hirayama, T. Kato, K. Sasaki, H. Saka, N. Kato: Electron holographic characterization of electrostatic potential distributions in a transistor sample fabricated by focused ion beam, Appl. Phys. Lett. **80**, 246-248 (2002)

217. Z. Wang, K. Sasaki, N. Kato, K. Urata, T. Hirayama, H. Saka: Examination of electrostatic potential distribution across an implanted p–n junction by electron holography, J. Electron Microsc. **50**, 479-484 (2002)

218. Z. Wang, T. Kato, N. Shibata, T. Hirayama, N. Kato, K. Sasaki, H. Saka: Characterizing an implanted Si/Si p-n junction with lower doping level by combined electron holography and focused-ion-beam milling, Appl. Phys. Lett. **81**, 478-480 (2002)

219. Z. Wang, T. Kato, T. Hirayama, N. Kato, K. Sasaki, H. Saka: Wedge-shaped and flat cross-sections for quantitative characterization of the electrostatic potential distributions across p-n junctions by electron holography, Surf. Int. Anal. **37**, 221-224 (2005)

220. D. Cooper, A.C. Twitchett, P.K. Somodi, P.A. Midgley, R.E. Dunin-Borkowski, I. Farrer, D.A. Ritchie: Improvement in electron holographic phase images of focused-ion-beam-milled GaAs and Si *p-n* junctions by in situ annealing, Appl. Phys. Lett. **88**, 063510 (2006)

221. D. Cooper, R. Truche, A.C. Twitchett-Harrison, R.E. Dunin-Borkowski, P.A. Midgley: Quantitative off-axis electron holography of GaAs *p-n* junctions, J. Microsc. **233**, 102-113 (2009)

222. M. Beleggia, G.C. Cardinali, P.F. Fazzini, P.G. Merli, G. Pozzi: Influence of the specimen surfaces on TEM images of reverse-biased p-n junctions, Inst. Phys. Conf. Ser. **169**, 427-430 (2001)

223. R.E. Dunin-Borkowski, W.O. Saxton: The importance of the fringing field surrounding a TEM foil to the quantification of phase contrast at a p-n junction, In: Atomic Resolution Microscopy of Surfaces and Interfaces, ed. by D.J. Smith, R.J. Hamers. Materials Research Society Symposium Proceedings, Vol. 466 (Materials Research Society, Warrendale, PA 1996) pp. 73-78

224. P.K. Somodi, A.C. Twitchett-Harrison, P.A. Midgley, B.E. Kardynal, C.H.W. Barnes, R.E. Dunin-Borkowski: Finite element simulations of electrostatic dopant potentials in thin semiconductor specimens for electron holography, Ultramicroscopy **134**, 160-166 (2013)

225. M.Y. Kim, J.M. Zuo, J.C.H. Spence: Ab-initio LDA calculations of the mean Coulomb potential V_0 in slabs of crystalline Si, Ge and MgO, Phys. Status Solidi A **166**, 445-451 (1998)

226. M. Schowalter, D. Lamoen, A. Rosenauer, P. Kruse, D. Gerthsen: First-principles calculations of the mean inner Coulomb potential for sphalerite type II-VI semiconductors, Appl.Phys. Lett. **85**, 4938-4940 (2004)

227. M. Schowalter, A. Rosenauer, D. Lamoen, P. Kruse, D. Gerthsen: Ab initio computation of the mean inner Coulomb potential of wurtzite-type semiconductors and gold, Appl. Phys. Lett. **88**, 232108 (2006)

228. R.S. Pennington, C.B. Boothroyd, R.E. Dunin-Borkowski: Surface effects on mean inner potentials studied using density functional theory, Ultramicroscopy **159**, 34-45 (2015)

229. K.H. Park: Cross-sectional TEM specimen preparation of semiconductor devices by focused ion beam etching, Mater. Res. Soc. Symp. Proc. **199**, 271-280 (1990)

230. J. Szot, R. Hornsey, T. Ohnishi, J. Minagawa: Focused ion beam micromachining for transmission electron microscopy specimen preparation of semiconductor laser diodes, J. Vac. Sci, Technol. B **10**, 575-579 (1992)

231. S.M. Sze: *Physics of Semiconductor Devices* (Wiley, New York 2002)

232. S.M. Schwarz, B.W. Kempshall, L.A. Giannuzzi, M.R. McCartney: Avoiding the curtaining effect: backside milling by FIB INLO, Microsc. Microanal. **9** (Suppl. 2), 116-117 (2003)

233. M.R. McCartney, J. Li, P. Chakraborty, L.A. Giannuzzi, S.M. Schwarz: Issues affecting quantitative evaluation of dopant profiles using electron holography, Microsc. Microanal. **9** (Suppl. 2), 776-777 (2003)

234. D. Cooper, R. Truche, P. Rivallin, J.M. Hartmann, F. Laugier, F. Bertin, A. Chabli, J.L. Rouviere: Medium resolution off-axis electron holography with millivolt sensitivity, Appl. Phys. Lett. **91**, 143501 (2007)

235. D. Cooper, P. Rivallin, J.M. Hartmann, A. Chabli, R.E. Dunin-Borkowski: Extending the detection limit of dopants for focused ion beam prepared semiconductor specimens examined by off-axis electron holography, J. Appl. Phys. **106**, 064506 (2009)

236. D. Cooper, A.C. Twitchett-Harrison, P.A. Midgley, R.E. Dunin-Borkowski: The influence of electron irradiation on electron holography of focused ion beam milled GaAs *p-n* junctions, J. Appl. Phys. **101**, 094508 (2007)

237. D. Cooper, C. Ailliot, J.P. Barnes, J.M. Hartmann, P. Salles, G. Benassayag, R.E. Dunin-Borkowski: Dopant profiling of focused ion beam milled semiconductors using off-axis electron holography; reducing artefacts, extending detection limits and reducing the effects of gallium implantation, Ultramicroscopy **110**, 383-389 (2010)

238. J.B. Park, T. Niermann, D. Berger, A. Knauer, I. Koslow, M. Weyers, M. Kneissl, M. Lehmann: Impact of electron irradiation on electron holographic potentiometry, Appl. Phys. Lett. **105**, 094102 (2014)

239. A. Lenk, H. Lichte, U. Muehle: 2D-mapping of dopant distribution in deep sub micron CMOS devices by electron holography using adapted FIB-preparation, J. Electron Microsc. **54**, 351-359 (2005)

240. P. Formanek, E. Bugiel: On specimen tilt for electron holography of semiconductor devices, Ultramicroscopy **106**, 292-300 (2006)

241. D. Cooper, F. de La Peña, A. Béché, J.L. Rouvière, G. Servanton, R. Pantel, P. Morin: Field mapping with nanometer-scale resolution for the next generation of electronic devices, Nano Letters **11**, 4585-4590 (2011)

242. D. Cooper, P. Rivallin, G. Guegan, C. Plantier, E. Robin, F. Guyot, I. Constant: Field mapping of focused ion beam prepared semiconductor devices by off-axis and dark field electron holography, Sem. Sci. Technol. **28**, 125013 (2013)

243. D. Cooper, R.E. Dunin-Borkowski: Interpretation of phase images of delta-doped layers, Microscopy **62 (Suppl. 1)**, S87-S98 (2013)

244. S. Yazdi, T. Kasama, M. Beleggia, M. Samaie Yekta, D.W. McComb, A.C. Twitchett-Harrison, R.E. Dunin-Borkowski: Towards quantitative electrostatic potential mapping of

working semiconductor devices using off-axis electron holography, Ultramicroscopy **152**, 10-20 (2015)

245. A.C. Twitchett, T.J.V. Yates, S.B. Newcomb, R.E. Dunin-Borkowski, P.A. Midgley: High-resolution three-dimensional mapping of semiconductor dopant potentials, Nano Letters **7**, 2020-2023 (2007)

246. A.C. Twitchett-Harrison, T.J.V. Yates, R.E. Dunin-Borkowski, P.A. Midgley: Quantitative electron holographic tomography for the 3D characterisation of semiconductor device structures, Ultramicroscopy **108**, 1401-1407 (2008)

247. D. Wolf, A. Lubk, A. Lenk, S. Sturm, H. Lichte: Tomographic investigation of fermi level pinning at focused ion beam milled semiconductor surfaces, Appl. Phys. Lett. **103**, 264104 (2013)

248. M.R. McCartney, F.A. Ponce, J. Cai, D.P. Bour: Mapping electrostatic potential across an AlGaN/InGaN/AlGaN diode by electron holography, Appl. Phys. Lett. **76**, 3055-3057 (2000)

249. M. Stevens, A. Bell, M.R. McCartney, F.A. Ponce, H. Marui, S. Tanaka: Effect of layer thickness on the electrostatic potential in InGaN quantum wells, Appl. Phys. Lett. **85**, 4651-4653 (2004)

250. L. Zhou, M. Gonschorek, E. Giraud, E. Feltin, J.F. Carlin, N. Grandjean, D.J. Smith, M.R. McCartney: Measurement of polarization-induced electric fields in GaN/AlInN quantum wells, Appl. Phys. Lett. **101**, 251902 (2012)

251. L. Zhou, D.J. Smith, M.R. McCartney, T. Xu, T.D. Moustakas: Measurement of electric field across individual wurtzite GaN quantum dots using electron holography, Appl. Phys. Lett. **99**, 101905 (2011)

252. L. Li, D.J. Smith, E. Dailey, P. Madras, J. Drucker, M.R. McCartney: Observation of hole accumulation in Ge/Si core/shell nanowires using off-axis electron holography, Nano Letters **11**, 493-497 (2011)

253. D. Cherns, C.G. Jiao: Electron holography studies of the charge on dislocations in GaN, Phys. Rev. Lett. **87**, 205504 (2001)

254. S. Chung, R.A. Berechman, M.R. McCartney, M. Skowronski: Electronic structure analysis of threading screw dislocations in 4H-SiC using electron holography, J. Appl. Phys. **109**, 034906 (2011)

255. J. Dietrich, D. Abou-Ras, S.S. Schmidt, T. Rissom, T. Unold, O. Cojocaru-Mirédin, T. Niermann, M. Lehmann, C. Boit: Origins of electrostatic potential wells at dislocations in polycrystalline Cu(In,Ga)Se_2 thin films, J. Appl. Phys. **115**, 103507 (2014)

256. L. Li, L. Jin, J. Wang, D.J. Smith, W.J. Yin, Y. Yan, H. Sang, W.C.H. Choy, M.R. McCartney: Polarization-induced charge distribution at homogeneous zincblende/wurtzite heterostructural junctions in ZnSe nanobelts, Adv. Mat. **24**, 1328-1332 (2012)

257. A. Marchewka, D. Cooper, C. Lenser, S. Menzel, H. Du, R. Dittmann, R.E. Dunin-Borkowski, R. Waser: Determination of the electrostatic potential distribution in Pt/Fe: $SrTiO_3$/Nb:$SrTiO_3$ thin-film structures by electron holography, Scientific Reports **4**, 6975 (2014)

258. M. Duchamp, V. Migunov, A.H. Tavabi, A. Mehonic, M. Buckwell, M. Munde, A.J. Kenyon, R.E. Dunin-Borkowski: In situ transmission electron microscopy of resistive switching in thin silicon oxide layers, Resolution and Discovery **1**, 27-33 (2016)

259. S. Yazdi, A. Berg, M.T. Borgström, T. Kasama, M. Beleggia, L. Samuelson, J.B. Wagner: Doping GaP core-shell nanowire pn-junctions: A study by off-axis electron holography, Small **11**, 2687-2695 (2015)

260. M.H.T. Dastjerdi, E.M. Fiordaliso, E.D. Leshchenko, A. Akhtari-Zavareh, T. Kasama, M. Aagesen, V.G. Dubrovskii, R.R. LaPierre: Three-fold symmetric doping mechanism in GaAs nanowires, Nano Letters **17**, 5875-5882 (2017)

261. Z. Gan, M. Gu, J. Tang, C.Y. Wang, Y. He, K.L. Wang, C. Wang, D.J. Smith, M.R. McCartney: Direct mapping of charge distribution during lithiation of Ge nanowires using off-axis electron holography, Nano Letters **16**, 3748-3753 (2016)

262. D. Keller, S. Buecheler, P. Reinhard, F. Pianezzi, E. Snoeck, C. Gatel, M.D. Rossell, R. Erni, A.N. Tiwari: Assessment of off-axis and in-line electron holography for measurement of potential variations in Cu(In,Ga)Se_2 thin-film solar cells, Advanced Structural and Chemical Imaging **2**, 1 (2017)

263. J. Frenkel: *Kinetic Theory of Liquids* (Oxford University Press, Oxford 1946).

264. V. Ravikumar, R.P. Rodrigues, V.P. Dravid: Direct imaging of spatially varying potential and charge across internal interfaces in solids, Phys. Rev. Lett. **75**, 4063-4066 (1995)

265. G. Pozzi: The influence of the external field on transmission electron microscopy observations of electric fields at interfaces, J. Phys. D: Appl. Phys. **29**, 1807-1811 (1996)

266. R.E. Dunin-Borkowski, W.O. Saxton: The electrostatic contribution to the forward scattering potential at a space charge layer in high energy electron diffraction. II. Fringing fields, Acta Crystallogr. A **53**, 242-250 (1997)

267. M. Elfwing, E. Olsson: Electron holography study of active interfaces in zinc oxide varistor materials, J. Appl. Phys. **92**, 5272-5280 (2002)

268. Z. Mao, R.E. Dunin-Borkowski, C.B. Boothroyd, K.M. Knowles: Direct measurement and interpretation of electrostatic potentials at 24° [001] tilt boundaries in undoped and niobium-doped strontium titanate bicrystals, J. Am. Ceram. Soc. **81**, 2917-2926 (1998)

269. R.E. Dunin-Borkowski, W.M. Stobbs, D.D. Perovic, Z.R. Wasilewski: The interpretation of the measured mean forward scattering potential of delta-doped layers in semiconductors, In: Proceedings of the 13th International Conference on Electron Microscopy, Paris, France, ed. by B. Jouffrey, C. Colliex (1994) pp. 411-412

270. P.F. Fazzini, G. Pozzi, M. Beleggia: Electron optical phase-shifts by Fourier methods: Analytical versus numerical calculations, Ultramicroscopy **104**, 193-205 (2005)

271. S. von Alfthan, N.A. Benedek, L. Chen, A. Chua, D.J.H. Cockayne, K.J. Dudeck, C. Elsässer, M.W. Finnis, C.T. Koch, B. Rahmati, M. Rühle, S.-J. Shih, A.P. Sutton: The structure of grain boundaries in strontium titanate: theory, simulation, and electron microscopy, Ann. Rev. Mat. Res. **40**, 557-599 (2010)

272. H. Lichte: Are ferroelectric crystals blaze-gratings for electrons?, Crystal Research and Technology **35**, 887-898 (2000)

273. H. Lichte, M. Reibold, K. Brand, M. Lehmann: Ferroelectric electron holography, Ultramicroscopy **93**, 199-212 (2003)

274. T. Matsumoto, M. Koguchi, K. Suzuki, H. Nishimura, Y. Motoyoshi, N. Wada: Ferroelectric 90° domain structure in a thin film of $BaTiO_3$ fine ceramics observed by 300 kV electron holography, Appl. Phys. Lett. **92**, 072902 (2008)

275. D. Szwarcman, A. Lubk, M. Linck, K. Vogel, Y. Lereah, H. Lichte, G. Markovich: Ferroelectric effects in individual $BaTiO_3$ nanocrystals investigated by electron holography, Phys. Rev. B **85**, 134112 (2012)

276. C. Phatak, A.K. Petford-Long, M. Beleggia, M. De Graef: Theoretical study of ferroelectric nanoparticles using phase reconstructed electron microscopy, Phys. Rev. B **89**, 214112 (2014)

277. H. Lichte: Optimum focus for taking electron holograms, Ultramicroscopy **38**, 13-22 (1991)

278. H. Lichte: Electron holography: I. Can electron holography reach 0.1 nm resolution?, Ultramicroscopy **47**, 223-230 (1992)

279. H. Lichte, W.D. Rau: High-resolution electron holography with the CM30FEG-special Tübingen, Ultramicroscopy **54**, 310-316 (1994)

280. K. Ishizuka, T. Tanji, A. Tonomura, T. Ohno, Y. Murayama: Aberration correction using off-axis holography II. Beyond the Scherzer limit, Ultramicroscopy **55**, 197-207 (1994)

281. A. Orchowski, W.D. Rau, H. Lichte: Electron holography surmounts resolution limit of electron microscopy, Phys. Rev. Lett. **74**, 399-402 (1995)

282. M. Lehmann, H. Lichte, D. Geiger, G. Lang, E. Schweda: Electron holography at atomic dimensions - Present state, Mater. Characterization **42**, 249-263 (1999)

283. M. Lehmann, H. Lichte: Electron holographic material analysis at atomic dimensions, Cryst. Res. Technol. **40**, 149-160 (2005)

284. H. Lichte, P. Formanek, A. Lenk, M. Linck, C. Matzeck, M. Lehmann, P. Simon: Electron holography: Applications to materials questions, Annu. Rev. Mater. Res. **37**, 539-588 (2007)

285. M. Linck, B. Freitag, S. Kujawa, M. Lehmann, T. Niermann: State of the art in atomic resolution off-axis electron holography, Ultramicroscopy **116**, 13-23 (2012)

286. M. Linck: Optimum aberration coefficients for recording high-resolution off-axis holograms in a C_S-corrected TEM, Ultramicroscopy **124**, 77-87 (2013)

287. S. Borghardt, F. Winkler, Z. Zanolli, M.J. Verstraete, J. Barthel, A.H. Tavabi, R.E. Dunin-Borkowski, B.E. Kardynal: Quantitative agreement between electron-optical phase images of WSe_2 and simulations based on electrostatic potentials that include bonding effects, Phys. Rev. Lett. **118**, 086101 (2017)

288. F. Winkler, A.H. Tavabi, J. Barthel, M. Duchamp, E. Yucelen, S. Borghardt, B.E. Kardynal, R.E. Dunin-Borkowski: Quantitative measurement of mean inner potential and specimen thickness from high-resolution off-axis electron holograms of ultra-thin layered WSe_2, Ultramicroscopy **178**, 38-47 (2017)

289. J.M. Cowley: Twenty forms of electron holography, Ultramicroscopy **41**, 335-348 (1992)

290. R.A. Herring, G. Pozzi, T. Tanji, A. Tonomura: Interferometry using convergent electron diffracted beams plus an electron biprism (CBED+ EBI), Ultramicroscopy **60**, 153-169 (1995)

291. H. Banzhof, K.-H. Herrmann: Reflection electron holography, Ultramicroscopy **48**, 475-481 (1993)

292. M.J. Hÿtch, F. Houdellier, F. Hüe, E. Snoeck: Nanoscale holographic interferometry for strain measurements in electronic devices, Nature **453**, 1086-1089 (2008)

293. A. Béché, J.L. Rouvière, J.P. Barnes, D. Cooper: Strain measurement at the nanoscale: Comparison between convergent beam electron diffraction, nano-beam electron diffraction, high resolution imaging and dark field electron holography, Ultramicroscopy **131**, 10-23 (2013)

294. T. Denneulin, F. Houdellier, M.J. Hÿtch: Differential phase-contrast dark-field electron holography for strain mapping, Ultramicroscopy **160**, 98-109 (2016)

295. T. Denneulin, M.J. Hÿtch: Four-wave dark-field electron holography for imaging strain fields, J. Phys. D: Applied Physics **49**, 244003 (2016)

296. H. Rose: Nonstandard imaging methods in electron microscopy, Ultramicroscopy **2**, 251-267 (1977)

297. M. Mankos, M.R. Scheinfein, J.M. Cowley: Absolute magnetometry at nanometer transverse spatial resolution: Holography of thin cobalt films in a scanning transmission electron microscope, J. Appl. Phys. **75**, 7418-7424 (1994)

298. M.R. McCartney, P. Kruit, A.H. Buist, M.R. Scheinfein: Differential phase contrast in TEM, Ultramicroscopy **65**, 179-186 (1996)

299. G. Pozzi: Amplitude division off-axis Fresnel holography in transmission electron microscopy, Optik **66**, 91-100 (1983)

300. G. Matteucci, G.F. Missiroli, G. Pozzi: A new off-axis Fresnel holographic method in transmission electron microscopy: an application on the mapping of ferromagnetic domains. III, Ultramicroscopy **8**, 403-408 (1982)

301. Q. Ru: Incoherent electron holography, J. Appl. Phys. **77**, 1421-1426 (1995)

302. Q. Ru, J. Endo, T. Tanji, A. Tonomura: Phase-shifting electron holography by beam tilting, Appl. Phys. Lett. **59**, 2372-2374 (1992)

303. T. Kawasaki, J. Endo, T. Matsuda, N. Osakabe, A. Tonomura: Applications of holographic interference electron microscopy to the observation of biological specimens, J. Electron Microsc. **35**, 211-214 (1986)

304. K. Yamamoto, I. Kawajiri, T. Tanji, M. Hibino, T. Hirayama: High precision phase-shifting electron holography, J. Electron Microsc. **49**, 31-39 (2000)

305. T. Suzuki, S. Aizawa, T. Tanigaki, K. Ota, T. Matsuda, A. Tonomura: Improvement of the accuracy of phase observation by modification of phase-shifting electron holography, Ultramicroscopy **118**, 21-25 (2012)

306. H. Sasaki, S. Otomo, R. Minato, K. Yamamoto, T. Hirayama: Direct observation of dopant distribution in GaAs compound semiconductors using phase-shifting electron holography and Lorentz microscopy, Microscopy **63**, 235-242 (2014)

307. D. Lei, K. Mitsuishi, K. Harada, M. Shimojo, D. Ju, M. Takeguchi: Super-resolution phase reconstruction technique in electron holography with a stage-scanning system, Jap. J. Appl. Phys. **53**, 02BC23 (2014)

308. J. Chen, T. Hirayama, T. Tanji, K. Ishizuka, A. Tonomura: Video-rate electron-holographic interference microscopy and its application to dynamic observation of electromagnetic fields, Opt. Commun. **110**, 33-40 (1994)

309. T. Hirayama, T. Tanji, A. Tonomura: Direct visualization of electromagnetic microfields by interference of three electron waves, Appl. Phys. Lett. **67**, 1185-1187 (1995)

310. T. Hirayama, G. Lai, T. Tanji, N. Tanaka, A. Tonomura: Interference of three electron waves by two biprisms and its application to direct visualization of electromagnetic fields in small regions, J. Appl. Phys. **82**, 522-527 (1997)

311. E. Völkl: Live electron holography: Window to the phase world, Microsc. Microanal., **6**, 211-217 (2000)

312. T. Latychevskaia, H.W. Fink: Solution to the twin image problem in holography, Phys. Rev. Lett., **98**, 233901 (2007)

313. B.J. Thomson, G.B. Parrent, J.H. Ward, B. Justh: A readout technique for the laser fog disdrometer, J. Appl. Meteorology **5**, 343-348 (1966)

314. A. Tonomura, A. Fukuhara, H. Watanabe, T. Komoda: Optical reconstruction of image from Fraunhofer electron-hologram, Jap. J. Appl. Phys. **7**, 295 (1968)

315. T. Matsumoto, T. Tanji, A. Tonomura: Phase-contrast visualization of an undecagold cluster by in-line electron holography, Ultramicroscopy **54**, 317-334 (1994)

316. R.E. Dunin-Borkowski: The development of Fresnel contrast analysis, and the interpretation of mean inner potential profiles at interfaces, Ultramicroscopy **83**, 193-216 (2000)

317. T. Latychevskaia, P. Formanek, C.T. Koch, A. Lubk: Off-axis and inline electron holography: Experimental comparison, Ultramicroscopy **110**, 472-482 (2010)

318. V.J. Keast, M.J. Gladys, T.C. Petersen, C. Dwyer, C.T. Koch, T. Haber, G. Kothleitner: Energy-filtered phase retrieval using the transport of intensity equation, Appl. Phys. Lett. **99**, 221905 (2011)

319. C. Ozsoy-Keskinbora, C.B. Boothroyd, R.E. Dunin-Borkowski, P.A. van Aken, C.T. Koch: Hybridization approach to in-line and off-axis (electron) holography for superior resolution and phase sensitivity, Scientific Reports **4**, 7020 (2014)

320. C. Ozsoy-Keskinbora, C.B. Boothroyd, R.E. Dunin-Borkowski, P.A. van Aken, C.T. Koch: Mapping the electrostatic potential of Au nanoparticles using hybrid electron holography, Ultramicroscopy **165**, 8-14 (2016)

321. J.M. Cowley: High resolution side-band holography with a STEM instrument, Ultramicroscopy **34**, 293-297 (1990)

322. M. Mankos, J.M. Cowley, M.R. Scheinfein: Absolute magnetometry using electron holography: Magnetic superlattices and small particles, Mat. Res. Soc. Bull. **20**, 45-48 (1995)

323. J.M. Cowley, M. Mankos, M.R. Scheinfein: Greatly defocused, point-projection, off-axis electron holography, Ultramicroscopy **63**, 133-147 (1996)

324. G. Matteucci, M. Muccini: On electron holographic mapping of electric and magnetic fields: recording and processing problems and field information reliability, Ultramicroscopy **53**, 19-25 (1994)

325. C. Gatel, F. Houdellier, E. Snoeck: Dynamical holographic Moirés in a TEM, J. Phys. D: Appl. Phys.**49**, 324001-FINAL (2016)

326. V. Migunov, C. Dwyer, C.B. Boothroyd, G. Pozzi, R.E. Dunin-Borkowski: Prospects for quantitative and time-resolved double and continuous exposure off-axis electron holography, Ultramicroscopy **178**, 48-61 (2017)

327. T. Hirayama: Interference of three electron waves and its application to direct visualization of electric fields, Mater. Characterization **42**, 193-200 (1999)

328. K. Ogai, Y. Kimura, R. Shimizu, J. Fujita, S. Matsui: Nanofabrication of grating and dot patterns by electron holographic lithography, Appl. Phys. Lett. **66**, 1560-1562 (1995)

329. C. Dwyer, C.B. Boothroyd, S.L.Y. Chang, R.E. Dunin-Borkowski: Three-wave electron vortex lattices for nanofield measurements, Ultramicroscopy **148**, 25-30 (2015)

330. T. Tanji, Q. Ru, A. Tonomura: Differential microscopy by conventional electron off-axis holography, Appl. Phys. Lett. **69**, 2623-2625 (1996)

331. T. Tanji, S. Manabe, K. Yamamoto, T. Hirayama: Electron differential microscopy using an electron trapezoidal prism, Ultramicroscopy **75**, 197-202 (1999)

332. F. Venturi, M. Campanini, G.C. Gazzadi, R. Balboni, S. Frabboni, R.W. Boyd, R.E. Dunin-Borkowski, E. Karimi, V. Grillo: Phase retrieval of an electron vortex beam using diffraction holography, Appl. Phys. Lett. **111**, 223101 (2017)

333. A. Lubk, F. Röder: Phase-space foundations of electron holography, Phys. Rev. A **92**, 033844 (2015)

334. S.J. Lade, D. Paganin, M.J. Morgan: Electron tomography of electromagnetic fields, potentials and sources, Optics Commun. **253**, 392-400 (2005)

335. C. Phatak, M. Beleggia, M. De Graef: Vector field electron tomography of magnetic materials: Theoretical development, Ultramicroscopy **108**, 503-513 (2008)

336. P.Y. Rotha, M.J. Morgan, D.M. Paganin: Lorentz-electron vector tomography using two and three orthogonal tilt series, Phys. Rev. A **83**, 023813 (2011)

337. Z.D.C. Kemp, T.C. Petersen, D.M. Paganin, K.M. Spiers, M. Weyland, M.J. Morgan: Analysis of noise-induced errors in vector-field electron tomography, Phys. Rev. A **90**, 023859 (2014)

Figure Captions

Figure 1 (a) Schematic illustration of the set-up used for generating off-axis electron holograms. The specimen occupies approximately half the field of view. Essential components are the field-emission gun (FEG) electron source, which provides coherent illumination, and the electron biprism, which causes overlap of the object and (vacuum) reference waves. The Lorentz lens allows imaging of magnetic materials in close-to-field-free conditions. (b) Off-axis electron hologram of a chain of magnetite (Fe_3O_4) crystals, recorded at 200 kV using a Philips CM200 FEGTEM. The crystals are supported on a holey carbon film. Phase changes can be seen in the form of bending of the holographic interference fringes as they pass through the crystals. Fresnel fringes from the edges of the biprism wire are also visible.

Figure 2 (a) Off-axis electron hologram recorded from a thin crystal. (b) Enlargement showing interference fringes within the specimen. (c) Fourier transform of the electron hologram. (d) Phase image obtained after inverse Fourier transformation of the sideband marked with a box in (c). Reprinted from Dunin-Borkowski et al. [156].

Figure 3 Illustration of distortion correction procedure. (a) Initial (six times amplified) phase image of a wedge-shaped InP crystal recorded at 100 kV using a Philips 400ST FEGTEM equipped with a Gatan 679 slow-scan CCD camera. (b) Phase image obtained from vacuum, with the specimen removed from the field of view. (c) Corrected phase image, obtained by subtracting image (b) from image (a). This procedure is carried out by dividing the complex image waves obtained by inverse Fourier transforming the sideband obtained from each hologram, and by calculating the phase of the resulting wavefunction. Reprinted from Smith et al. [25].

Figure 4 (a) Phase profile plotted as a function of distance into a 90° GaAs cleaved wedge specimen tilted to a weakly diffracting orientation. The phase change increases approximately linearly with specimen thickness. (b) Phase profile obtained from a GaAs wedge tilted close to a [100] zone axis, showing strong dynamical effects. Reprinted from Gajdardziska-Josifovska and Carim [58].

Figure 5 (a) Room temperature Lorentz (Fresnel underfocus) image of a $Nd_2Fe_{14}B$ hard magnet, recorded at 200 kV using a Philips CM200 FEGTEM operated in Lorentz mode. (b) Phase image of the same region of the specimen reconstructed from an electron hologram obtained using an interference fringe spacing of 2.5 nm. (c) and (d) Gradients of the phase image shown in (b), calculated parallel to the +x and -y directions, respectively. (e) Induction map derived from the phase gradients shown in (c) and (d). (f) Enlargement of the area indicated in (e). (g) Linescan obtained across a 90° domain wall that appears as a bright ridge near the center of image (b). The line profile provides an upper limit for the domain wall width of 10 nm. Reprinted from McCartney and Zhu [115].

Figure 6 (a) Off-axis electron hologram of a chain of Co particles suspended over a hole in a carbon support film, acquired at 200 kV using a Philips CM200 FEGTEM and a biprism voltage of 90 V. (b) Corresponding unwrapped phase image. (c) and (d) Experimental line profiles formed from lines 1 and 2 in (b), and fitted phase profiles generated for spherical Co nanoparticles. Reprinted from de Graef et al. [117].

Figure 7 Schematic diagram illustrating the use of specimen tilt to provide an in-plane component of the external field for in situ magnetization reversal experiments. Reprinted from Dunin-Borkowski et al. [156].

Figure 8 Phase contours showing (a) the mean inner potential (MIP) and (b) the magnetic (MAG) contribution to the phase shift at the end of a chain of magnetite crystals from magnetotactic bacteria collected from a brackish lagoon at Itaipu in Brazil. The contours have been overlaid onto the mean inner potential contribution to the phase. (c) Line profiles obtained from images (a) and (b) across the large and small magnetite crystals close to the center of each image. The experimental data are shown as open circles. The purple line shows the best-fitting simulation to the data for the larger crystal, corresponding to a distorted hexagonal cross-section (shown above the figure). The red line shows the worse fit that results from assuming a diamond shape in cross-section (also shown above the figure).

Figure 9 (a) Low magnification bright-field image of self-assembled Co nanoparticle rings and chains deposited onto an amorphous carbon support film. Each Co particle has a diameter of between 20 and 30 nm. (b - e) Magnetic phase contours (128 × amplification; 0.049 radian spacing), formed from the magnetic contribution to the measured phase shift, in four different nanoparticle rings. The outlines of the nanoparticles are marked in white, while the direction of the measured magnetic induction is indicated both using arrows and according to the color wheel shown in (f) (red = right, yellow = down, green = left, blue = up). Reprinted from Dunin-Borkowski et al. [12].

Figure 10 (a) Chemical map of $Fe_{0.56}Ni_{0.44}$ nanoparticles, obtained using three-window background-subtracted elemental mapping with a Gatan imaging filter, showing Fe (red), Ni (blue) and O (green). (b) Bright-field image and (c) electron hologram of

the end of a chain of $Fe_{0.56}Ni_{0.44}$ particles. The hologram was recorded using an interference fringe spacing of 2.6 nm. Reprinted from Dunin-Borkowski et al. [12].

Figure 11 (a) and (b) Experimental phase contours showing the strength of the local magnetic induction (integrated in the electron beam direction) in two different chains of $Fe_{0.56}Ni_{0.44}$ particles, recorded with the electron microscope objective lens switched off. The particle diameters are: (a) 75 nm between two smaller particles; (b) 71 nm at the end of a chain. Contours, whose spacings are 0.083 and 0.2 radians for images (a) and (b), respectively, have been overlaid onto oxygen maps of the particles recorded using a Gatan imaging filter. The mean inner potential contribution to the measured phase shift has been removed from each image. (c) and (d) show schematic representations of the magnetic microstructure in the chains. Magnetic vortices spinning about the chain axis are visible in (c) and (d). A vortex spinning perpendicular to the chain axis is also visible in (d). Reprinted from Dunin-Borkowski et al. [12].

Figure 12 Three-window background-subtracted elemental maps acquired from a naturally occurring titanomagnetite sample with a Gatan imaging filter using (a) the Fe L edge and (b) the Ti L edge. Brighter contrast indicates a higher concentration of Fe and Ti in (a) and (b), respectively. Reprinted from Dunin-Borkowski et al. [12].

Figure 13 Magnetic phase contours from the region shown in Fig. 12, measured using electron holography. Each image was acquired with the specimen in magnetic-field-free conditions. The outlines of the magnetite-rich regions are marked in white, while the direction of the measured magnetic induction is indicated both using arrows and according to the color wheel shown at the bottom of the figure (red = right, yellow = down, green = left, blue = up). Images (a), (c), (e) and (g) were obtained after

applying a large (>10,000 Oe) field towards the top left, then the indicated field towards the bottom right, after which the external magnetic field was removed for hologram acquisition. Images (b), (d), (f) and (h) were obtained after applying identical fields in the opposite directions. Reprinted from Harrison et al. [146].

Figure 14 (a) Chemical map of a finely-exsolved naturally-occurring titanomagnetite inclusion within pyroxene, acquired using a Gatan imaging filter. The blue regions show the positions of magnetite (Fe_3O_4) blocks, which are separated from each other by paramagnetic ulvöspinel (Fe_2TiO_4) lamellae. (b) and (c) show magnetic phase contours, measured using electron holography from the same region after magnetizing the sample using two different values of the magnetic field provided by the conventional microscope objective lens. The in-plane component of the applied field was always vertical on the page. The black contour lines show the direction and magnitude of the projected in-plane magnetic induction, which can be correlated with the positions of the magnetite blocks (outlined in white). The direction of the measured induction is also indicated using colors and arrows. Each image was acquired with the specimen in magnetic-field-free conditions. The outlines of the magnetite-rich regions are marked in white, while the direction of the measured magnetic induction is indicated using arrows and colors. Reprinted from Feinberg et al. [147].

Figure 15 (a) Scanning electron microscope image of 100-nm-diameter 20-nm-thick Co dots fabricated on Si in a square array of side 200 nm using interferometric lithography. (b) Off-axis electron hologram of part of an electron-transparent membrane containing the dots, prepared using FIB milling. The hologram was acquired at 200 kV using a Philips CM200 FEGTEM, a biprism voltage of 160 V, a holographic interference fringe spacing of 3.05 nm and an overlap width of 1.04 μm. (c) and (d) show magnetic contributions to the measured electron holographic phase shift

for two remanent magnetic states. The contour spacing is 0.033 radians. (c) was formed by saturating the dots upwards and then removing the external field. (d) was formed by saturating the dots upwards, applying a 382 Oe downward field and then removing the external field. Reprinted from Dunin-Borkowski et al. [153].

Figure 16 Temperature and magnetic field dependence of skyrmions in B20-type FeGe. (a-c) Magnetic induction maps of a skyrmion lattice recorded in a 100 mT out-of-plane magnetic field at 95, 200 and 240 K, respectively. The magnetic induction maps were generated from magnetic phase images obtained using off-axis electron holography. (d) Phase shifts across skyrmions measured from magnetic phase images, plotted as a function of temperature. (e-h) Magnetic induction maps of a skyrmion lattice recorded at 200 K in out-of-plane magnetic fields of 100, 300, 350 and 400 mT, respectively. The contour spacing in each magnetic induction map is $2\pi/64 = 0.098$ radians and the scale bar is 100 nm. A color wheel is shown alongside (c). Adapted from Kovács et al. [166].

Figure 17 (a) Bright-field image of the end of a bundle of Co nanowires adjacent to a hole in a carbon support film. (b) Contours (0.005 radian spacing) generated from the magnetic contribution to the phase shift for a single isolated Co nanowire, superimposed onto the mean inner potential contribution to the measured phase shift. Reprinted from Snoeck et al. [172].

Figure 18 (a) Montage of three electron holograms acquired from the end of a bundle of Co nanowires. The biprism voltage is 210 V, the acquisition time for each hologram 16 s, the holographic interference fringe spacing 3.9 nm and the holographic overlap width 1160 nm. No objective aperture was used. (b) Magnetic remanent state, displayed in the form of contours (0.25 radian spacing), generated from the measured magnetic

contribution to the electron holographic phase shift after saturating the wires in the direction of the axis of the bundle. The contours are superimposed onto the mean inner potential contribution to the phase shift. Reprinted from Snoeck et al. [172].

Figure 19 (a) Off-axis electron hologram obtained from a magnetic tunnel junction containing a 4-nm HfO_2 tunnel barrier. (b) Measured phase profile across the layers in the tunnel junction structure. (c) Image formed by recording two holograms with opposite directions of magnetization in the specimen, and subsequently taking the difference between the recorded phase gradients (calculated in a direction perpendicular to the layers) and dividing by the average of the two phases. (d) Measured magnetic induction in the tunnel junction sample, generated by multiplying a line profile obtained from image (c) by a constant (see text for details), with the vertical scale now plotted in units of Tesla. Reprinted from McCartney and Dunin-Borkowski [174].

Figure 20 (a) Schematic diagram of the experimental set-up used to record electron holograms of field-emitting carbon nanotubes. (b) Phase shift and phase gradient maps determined from electron holograms of a single multi-walled carbon nanotube at bias voltages of 0 and 120 V. The phase gradient indicates where the electric field is strongest. Note the concentration of the electric field at the nanotube tip when the bias voltage is 120 V. Reprinted from Cumings et al. [194].

Figure 21 (a)-(c) Equiphase contours recorded using off-axis electron holography from an electrically biased Fe needle that contains yttrium oxide nanoparticle inclusions. A voltage was applied between the needle and a counter-electrode that was placed coaxially with the needle at distance of ~400 nm from it. The images correspond to (a) an original phase image recorded from the needle; (b) the difference between

phase images acquired at two different bias voltages; (c) a best-fitting model-dependent simulation to the result shown in (b). (d) shows a central slice of the three-dimensional distribution of electrical potential (colours) and electric field (white lines) around the needle, inferred from the results shown in (a)-(c) on the assumption of cylindrical symmetry. Reprinted from Migunov et al. [200].

Figure 22 (a) Reconstructed maps of the electrostatic potential distribution in a 0.35 μm semiconductor device structure, with a contour step of 0.1 V, recorded at an accelerating voltage of 200 KV using a Philips CM200 FEGTEM. (b) Lateral and (c) depth profiles obtained from the image shown in (a). Predictions from process simulations for 'scaled loss' and 'empirical loss' models are also shown. (d) Two-dimensional simulated map of the potential based on the 'empirical loss' model, with a contour step of 0.1 V. The dimensions are in μm. Reprinted from Gribelyuk et al. [210].

Figure 23 (a) Schematic diagram showing the specimen geometry used for applying external voltages to FIB-milled semiconductor device specimens containing *p-n* junctions in situ in the TEM. In the diagram, FIB milling has been used to machine a membrane of uniform thickness that contains a *p-n* junction at one corner of a 90° cleaved wedge. (b) Schematic diagram showing the specimen position in a single tilt electrical biasing holder. The specimen is glued to the edge of a Cu grid using conducting epoxy and then clamped between two spring contacts on an insulating base. (c) Reconstructed phase image acquired from an unbiased Si sample containing a *p-n* junction. Note the 'gray' layer running along the edge of the specimen, which is discussed in the text. No attempt has been made to remove the 2π phase 'wraps' at the edge of the specimen. (d) Phase shift measured across a *p-n* junction as a function of reverse bias for a single sample of 390 nm crystalline

thickness (measured using convergent beam electron diffraction). (e) shows the height of the measured step in phase across the junction as a function of reverse bias. (f) Four-times-amplified reconstructed phase image, showing the vacuum region outside a *p-n* junction in a 2-V-reverse-biased cleaved wedge sample that had not been FIB-milled. Reprinted from Twitchett et al. [212].

Figure 24 Simulations of electrostatic potential distributions in parallel-sided slabs of thickness 300 nm containing abrupt, symmetrical Si *p-n* junctions formed from (a) 10^{18} , (b)10^{17} and (c) 10^{16} cm^{-3} of Sb (*n*-type) and B (*p*-type) dopants. The potential at the specimen surfaces is 0.7 eV above the Fermi level, and contours of spacing 0.05 V are shown. The horizontal scale is different in each figure in order to show the variation in potential close to the position of the junction. The simulations were generated using a 2-dimensional rectangular grid. Reprinted from Somodi et al. [224].

Figure 25 Results obtained from a cross-sectional semiconductor device specimen of nominal thickness 400 nm prepared using conventional 'trench' FIB milling. (a) Bright-field TEM image of a PMOS (0.5μm gate) transistor, which forms part of a linear array of similar transistors, indicating the locations of the regions analyzed in more detail in the subsequent figures. The bright bands of contrast above the transistors are W contacts. Thickness corrugations are visible in the Si substrate in each image. The gates are formed from W silicide, while the amorphous layers above the gates and between the W plugs are formed from Si oxides that have different densities. (b) Eight-times-amplified phase contours, calculated by combining phase images from several holograms obtained across the region marked '1' in (a) using a microscope accelerating voltage of 200 kV and a biprism voltage of 160 V. Specimen charging results in the presence of electrostatic fringing fields in the

vacuum region outside the specimen edge, as well as elliptical phase contours within the Si oxide layers between the W contacts. (c) shows an equivalent phase image obtained after coating the specimen on one side with approximately 20 nm of carbon to remove the effects of charging. The phase contours now follow the expected mean inner potential contribution to the phase shift in the oxide layers, and there is no electrostatic fringing field outside the specimen edge. (d) One-dimensional line profiles obtained from the phase images in (b) and (c) along the line marked '2' in (a). The dashed and solid lines were obtained before and after coating the specimen with carbon, respectively. The dotted line shows the difference between the solid and dashed lines. Reprinted from Dunin-Borkowski et al. [80].

Figure 26 High-resolution (a) amplitude and (b) phase images of the aberration-corrected specimen wave reconstructed from an electron hologram of [110] Si, obtained at 300 kV on a CM30 FEGTEM. The spacing of the hologram fringes was 0.05 nm. The sideband contained {111}, {220}, {113} and {004} reflections, corresponding to lateral information of 0.136 nm. The characteristic Si dumbbell structure is visible only after aberration correction. Reprinted from Orchowski et al. [281].

Figure 27 (a) Schematic ray diagram for the differential mode of off-axis TEM electron holography. The symbols are defined in the text. (b) Composite differential mode electron hologram formed from a series of eight holograms of a 30nm-thick Co film. (c) Differential phase contrast image obtained from the hologram shown in (b). The arrow below the image indicates the direction of the magnetic signal analyzed. The arrow close to the bottom of the image indicates the position of a magnetic vortex. Reprinted from McCartney et al. [298].

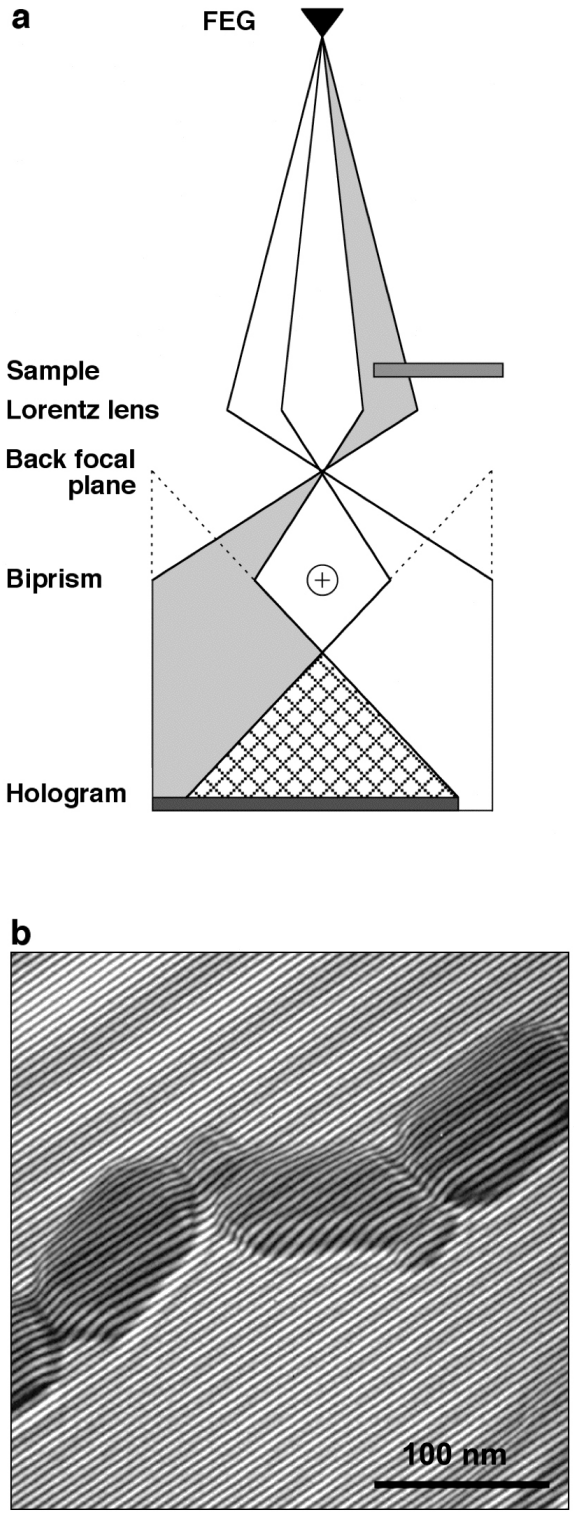
a
FEG
Sample
Lorentz lens
Back focal plane
Biprism
Hologram
b
100 nm

Figure 1

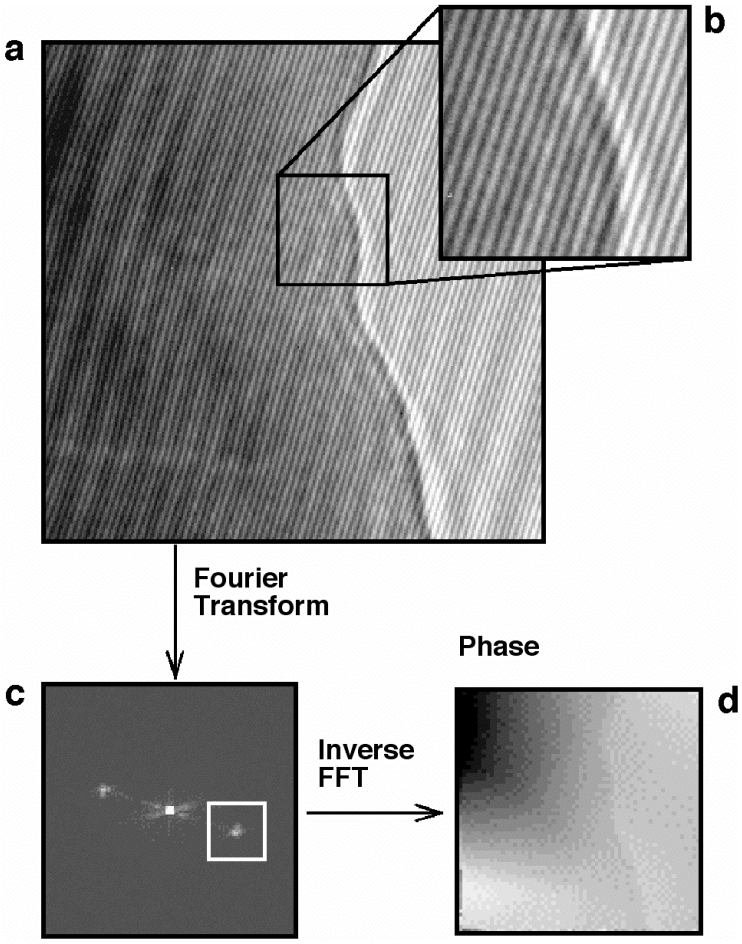

Figure 2

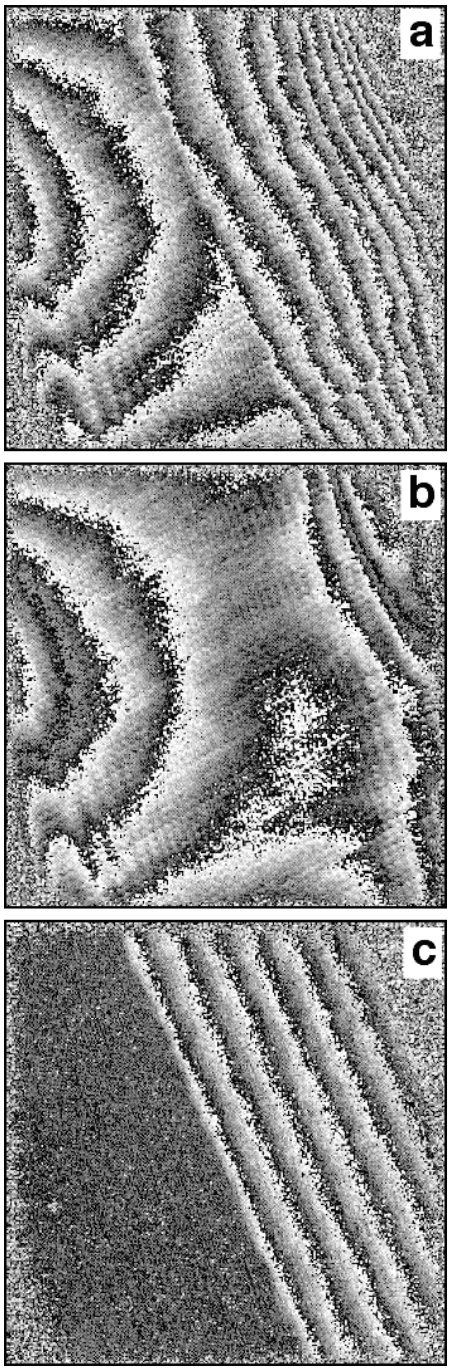

Figure 3

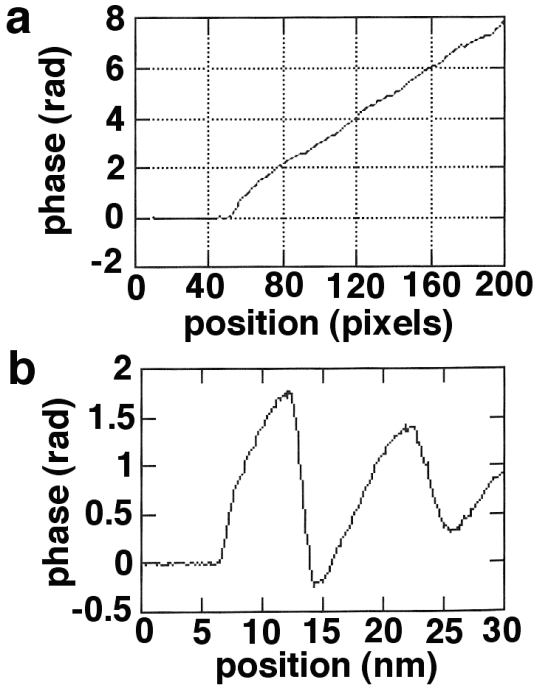
a
phase (rad)
8
6
4
2
0
-2
0
40
80
120
160
200
position (pixels)
b
phase (rad)
2
1.5
1
0.5
0
-0.5
0
5
10
15
20
25
30
position (nm)

Figure 4

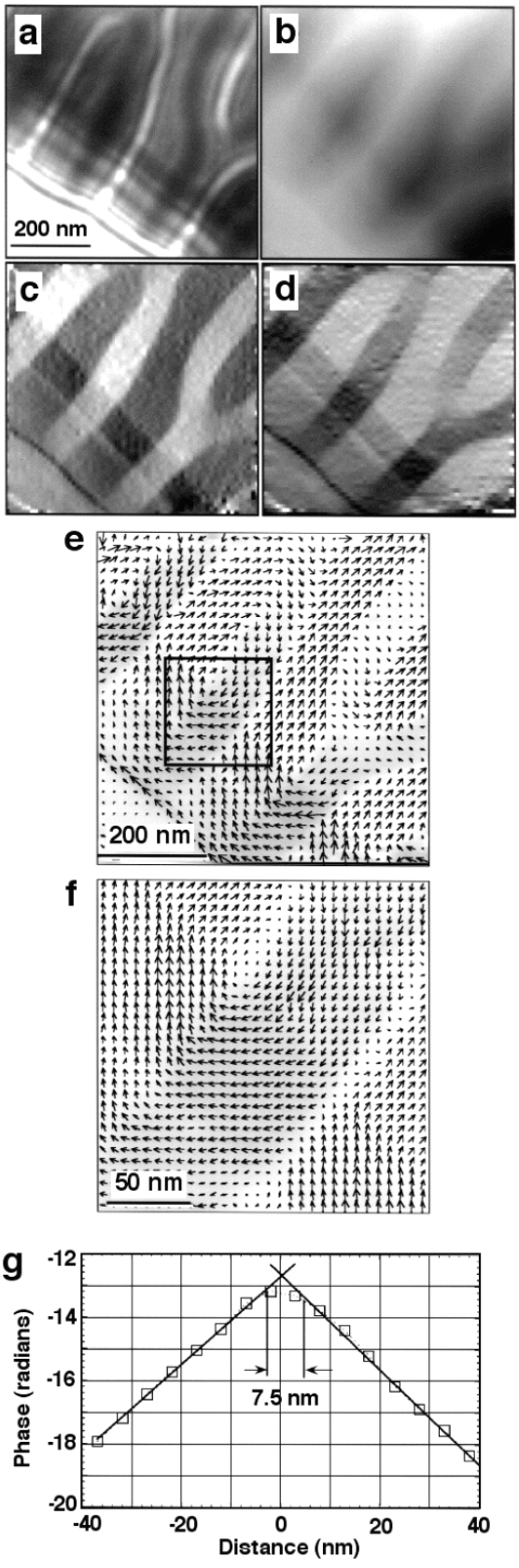
a
b
200 nm
c
d
e
200 nm
f
50 nm
g
-12
-14
-16
-18
-20
Phase (radians)
7.5 nm
-40
-20
0
20
40
Distance (nm)

Figure 5

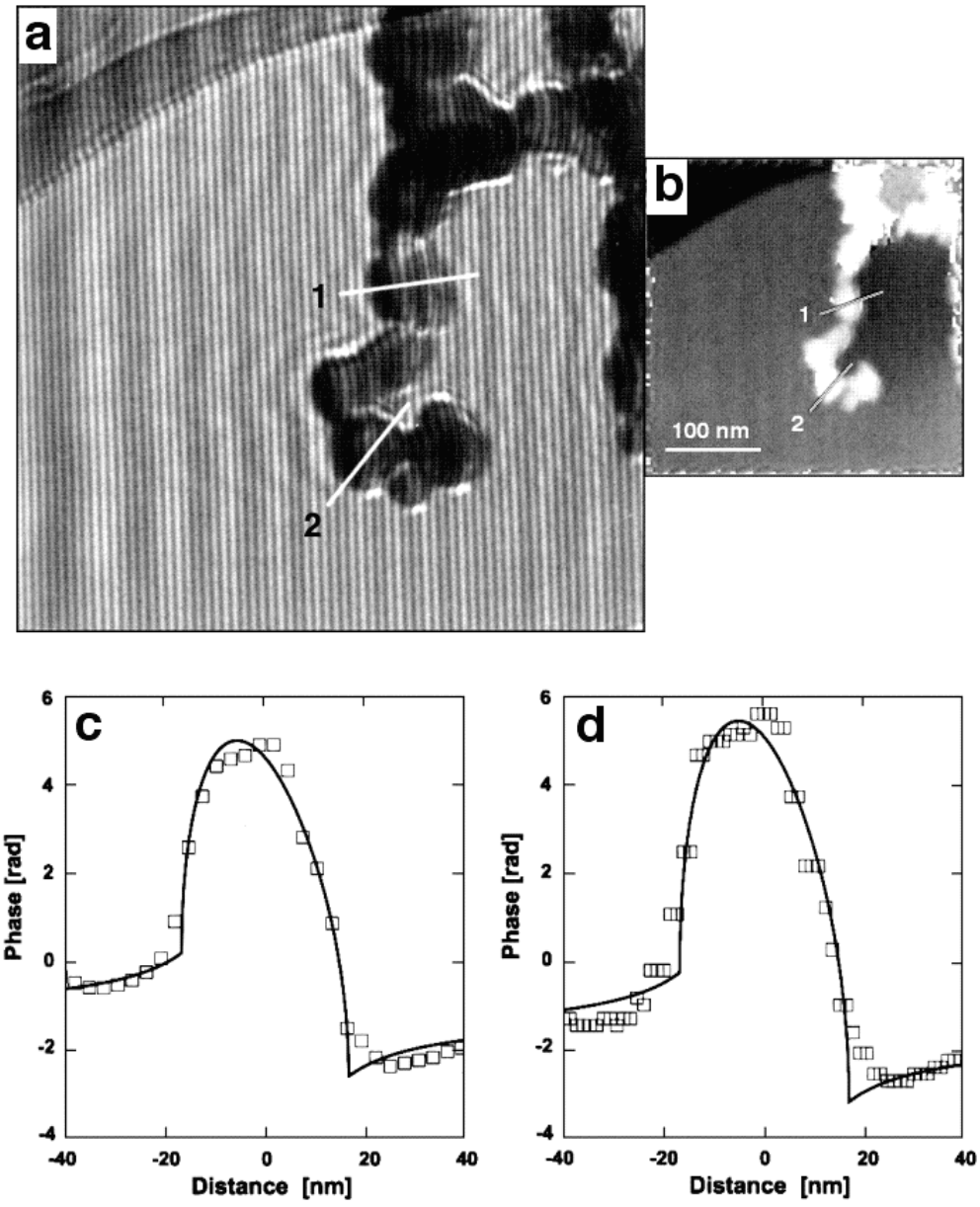

Figure 6

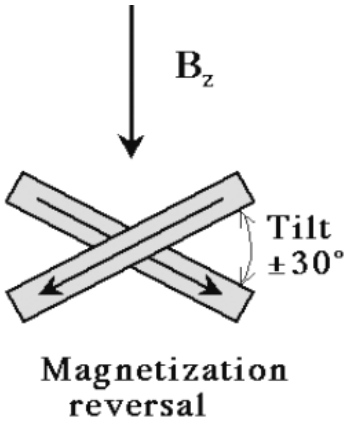

Figure 7

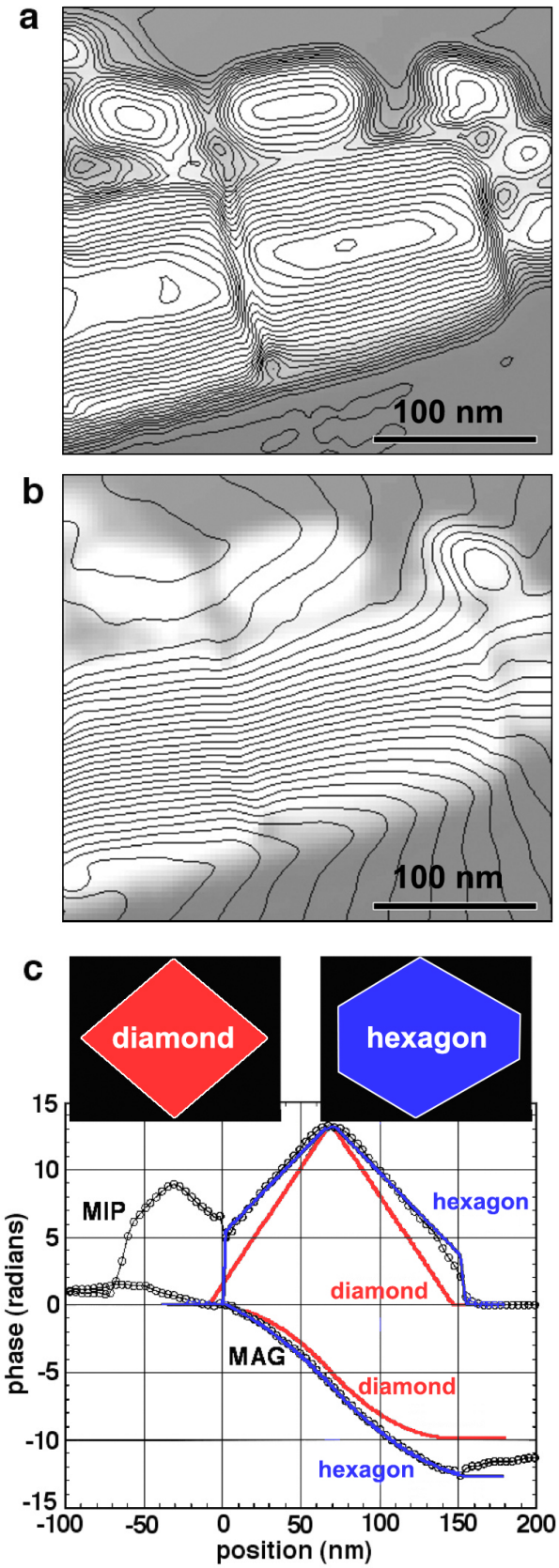
a
100 nm
b
100 nm
c
diamond
hexagon
MIP
MAG
hexagon
diamond
diamond
hexagon
phase (radians)
position (nm)
15
10
5
0
-5
-10
-15
-100
-50
0
50
100
150
200

Figure 8

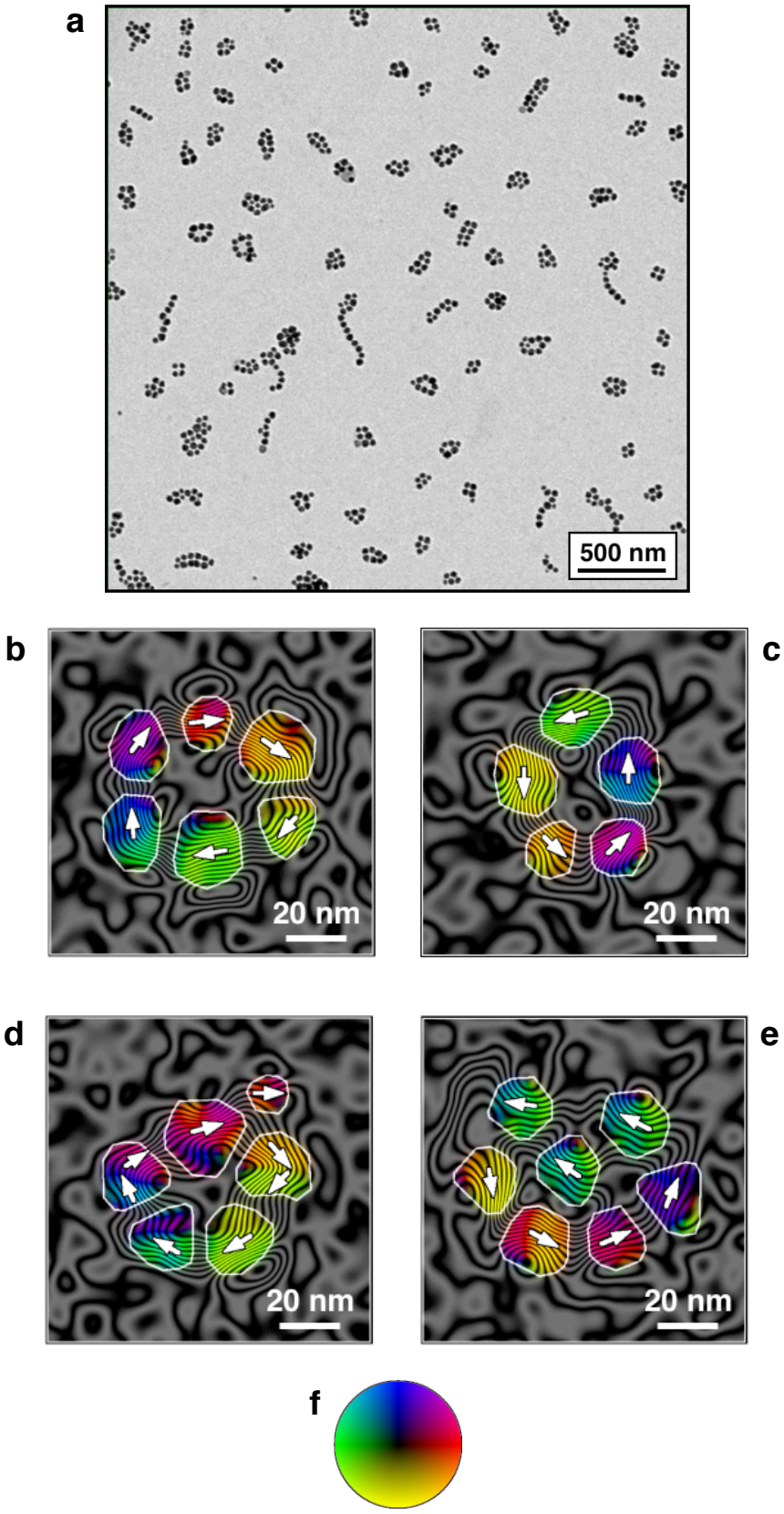

Figure 9 (color)

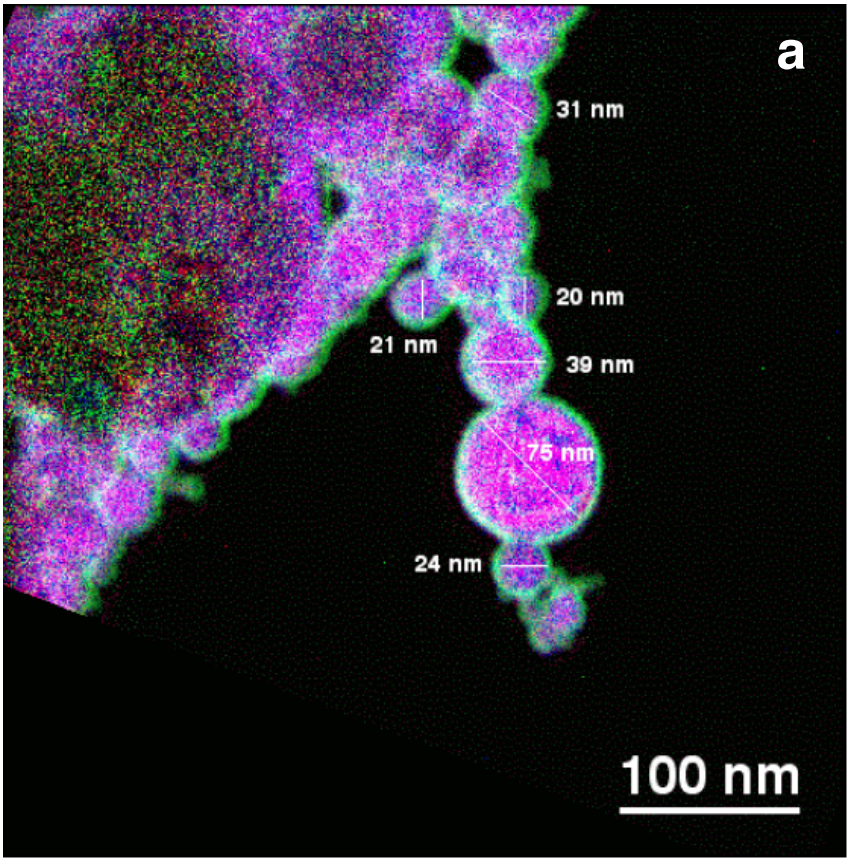

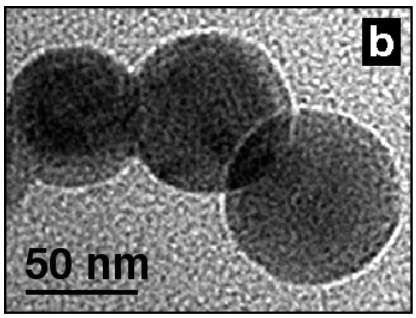

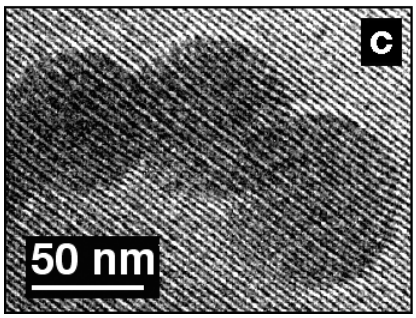

Figure 10 (color)

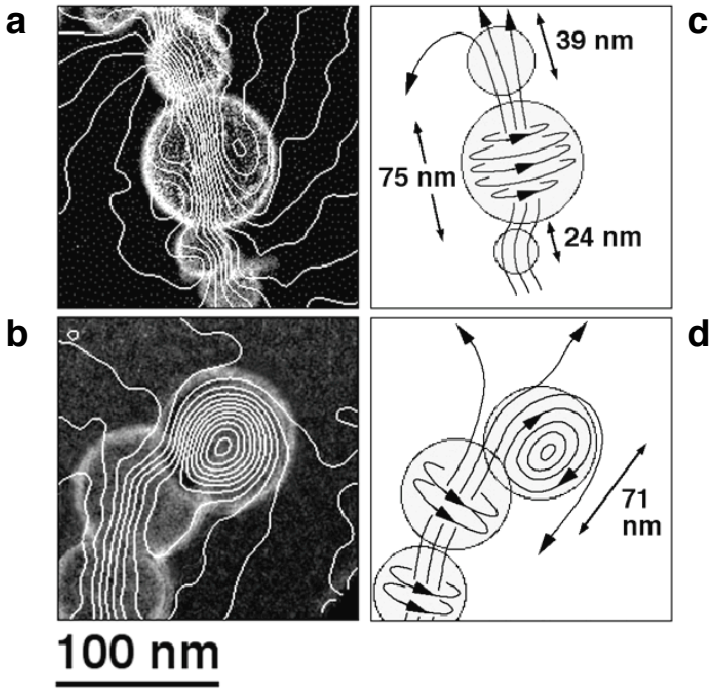

Figure 11

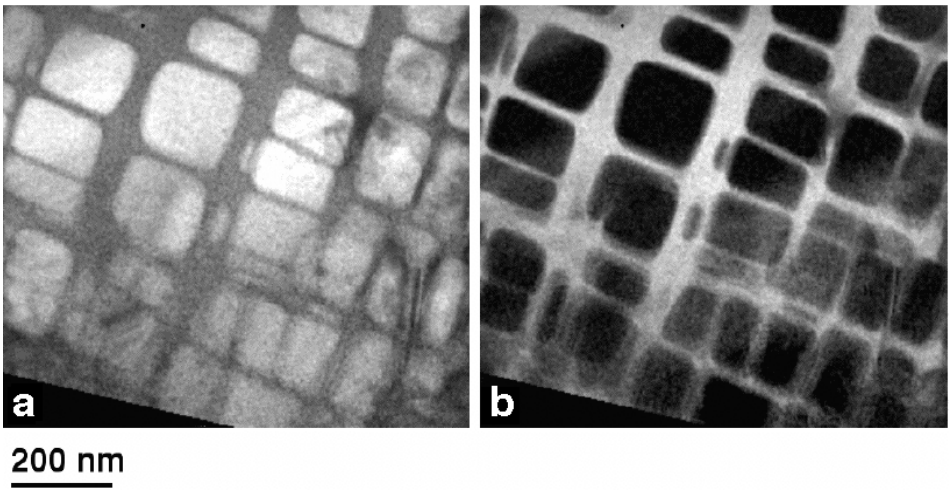

Figure 12

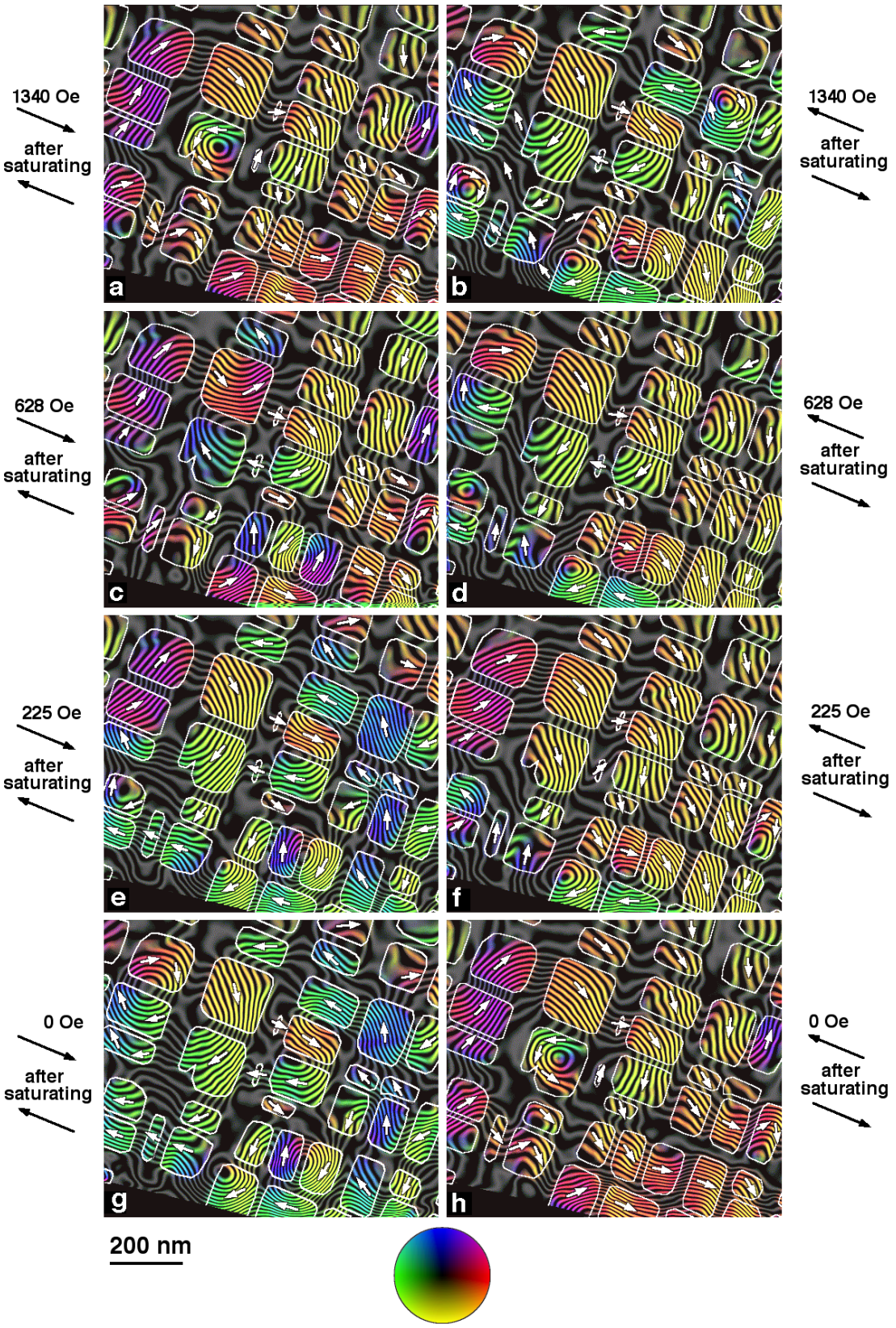

Figure 13 (color)

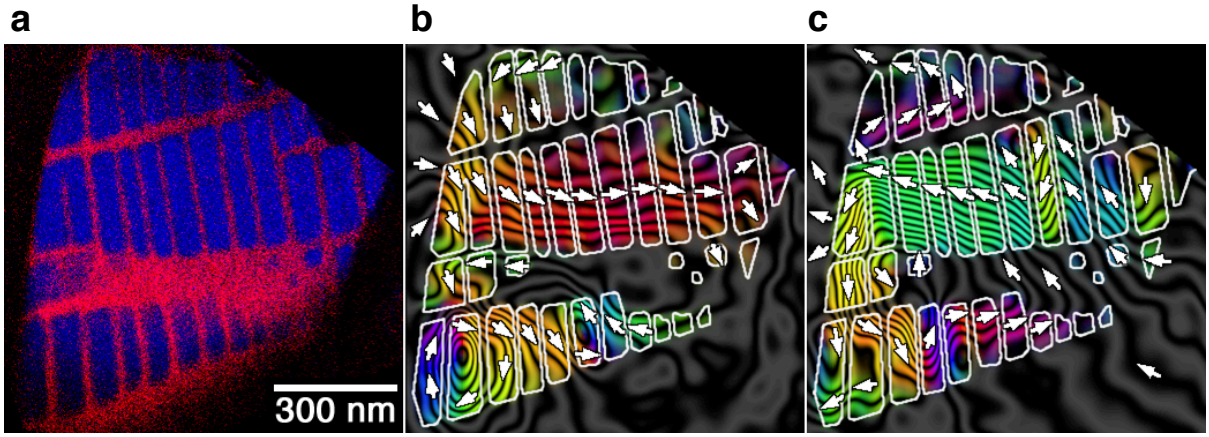

Figure 14

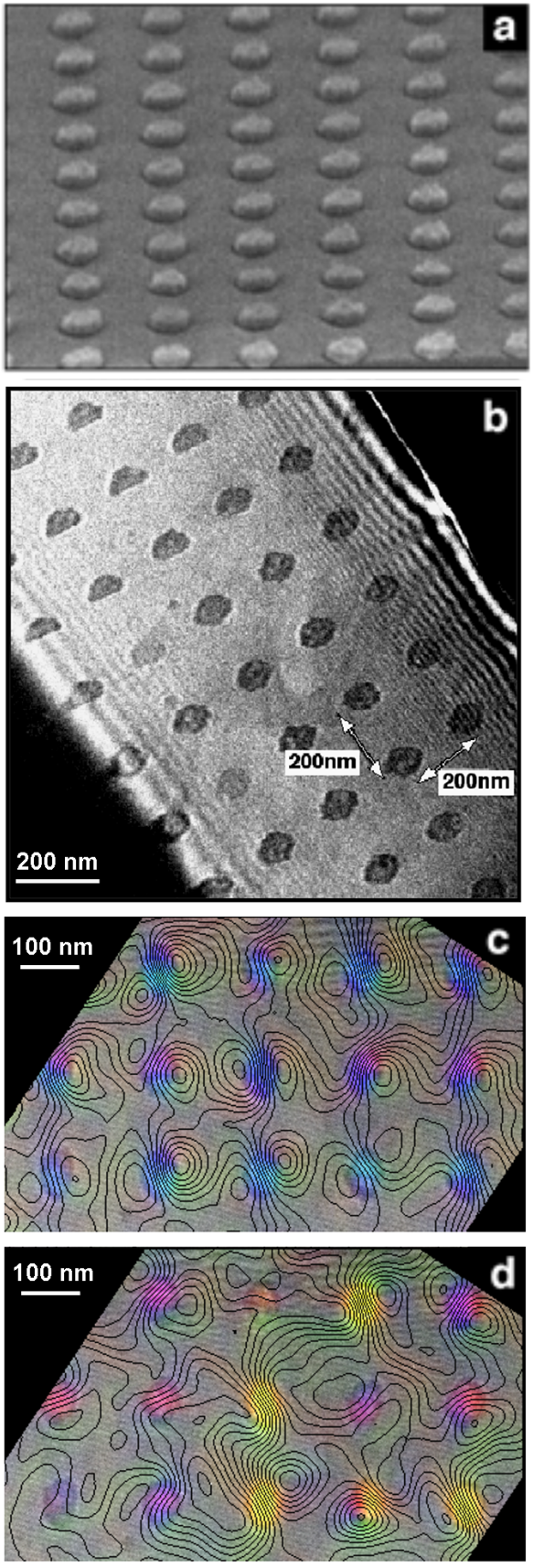

Figure 15

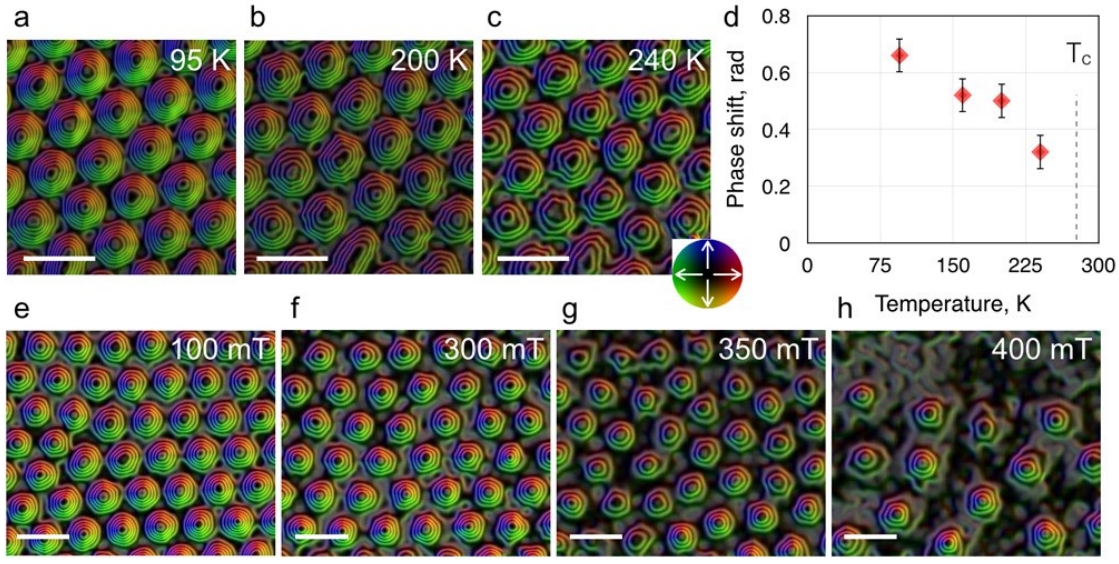
a
b
c
d
95 K
200 K
240 K
Phase shift, rad
0.8
0.6
0.4
0.2
0
0
75
150
225
300
Tc
Temperature, K
e
f
g
h
100 mT
300 mT
350 mT
400 mT

Figure 16

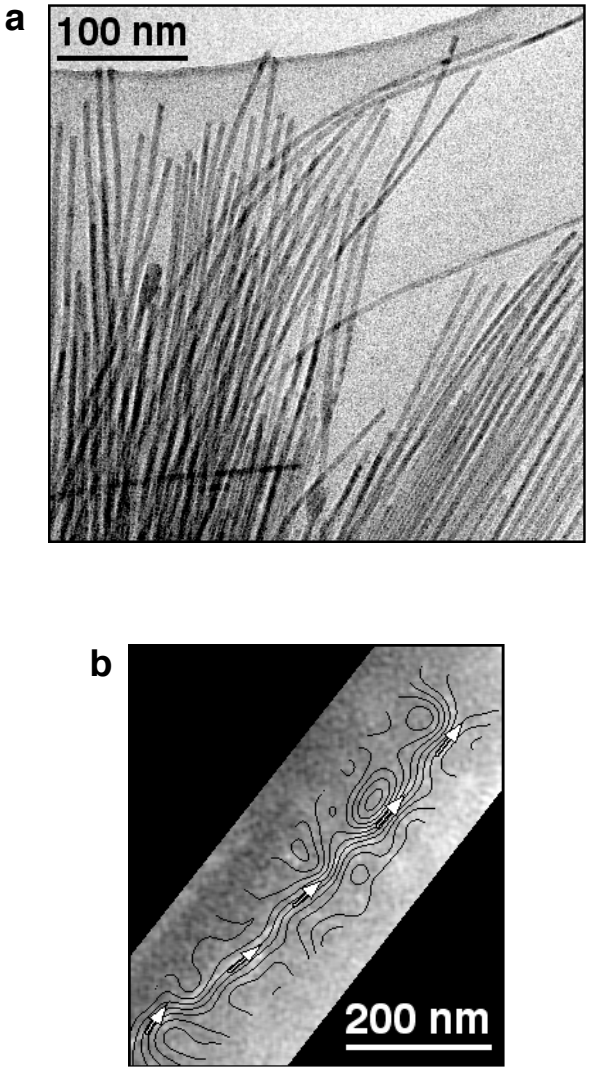

Figure 17

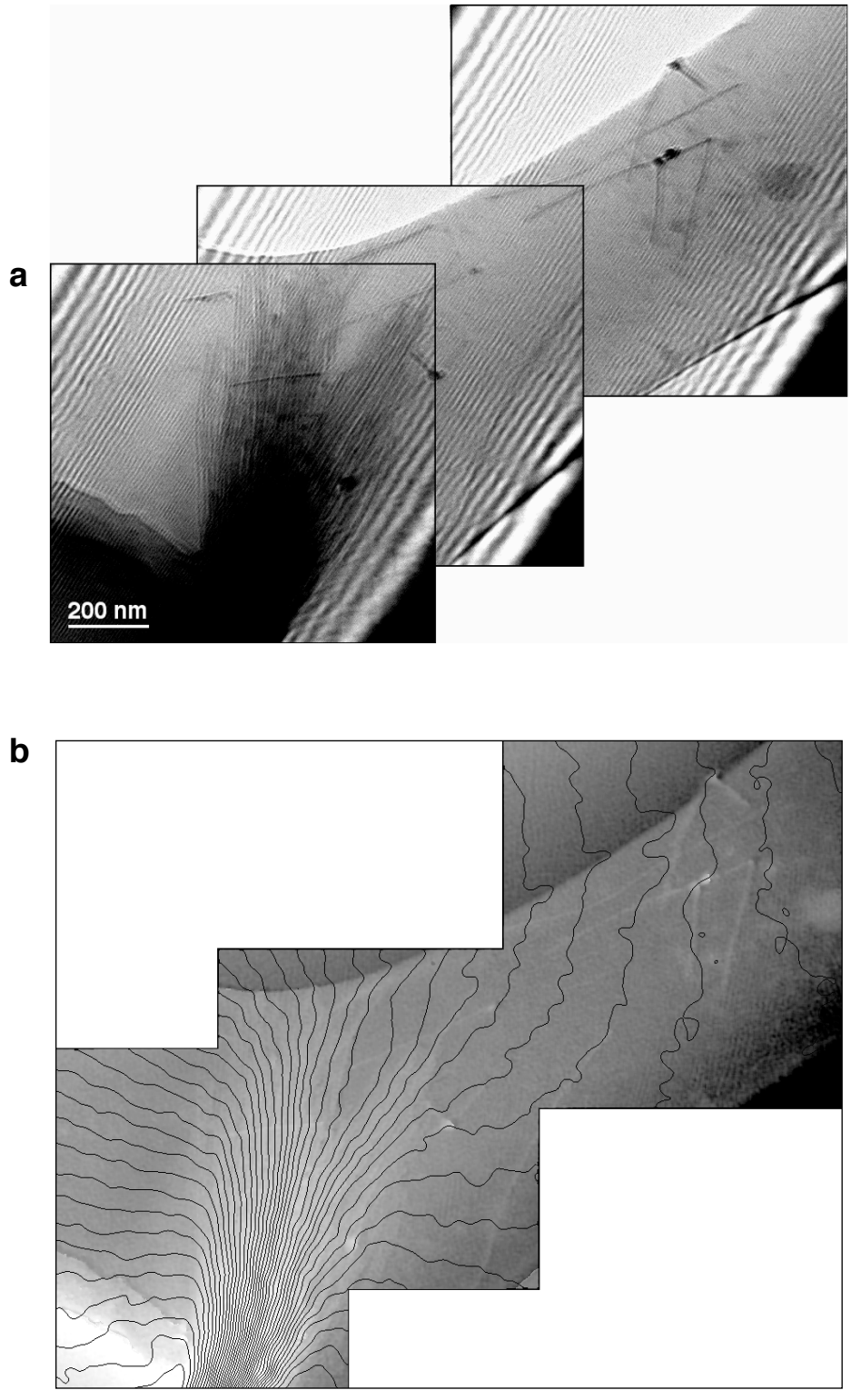

Figure 18

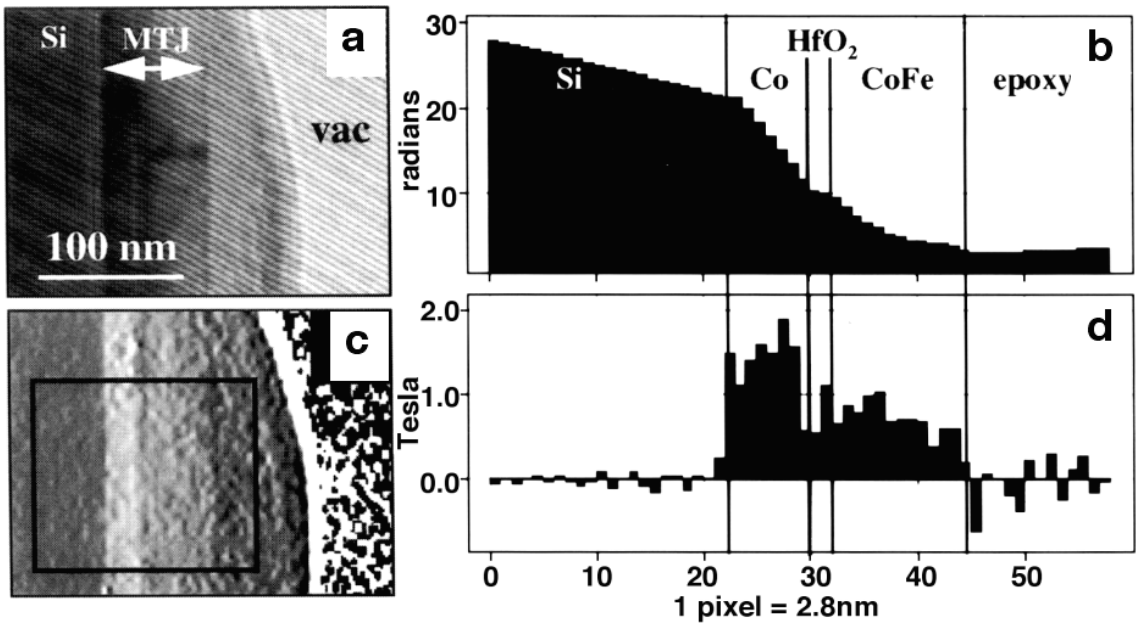
Si
MTJ
a
vac
100 nm
c
30
20
10
radians
Si
HfO2
Co
CoFe
epoxy
b
2.0
1.0
0.0
Tesla
d
0
10
20
30
40
50
1 pixel = 2.8nm

Figure 19

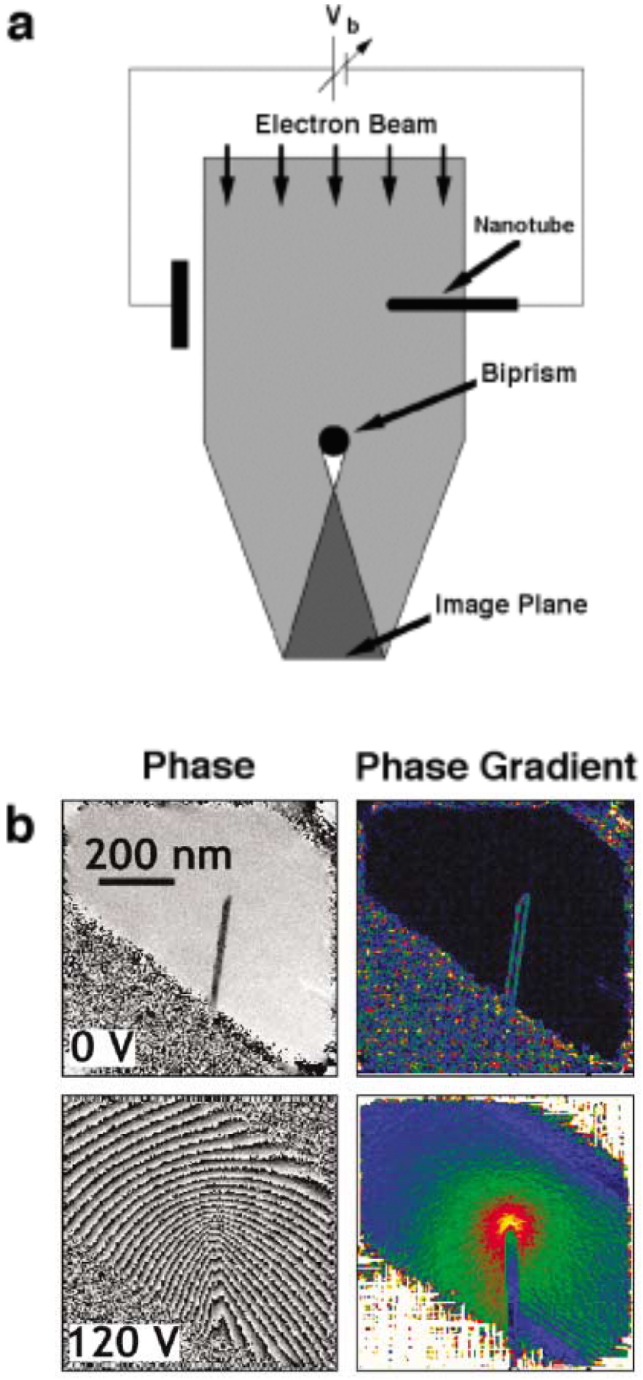
a
V b
Electron Beam
Nanotube
Biprism
Image Plane
Phase
Phase Gradient
b
200 nm
0 V
120 V

Figure 20

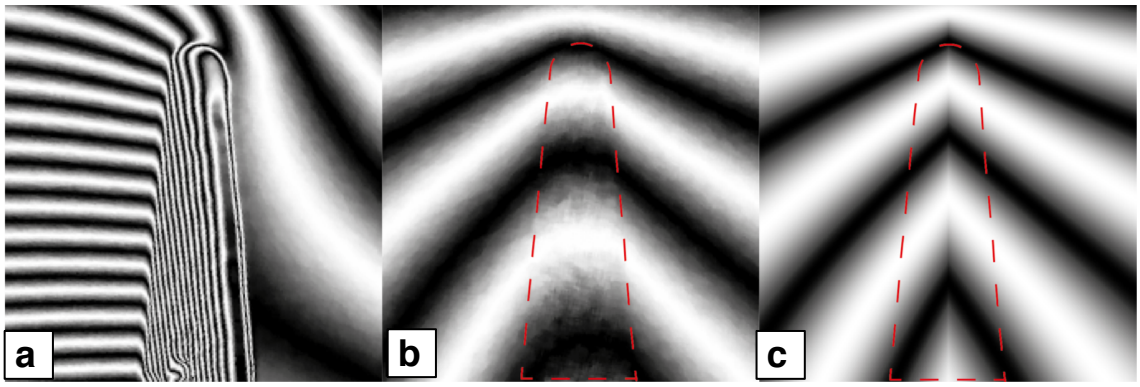

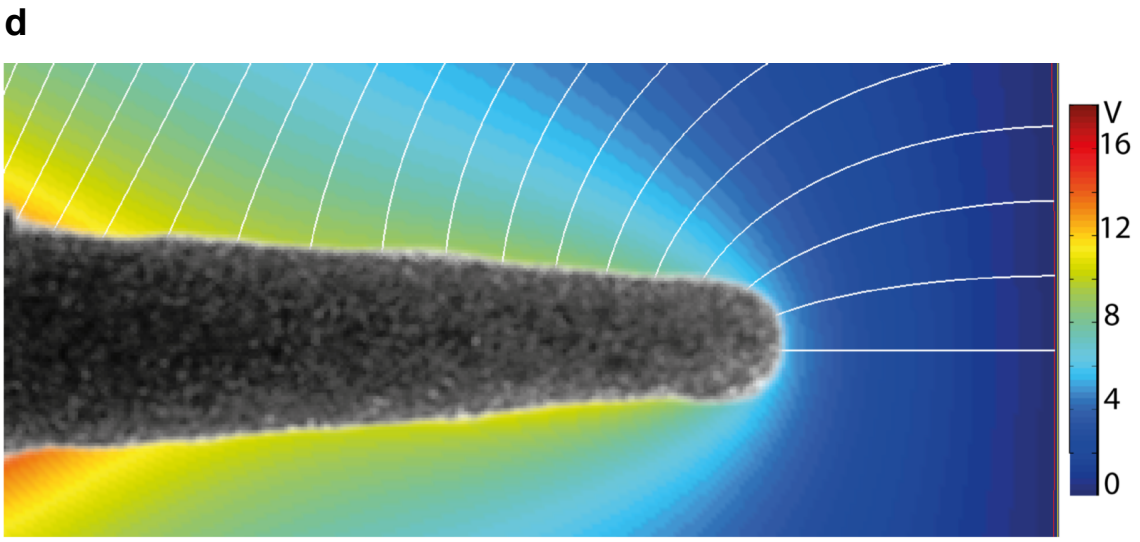

Figure 21

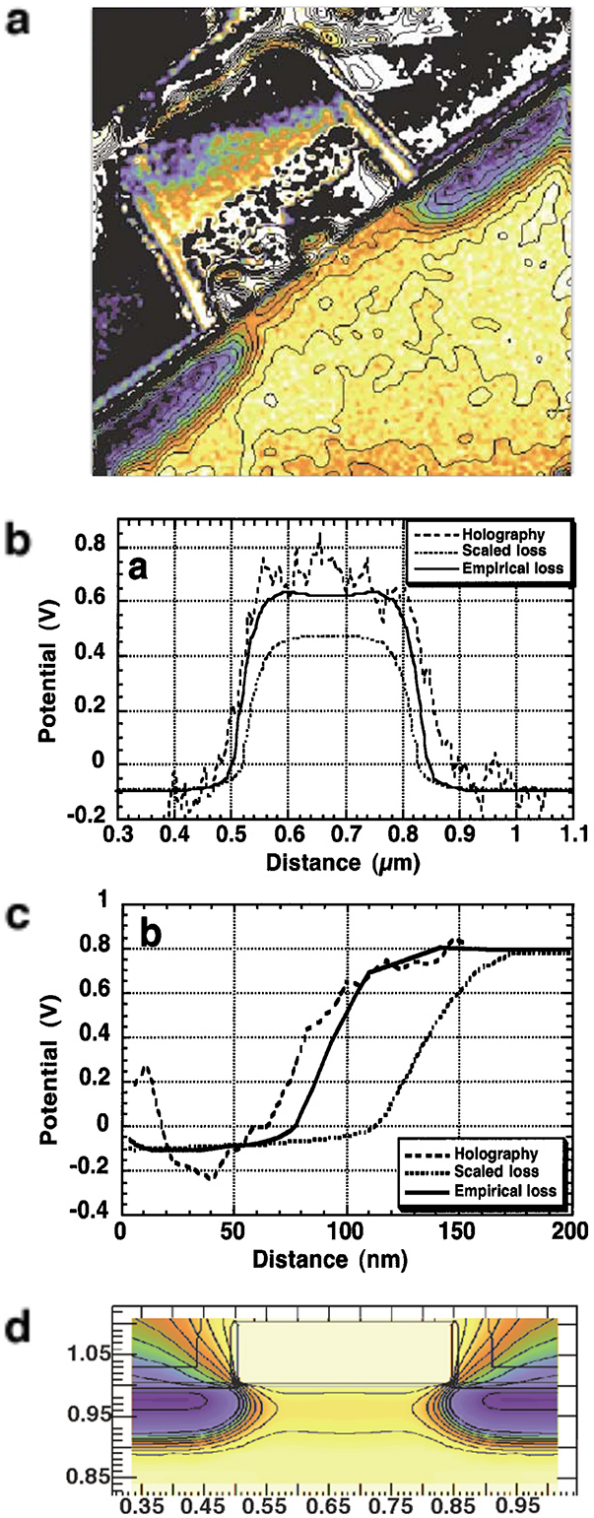
a
b
a
Holography
Scaled loss
Empirical loss
Potential (V)
Distance (μm)
c
b
Holography
Scaled loss
Empirical loss
Potential (V)
Distance (nm)
d

Figure 22

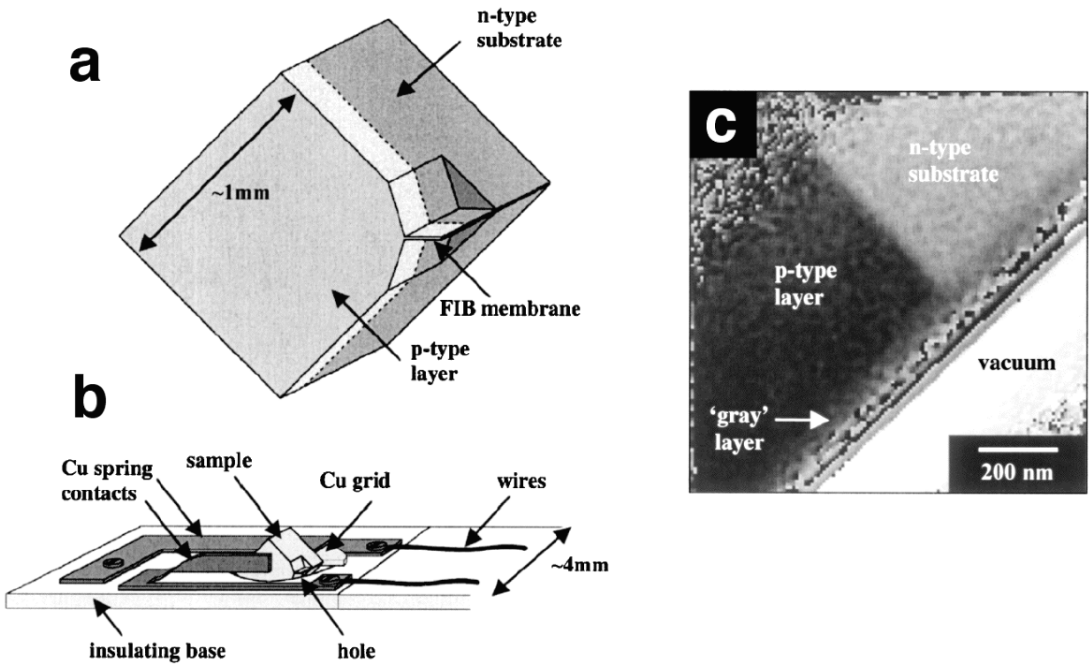
a
n-type substrate
~1mm
FIB membrane
p-type layer
b
Cu spring contacts
sample
Cu grid
wires
~4mm
insulating base
hole
c
n-type substrate
p-type layer
vacuum
'gray' layer
200 nm
d
biased sample
t_{cryst} = 390 nm
3 V
2 V
1 V
0 V
Phase ϕ (radians)
Position (nm)
e
biased sample
t_{cryst} = 390 nm
Step in phase Δϕ (radians)
Applied reverse bias (V)
f
p
n
0.5μm
Increasing sample thickness
Thin edge of cleaved sample

Figure 23

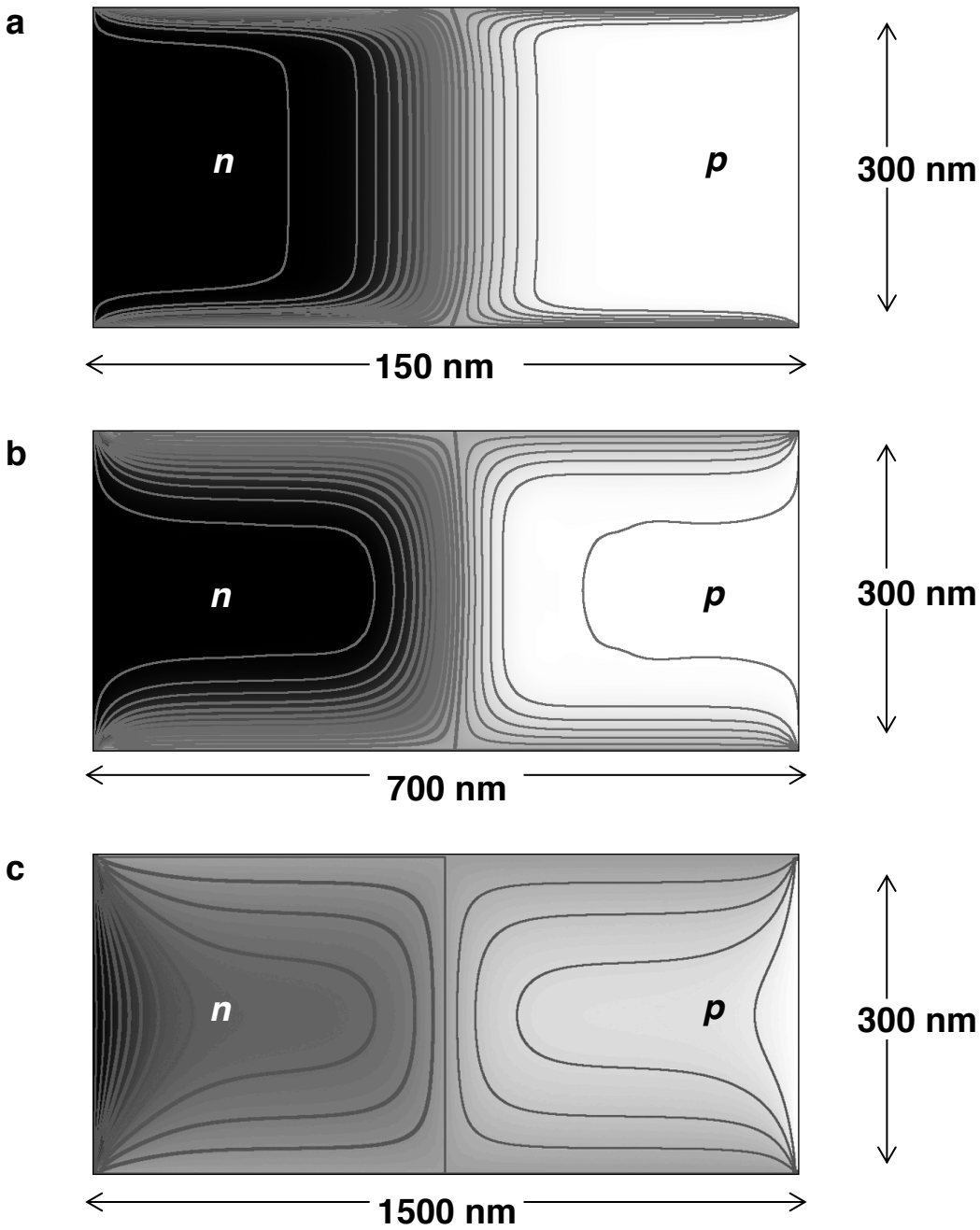

Figure 24

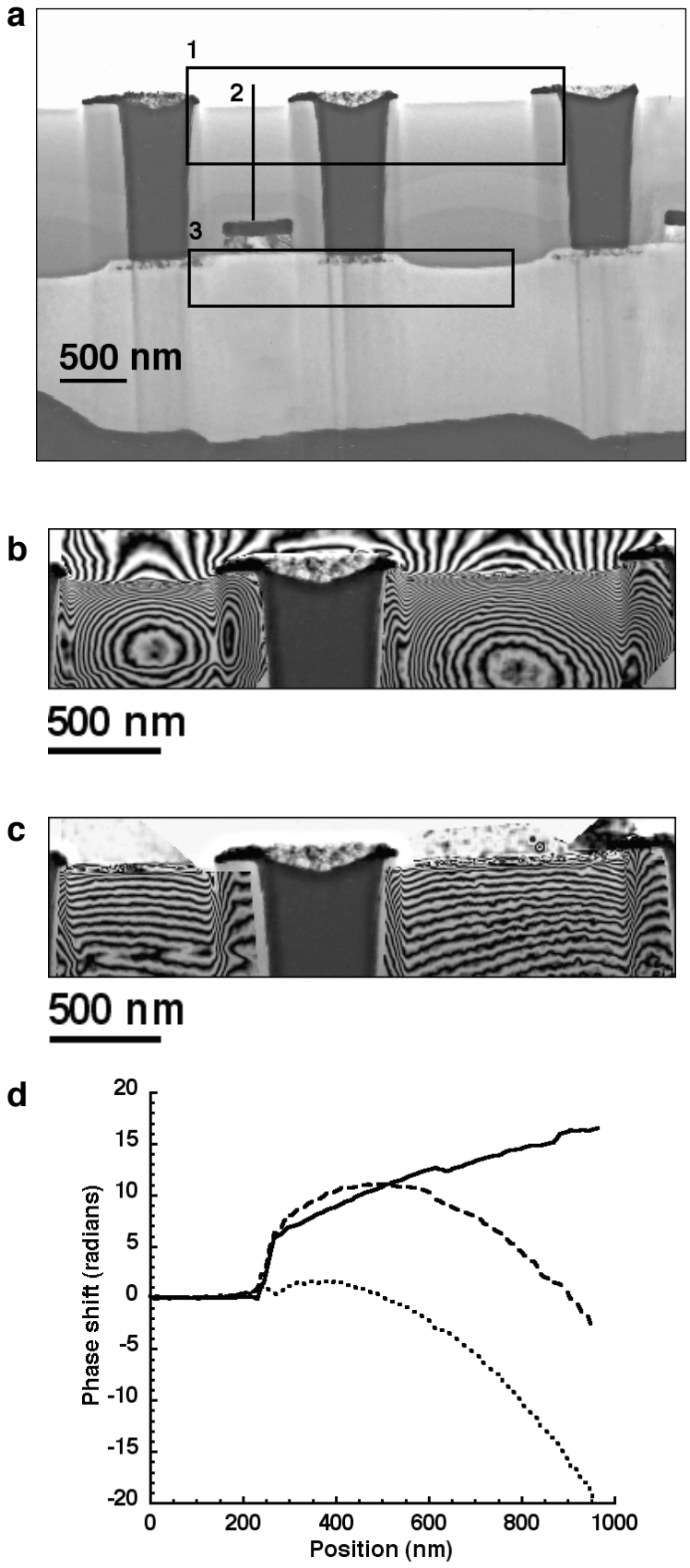
a
1
2
3
500 nm
b
500 nm
c
500 nm
d
Phase shift (radians)
20
15
10
5
0
-5
-10
-15
-20
0
200
400
600
800
1000
Position (nm)

Figure 25

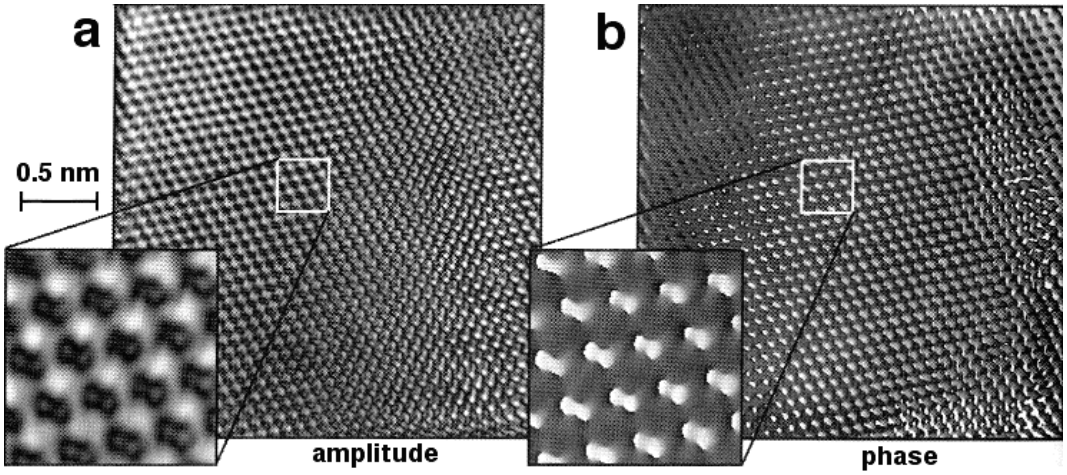

Figure 26

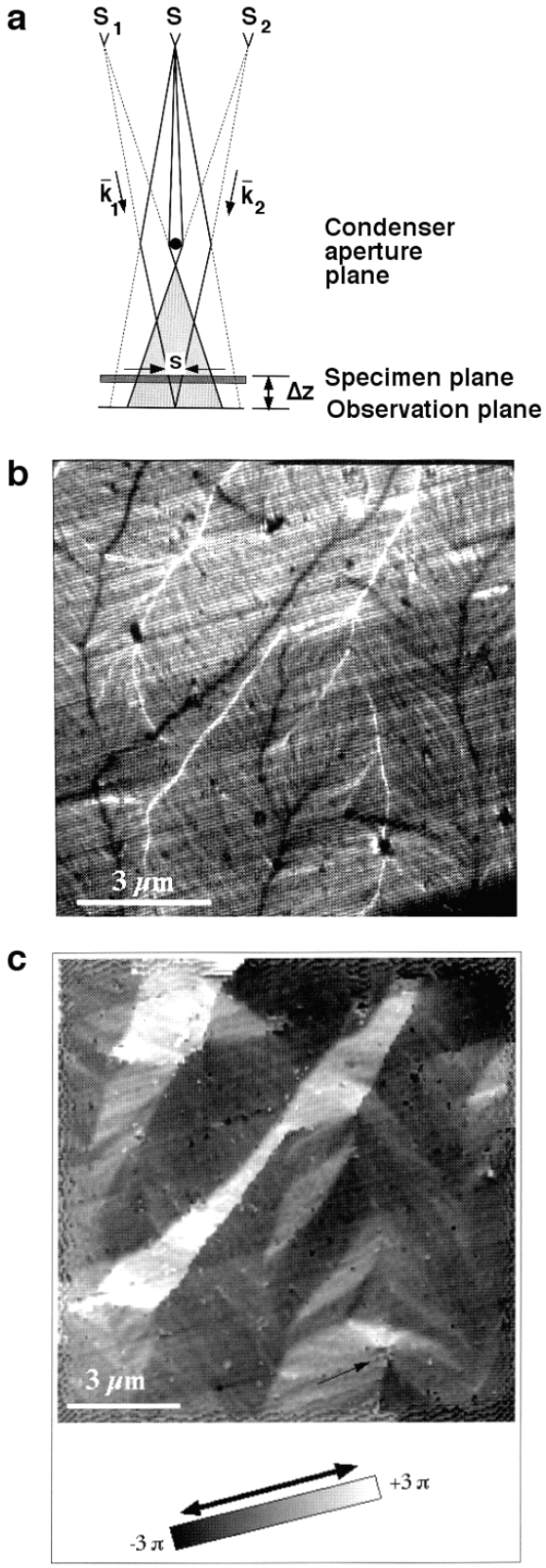
a
S1
S
S2
k1
k2
Condenser aperture plane
s
Δz
Specimen plane
Observation plane
b
3 μm
c
3 μm
+3 π
-3 π

Figure 27